Designing N-type Zintl phases for Thermoelectric Power Generation Applications

by

Verda Berşan Genceli

A Dissertation Submitted to the
Graduate School of Sciences and Engineering

in Partial Fulfillment of the Requirements for

the Degree of

Master of Science

in

Materials Science and Engineering

KOÇ ÜNİVERSİTESİ

June, 2024

Designing N-type Zintl phases for Thermoelectric Power Generation Applications

Koç University
Graduate School of Sciences and Engineering
This is to certify that I have examined this copy of a master's thesis by

Verda Berşan Genceli

and have found that it is complete and satisfactory in all respects,
and that any and all revisions required by the final
examining committee have been made.

Committee Members:

Assoc. Prof. Umut Aydemir (Advisor)

Assoc. Prof. Safacan Kölemen

Asst. Prof. Enes Kılınç

Date: June 12, 2024

Dedicated to my esteemed family, lineage bearing the patronymic Genceli…

ABSTRACT

Designing N-type Zintl phases for Thermoelectric Power Generation Applications

Verda Berşan Genceli

Master of Science in Materials Science and Engineering

June 12, 2024

The advancement of technology and a growing global population have increased energy demand, with over 60% of generated energy lost as waste heat, highlighting inefficiencies. Recovering waste heat is crucial for sustainable energy solutions. Thermoelectric materials, which convert heat into electricity, are of significant interest due to their silent operation, lack of moving parts, and scalable solid-state design. Thermoelectric generators use temperature gradients for power generation, and their efficiency is measured by the dimensionless figure of merit, zT ($zT = \alpha^2\sigma T/(\kappa_{lat} + \kappa_e)$), where α is the Seebeck coefficient, σ is electrical conductivity, κ_{lat} is lattice thermal conductivity, κ_e is electronic thermal conductivity, and T is temperature. Achieving optimal zT is challenging due to the interdependence of these properties. Certain ternary and binary metal phosphides, like GaP, NaSnP, and SrLiP, show promising potential as thermoelectric materials due to their superior electronic properties and low thermal conductivities, outperforming PbTe and Bi_2Te_3. Zintl phase thermoelectric materials, known for their tunable electronic transport properties, complex crystal structures, and low thermal conductivities, also exhibit high thermoelectric efficiencies. Notably, Mg_3Sb_2-based Zintl phases are particularly interesting for their excellent zT values as n-type materials, highlighting their potential in advancing thermoelectric technology. In this thesis, the synthesis and characterization of binary and ternary phosphides have been explored. These phosphides were synthesized through solid-state synthesis or high-energy ball milling (also known as mechanochemical synthesis), followed by spark plasma sintering to achieve densification for measurement of physical properties. Efforts were made to identify the most efficient synthesis routes for ternary phosphides. Despite rigorous efforts, our exploration encountered significant obstacles owing to the high air sensitivity of the ternary phases and substantial resistivity characteristic of the binary phases. These properties rendered the measurement of both electrical and thermal conductivities unfeasible.

Subsequent investigations focused on the design and determination of electrical and thermal transport properties of innovative and efficient n-type Mg_3Sb_2-based Zintl phases, such as $CaMg_2Sb_2$ and $CaMg_2Bi_2$. This was achieved through band structure engineering, employing doping strategies with tellurium and lanthanum ($Ca_{0.8}La_{0.2}Mg_{2.1}Sb_2$, $Ca_{0.9}La_{0.1}Mg_{2.1}Sb_{1.95}Te_{0.05}$, $Ca_{0.8}La_{0.2}Mg_{2.1}Bi_2$ and $Ca_{0.9}La_{0.1}Mg_{2.1}Bi_{1.95}Te_{0.05}$). These samples were successfully synthesized using high-energy ball milling and sintered through the spark plasma sintering technique. With the help of microstructural characterization and WDX analysis determination of effective doping has been made. Transport measurements were conducted to determine the thermoelectric performance of doped and undoped samples between 300-700 K. After introducing La and Te doping, resistivity and thermal conductivity values had a decrease, Seebeck coefficient values shifted from positive to negative across the entire temperature range studied. Additionally, the observation of negative Hall mobility values indicated that the electrical conductivity in these materials is predominantly due to the movement of free electrons, suggesting that effective doping strategies have indeed increased the carrier concentrations. Also, the calculations made to determine the main contribution of thermal

conductivity values revealed that the main contribution is coming from the lattice thermal conductivity part.

In conclusion, the La and Te doped Mg_3Sb_2-based samples, specifically $CaMg_2Sb_2$ and $CaMg_2Bi_2$, demonstrate potential as efficient n-type thermoelectric materials. By increasing the electrical conductivity values and achieve a promising zT value these findings suggest their viability for incorporation into complete Zintl phase thermoelectric modules, offering promising pathways for enhancing thermoelectric technology's effectiveness and sustainability.

ÖZETÇE

N-Tip Zintl Fazlarının Termoelektrik Enerji Üretim Uygulamaları İçin Tasarımı

Verda Berşan Genceli

Malzeme Bilimi ve Mühendisliği, Yüksek Lisans

12 Haziran, 2024

Teknolojinin ilerlemesi ve artan dünya nüfusu, enerji talebini enerji talebinde önemli bir artışa yol açmıştır. Son çalışmalar, endişe verici bir eğilimi vurgulamaktadır: Küresel olarak üretilen enerjinin %60'tan fazlası atık ısı olarak kayboluyor. Bu eğilim, mevcut enerji kullanım uygulamalarımızdaki önemli verimsizlikleri ortaya koymaktadır. Bu bağlamda atık ısının geri kazanılması, sürdürülebilir enerji çözümleri için büyük önem taşımaktadır. Isıyı elektriğe dönüştürebilen termoelektrik malzemeler, sessiz çalışmaları, hareketli parça içermemeleri ve ölçeklenebilir katı hal tasarımları nedeniyle önemli bir ilgi odağıdır. Termoelektrik jeneratörler, güç üretimi için sıcaklık gradyanlarını kullanır ve verimlilikleri, zT ($zT = \alpha^2\sigma T/(\kappa_{lat} + \kappa_e)$) ile ölçülür. Burada α Seebeck katsayısı, σ elektriksel iletkenlik, κ_{lat} kafes termal iletkenliği, κ_e elektronik termal iletkenlik ve T sıcaklığı temsil eder. Bu özelliklerin birbirine bağımlı olması nedeniyle optimal zT değerine ulaşmak zordur. GaP, NaSnP ve SrLiP gibi bazı üçlü ve ikili metal fosfitler, üstün elektronik özellikleri ve düşük ısıl iletkenlikleri sayesinde termoelektrik malzemeler olarak umut vaat etmektedir ve PbTe ve Bi_2Te_3'ü geride bırakmaktadır. Zintl fazı termoelektrik malzemeler, ayarlanabilir elektronik taşıma özellikleri, karmaşık kristal yapıları ve düşük ısıl iletkenlikleri ile yüksek termoelektrik verimlilik sergiler. Özellikle, n-tipi malzemeler olarak mükemmel zT değerleri ile dikkat çeken Mg_3Sb_2-bazlı Zintl fazları, termoelektrik teknolojisini ilerletme potansiyeline sahiptir. Bu tezde, ikili ve üçlü fosfitlerin sentezi ve karakterizasyonu incelenmiştir. Bu fosfitlerin katı hal sentezi veya yüksek enerjili bilyalı öğütme (mekanokimyasal sentez olarak da bilinir) yoluyla sentezlenmiş ve ardından fiziksel özelliklerin ölçülmesi için yoğunlaştırma sağlamak amacıyla kıvılcım plazma sinterleme ile sinterlenmiştir. Üçlü fosfitler için en verimli sentez yollarını belirlemek amacıyla çaba sarf edilmiştir. Ancak, üçlü fazların yüksek hava duyarlılığı ve ikili fazların yüksek direnç karakteristiği nedeniyle ciddi engellerle karşılaşılmış ve bu özellikler, hem elektriksel hem de ısıl iletkenliklerin ölçülmesini olanaksız hale getirmiştir.

Sonraki araştırmalar, tellür ve lantanum ile katkılama stratejileri kullanılarak $Ca_{0.8}La_{0.2}Mg_{2.1}Sb_2$, $Ca_{0.9}La_{0.1}Mg_{2.1}Sb_{1.95}Te_{0.05}$, $Ca_{0.8}La_{0.2}Mg_{2.1}Bi_2$ and $Ca_{0.9}La_{0.1}Mg_{2.1}Bi_{1.95}Te_{0.05}$ gibi yenilikçi ve verimli n-tipi Mg3Sb2 bazlı Zintl fazlarının tasarımı ve elektriksel ve ısıl taşıma özelliklerinin belirlenmesine odaklanmıştır. Bu numuneler, yüksek enerjili bilyalı öğütme kullanılarak başarıyla sentezlenmiş ve kıvılcım plazma sinterleme tekniği ile sinterlenmiştir. Mikroyapısal karakterizasyon ve WDX analizleri yardımıyla etkili katkılamanın belirlenmesi sağlanmıştır. 300-700 K arasında katkılı ve katkısız numunelerin termoelektrik performansını belirlemek için taşıma ölçümleri yapılmıştır. Yapıya La ve Te katkısı eklendikten sonra, direnç ve ısıl iletkenlik değerlerinde bir düşüş gözlenmiş ve Seebeck katsayısı değerleri pozitiften negatife kaymıştır. Ayrıca, negatif Hall mobilite değerlerinin gözlemlenmesi, bu malzemelerdeki elektriksel iletkenliğin ağırlıklı olarak serbest elektronların hareketinden kaynaklandığını ve etkili katkılama stratejilerinin taşıyıcı konsantrasyonlarını gerçekten artırdığını önermektedir. Ayrıca, ısıl iletkenlik değerlerinin ana katkısını belirlemek için yapılan hesaplamalar, ana katkının kafes ısıl iletkenliğinden geldiğini ortaya koymaktadır.

Sonuç olarak, La ve Te ile katkılanmış Mg_3Sb_2-bazlı numuneler, özellikle $CaMg_3Sb_2$ ve $CaMg_2Bi_2$, verimli n-tipi termoelektrik malzemeler olarak potansiyel göstermektedir. Elektriksel iletkenlik değerlerini artırarak ve umut verici bir zT değeri elde ederek, bu bulgular, termoelektrik teknolojisinin etkinliğini ve sürdürülebilirliğini artırmak için umut verici yollar sunan tam Zintl fazı termoelektrik modüllerine dahil edilmeleri için uygun olduklarını önermektedir.

ACKNOWLEDGEMENTS

Without the invaluable support of those I wish to acknowledge and the guidance they provided, the journey I embarked upon at Koç University would not have been as enriching and unforgettable.

This study was supported by The Scientific and Technological Research Council of Turkey (TUBITAK) under the Grant Number 221N045. I extend my sincere thanks to TUBITAK for their generous support.

Foremost, my gratitude goes to my advisor, Assoc. Prof. Dr. Umut Aydemir, an expert in the realm of boron-based advanced materials and thermoelectricity. I am deeply appreciative for the mentorship that guided me through the pivotal stages of my academic journey. His unwavering support in a field distinct from my undergraduate major, along with imparting the virtues of calmness and patience in academic pursuits and laboratory endeavors, has been instrumental.

I extend my thanks to Dr. Anna Maria Miko and Dr. Melis Çağdaş, where I served as an assistant in their laboratory. Their adeptness in educating future generations in an engaging manner, coupled with their support during my thesis and education, has been invaluable. Special appreciation is reserved for Dr. Barış Yağcı, responsible for the SEM and EDX analyses, and Eleonora Isotta, who conducted my Hall Effect Measurements at Northwestern University. Lastly, my heartfelt gratitude goes to Dr. Pınar Tatar, whose warm and caring demeanor brightened the corridors and made every interaction a delightful experience.

I would like to articulate my thanks to all the KUBAM laboratory group members, for being kind, friendly and well supportive since the day I get accepted. I'm very appreciative for thir help and support. Allow me to specifically mention, Melis Aktürk Aktaş, Melis Özen and Arda Baran Burçak, I would like to express my grates gratitude for helping me, leading me though my first steps in thermoelectricity experiments and also made me feel no need for hesitation in any question about every conceivable thing. The other very special ones are Ebrahim Sadeghi and Sanaz Chamani, they become more than a friend and became a brother and a sister to me. I know that always we will felt the same whenever and where ever we are. I would like to thank specially to Dr. Müjde Yahyaoğlu for teaching me and lead me throughout my journey. She never refuses nay of my questions or practices. She gives the most out of herself to lead me and become successful in my career.

My best friends, who become sisters to me in a very short period of time, Elif Hançer and Zeynep Deniz Lal. They always support me, whatever and where every I am, without any doubts. I believe that without them I will never felt like I was belong to this university, but they made my whole education comfortable, fun and memorable.

And of course, my biggest thanks goes to my family, Mehmet and Esra Genceli, who raised me, brought me this far, supported me no matter what and respected every decision of mine. I would like to thank you very much for being with me every time I was sad during this process, rejoicing with me every time I was happy, and making me feel that we hold each other tightly under all circumstances. Thank you for being a light and example for me in my academic career and success. As a Genceli family member, I will try to be my best for you and all the Engineers in the Genceli family.

Contents

LIST OF TABLES

LIST OF FIGURES

ABBREVIATIONS

EU	European Union
AHPDOS	Non-harmonic phonon dispersion and Phonon Desity of States
B	Thermoelectric Quality Factor
BSE	Back Scattered Electron
CBM	Conduction Band Minimum
DFT	Density Functional Theory
EDOS	Electronic Density of States
EDX	Energy Dispersive X-Ray Spectroscopy
ELF	Electron Localization Function
HPDOS	Harmonic Phonon Dispersion and Phonon Density of States
Hv	Hardness Value
LFA	Laser Flash Analysis
SEM	Scanning Electron Microscopy
SPS	Spark Plasma Sintering
TEM	Transmission Electron Microscopy
VBM	Valence Band Minimum
VEC	Valence Electron Count
WDX	Wavelength Dispersive X-ray
XRD	X-Ray Diffraction
Z	Atomic Number
zT	Thermoelectric Figure of Merit

Chapter 1:

INTRODUCTION

The growing global population brings with it an escalating demand for energy. The reliance on fossil fuels as the primary source of energy has led to significant environmental pollution, primarily due to the high amounts of CO2 produced. This contributes to global warming, climate change, and an increasing carbon footprint, among other issues. Consequently, there has been a shift towards exploring cleaner, more sustainable energy sources. Renewable energy, in this context, has risen to prominence, playing a pivotal role in reducing emissions and enhancing energy production to meet the burgeoning demand.

It has been reported that 72% of the energy input is lost through industrial processes, with 52% of this input energy being lost as waste heat (1). The majority of the total energy demand comes from industrial applications. For instance, in 2011, Europe used 62% of its total energy in industrial processes (2). To address this considerable demand, strategies for reducing excess energy consumption and supplementing the energy supply include the recovery of waste heat from production processes, presenting a viable solution. Figure 1. 1 illustrates the heat consumption data in the European Union (EU), varying across different industrial sectors, with values obtained from the 2015 Eurostat (3).

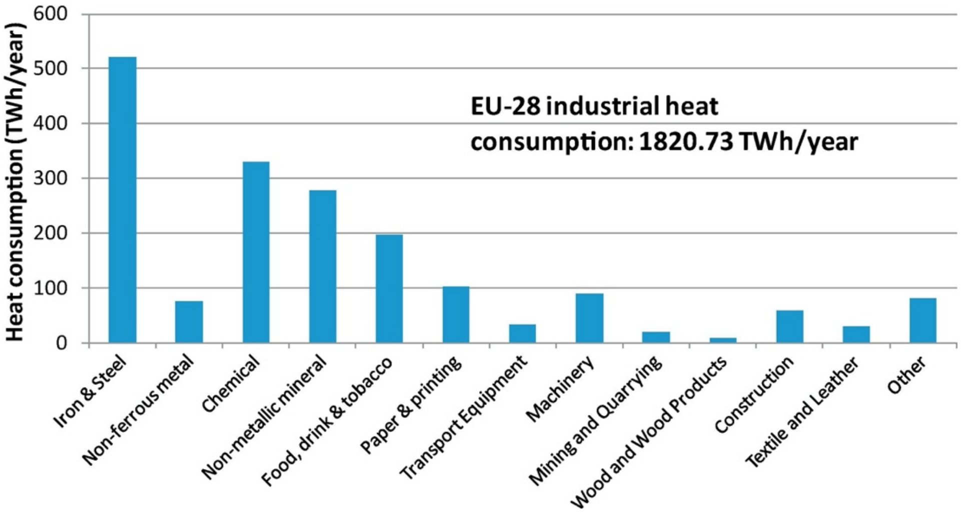

Figure 1. 1 Heat consumption values by the industrial applications in EU (3).

In addition to industrial sectors, a critical factor in assessing waste heat is the temperature level of the heat produced. It's essential to evaluate whether the heat generated during industrial processes is of sufficient quality or possesses the potential to be utilized as an energy source. Waste heat from industrial applications is classified into three categories based on temperature: high (> 400ºC), medium (100-400 ºC), and low temperature (< 100 ºC) (2, 4). The Figure 1. 2 represents the potential waste heat from different industrial applications based on their temperature values.

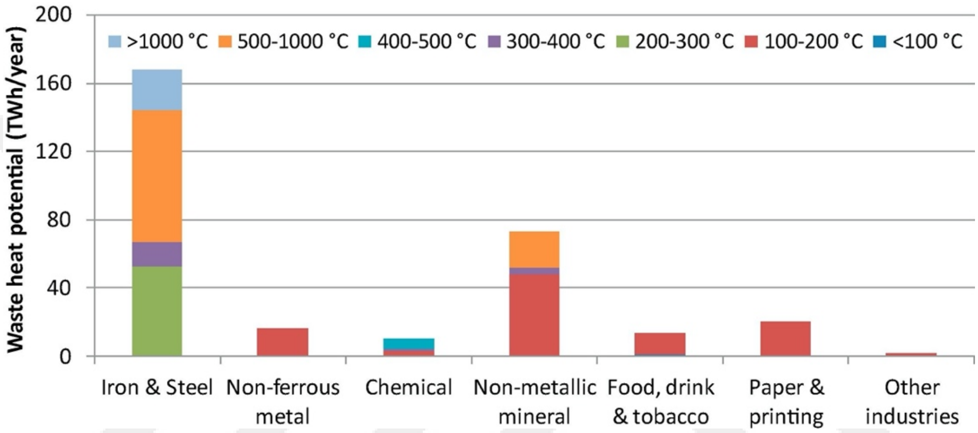

Figure 1. 2 Temperature levels and waste heat potential for different industrial applications (3).

Considering that each sector presents different potentials for waste heat, it becomes important and essential to discover waste heat recovery methods that match the specific operating temperatures unique to each sector. With respect to this, thermoelectric technology has gained increasing interest because these solid-state devices can convert different temperature differences into electricity using the Seebeck effect without any pollutants, noise, etc. (5, 6). Some state-of-art thermoelectric materials with their respective zT values are given in Figure 1. 3 as a function of temperature.

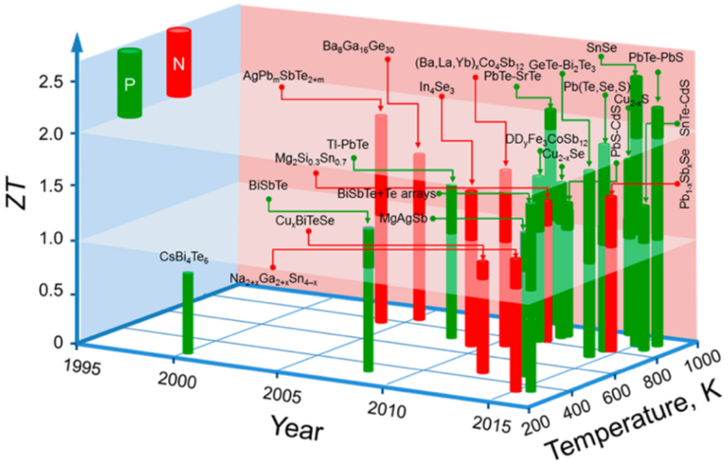

Figure 1. 3 State-of-art thermoelectric materials developed in years with zT values as a function of temperature (7).

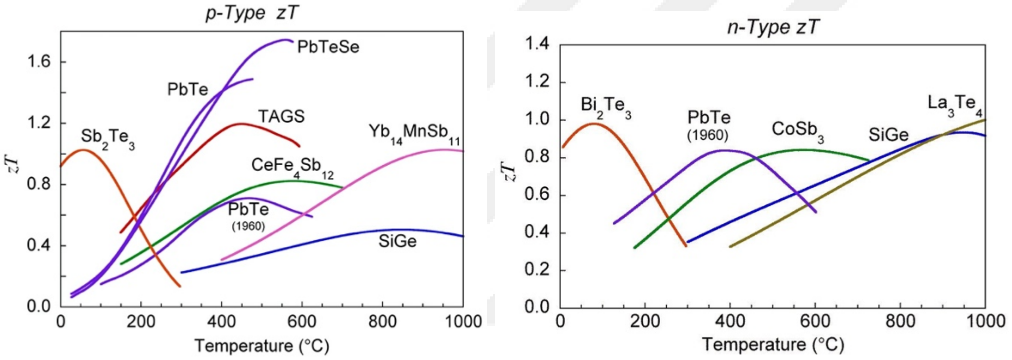

Figure 1. 4 Dimensionless figure of merit as a function of temperature for **a)** p-type materials and **b)** n-type materials (5).

As illustrated in Figure 1. 4, thermoelectric technology requires various types of thermoelectric materials with different electrical transport properties (n-type and p-type). Thus, depending on the temperature range, the amount of generated heat, and the production processes, thermoelectric materials can be selected and effectively applied for waste-heat recovery processes.

In this study, promising binary and ternary phosphides (GaP, NaSnP and LiSrP) along with $CaMg_2Sb_2$ and $CaMg_2Bi_2$ as n-type Zintl phases are discussed. The first chapter provides information on thermoelectric theory, followed by the second chapter focusing on thermoelectric phosphides and n-type $CaMg_2Sb_2$ and $CaMg_2Bi_2$ Zintl compounds. The third chapter gives information about the experimental procedures and characterization methods, while the fourth chapter presents results and discussions for those two different studies. Finally, the conclusion summarizes my entire work.

Chapter 2:

THERMOELECTRIC THEORY

The thermoelectric phenomenon describes a two-way process. Thermoelectricity produces a voltage when a material exhibits a temperature difference between both ends or when a voltage is applied to the material, creating a temperature gradient. Fundamentally, the temperature difference causes charge carriers in the material—either holes or electrons—to diffuse from the hot end to the cold end (8, 9). The thermoelectric effect is used for generating electricity or cooling devices without any hazardous effects on the environment.

2.1 Thermoelectric Effects

The first thermoelectric effect, also known as the Seebeck effect, was discovered in 1821 by the scientist Thomas Seebeck. About thirty years later, the Peltier and Thomson effects were also observed. Thomson established a relationship between these three effects and developed a thermodynamic theory for the thermoelectric effects. These effects form the main basis for the thermoelectric theory that describes the conversion between applied electric and temperature difference. This chapter mainly focuses on the thermoelectric effects and how they are used in thermoelectric devices.

2.1.1 Seebeck Effect

The Seebeck effect made the beginning of the thermoelectric effect and devices. In 1821, a German scientist named Thomas Johann Seebeck discovered a direct conversion of heat to electricity in solid materials. He attached two wires end to end to create a loop; then, he heated up one side of the junction while keeping the other end at a low temperature. Subsequently, Seebeck observed a magnetic field around the circuit. He explained the situation as magnetism occurring because of the temperature difference and named this phenomenon thermomagnetism. Another scientist named Hans Christian Ørsted reconsidered the experiment and determined that the magnetic field was not directly related to the temperature difference. Instead, he commented that the temperature difference created a voltage, and because of that, the electrical current created a magnetic field (10).

Electrons in a solid are the primary particles with a negative charge and carry an electrical current. The electrons located on the warmer side have a high concentration of Fermi energy compared to the colder side. When a temperature gradient exists, the electrons on the warmer side of the material migrate to the colder side because of the energy difference. This migration produces an electric current. This effect is named the Seebeck Effect. The Figure 2. 1 is represented the a material when it is exposed to an external temperature gradient (11).

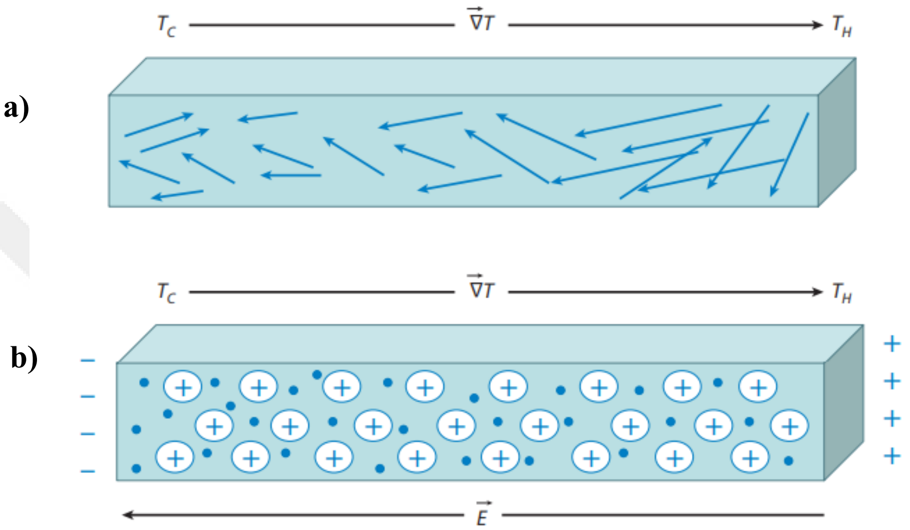

Figure 2. 1 The schematic view when a material is exposed to an external temperature gradient (12).

a) Higher energetic electrons obtained a longer mean free path.

b) The higher energetic electrons diffused to the cold side of the material until the electric field (E) is occurred and the system becomes stable.

When the material is completely uniform in its temperature difference, the electrons in the material are also stable. When a temperature difference is created between the ends of the material, the charge carriers at the warm end gain higher potential energy compared to the cold end. Because of this energy difference, charge carriers are prone to move toward the cold end. The difference in the concentration of the charge carriers on both ends of the material helps to form an electric field. The Seebeck coefficient (α), also known as thermopower, is an intrinsic material property determined by the ratio between the voltage generated and the temperature difference. Equation 1 is used to determine the Seebeck coefficient. (10, 12).

$$\alpha = \lim_{\Delta T \to 0} \frac{V}{\Delta T} \qquad \textit{Equation 1}$$

2.1.2 Peltier Effect

The Peltier effect is defined as the inverse process of the Seebeck effect. The name was given in 1834 by the French scientist named Jean-Charles-Athanase Peltier. The Peltier effect is defined as the generation of Joule Heat when an electric current passes through a junction of two different conductors. Depending on the current direction, the heat is either absorbed or rejected at the junction. (12).

This effect occurs due to the difference between the Fermi energy levels of the two materials. When two conductors with different Fermi energy levels are joined to form a connection, passing an electric current can lead to electron transitions from higher energy states to lower energy states. Alternatively, the opposite scenario may also occur. This applied electrical current heats up the cold junction and cools down the other side, reducing the temperature difference between the conductors. Additionally, when a power supply is placed externally to the circuit, it will generate an electric current and cool down one side while heating up the other, depending on the current direction. The image of this procedure can be seen in Figure 2. 2.

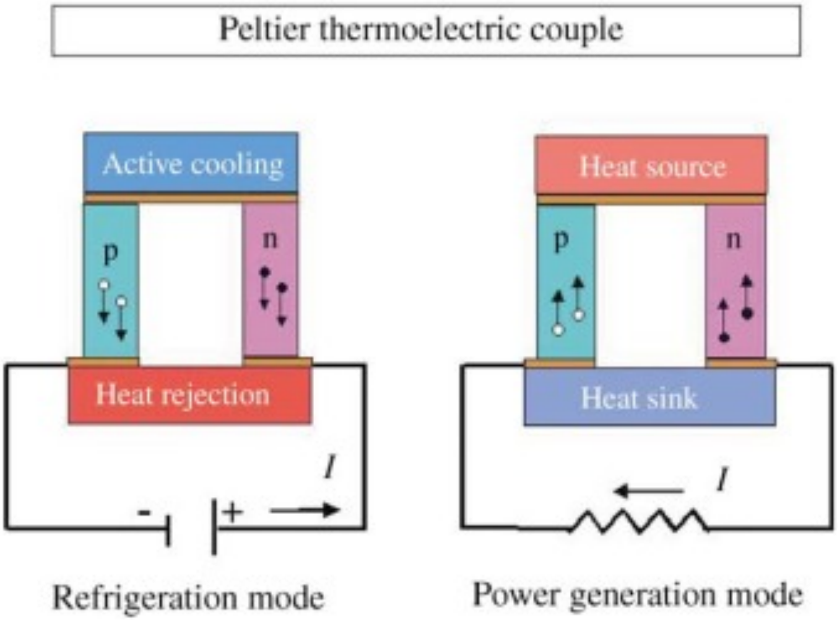

Figure 2. 2 Schematic view of a thermocouple obtained by combining an n-type and a p-type semiconductor. The image illiterates the power generation and electronic refrigeration systems (12).

The use of Peltier effect cooling systems can be achieved by using thermoelectric materials. Since the direction of the current determines the cooling and heating procedures, these thermoelectric materials can also be used for heating systems as well (11-13).

2.1.3 Thomson Effect

In 1855, the relationship between the Seebeck and Peltier effects was determined by William Thomson, also known as Lord Kelvin. He introduced the idea that when an electric current passes through a uniformly heated conductor, it can either absorb heat or release it in a unit of time. This phenomenon occurs not only on one side of the conductor but throughout the entire conductor, involving Joule heat. This knowledge was experimented with and named the Thomson Effect in 1867 (10).

Consider a conductor with sides cooler compared to the middle part. The temperature difference in the conductor differs due to the difference in electron density, creating a potential difference between the sides and ends. Let's consider a copper bar with sides named A and B. When an electrical current passes through this bar from point A to B, heat is absorbed along the A side and released on the B side. This creates a flow of heat in the direction of current flow, a phenomenon known as the Positive Thomson Effect. The positive Thomson effect is observed in metals such as Zn, Cd, and Ag. If the bar is made of iron, then the current flow generates heat absorption through the middle part to point A and heat release from the middle part to side B. This process, occurring in the opposite direction to the applied current flow, is referred to as the Negative Thomson Effect. The negative Thomson effect is observed in metals like Pt, Ni, Co, and Hg. The illustration of the process can be seen in Figure 2. 3.

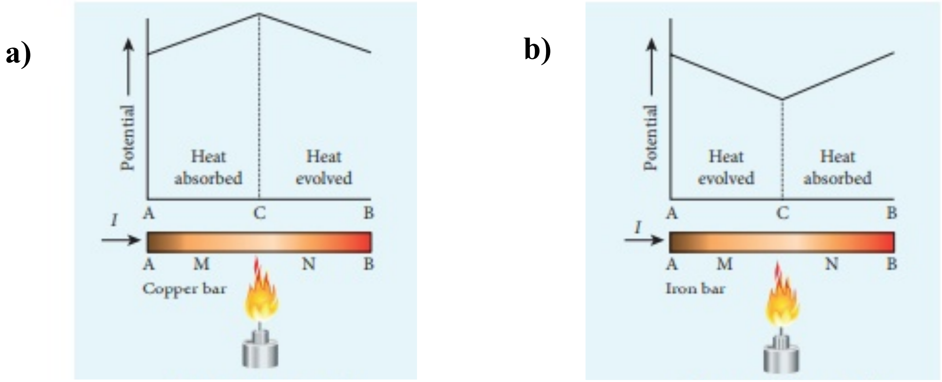

Figure 2. 3 a) The Positive Thomson effect and **b)** the Negative Thomson effect (Thomson effect - Thermoelectric Effect. (n.d.). BrainKart. https://www.brainkart.com/article/Thomson-effect_38436/).

The origin of the Thomson Effect is very similar to the Peltier and Seebeck effects. However, the difference occurs in the potential difference. In the Peltier effect, the potential difference occurs between two different conductors. In the Thomson effect, this is generated by a temperature gradient within a single conducting material. The Thomson effect differs from the others by being considered directly measurable for the materials.

2.2 Thermoelectric Efficiency and Dimensionless Figure of Merit

Thermoelectric devices convert heat into electricity. The efficiency of this process is determined by a dimensionless value named the Thermoelectric figure of merit (*zT*). To obtain the maximum efficiency from the energy conversion process (which can be either cooling or power generation) at a random point in a thermoelectric material, it can be determined by the thermoelectric figure of merit, *zT*. The *zT* value can be calculated using the given formula,

$$zT = \frac{\alpha^2.\sigma.T}{\kappa} \qquad \text{Equation 2}$$

where α is the Seebeck coefficient, σ is the electrical conductivity, T is the absolute temperature, and κ is the thermal conductivity. The thermal conductivity, represented by the letter κ, can be studied under two separate titles: lattice thermal conductivity (κ_{lat}) and electronic thermal conductivity (κ_{elec}). To achieve a high value of the zT, high values of the Seebeck coefficient, high electronic conductivity, and low thermal conductivity are essential. However, obtaining a higher zT value is not an easy task since these transport characteristics are directly related to the electronic properties of the materials. The Wiedemann-Franz Law in Equation 3 represents the direct relation between the electronic thermal conductivity and the electronic conductivity.

$$\kappa_{elec} = L\sigma T \qquad \text{Equation 3}$$

Where L represents the Lorenz factor, having a value of $2.4\text{x}10^{-8}$ $J^2K^{-2}C^{-2}$. This law shows that the electronic thermal conductivity (κ_{elec}) is directly proportional to the electrical conductivity (σ). A very similar relation is valid between the Seebeck coefficient (α) and electrical conductivity (σ) related to the carrier concentration (n). Due to the relation between the thermoelectric parameters, high α values or high σ values are not always enough to achieve a high *zT* value.

Accordingly, achieving a higher *zT* value cannot be attained by a high amount of carrier concentrations but can be achieved by optimizing the carrier concentration. Figure 2. 4 represents the *zT* value in relation to the carrier concentration.

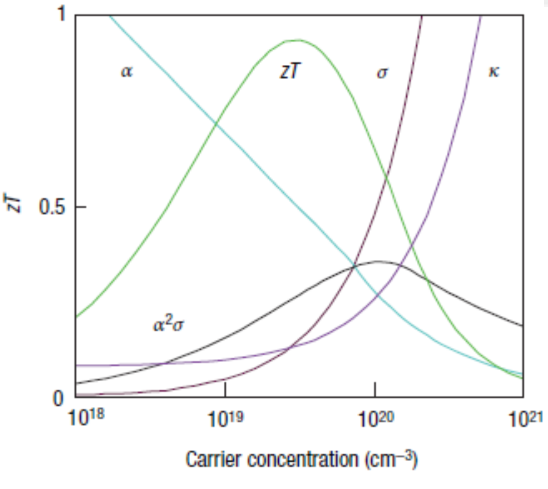

Figure 2. 4 Thermoelectric properties depended on the carrier concentration (5).

Due to the electronic contribution, thermal conductivity increases with increasing carrier concentration values. Additionally, the electrical conductivity value shows an increasing trend, while the Seebeck coefficient decreases. Materials with carrier concentrations between 10^{19} and 10^{21} per cm^3 can have optimized zT values, which are observed between well-known metals and semiconductors. Since heavily doped semiconductors fall within these values, they are attracting more attention to become thermoelectric materials (5).

2.3 Thermoelectric Modules and Generators

Thermoelectric devices serve a dual purpose. These materials can be employed for generating electricity by converting heat energy and can also effectively transform heat into cooling mechanisms through the utilization of the Seebeck and Peltier effects. Thermoelectric devices are a combination of n-type (containing free electrons) and p-type (containing free holes) legs, connected electrically in series and thermally in parallel. Figure 2. 5 is an illustration of a thermoelectric generator (5).

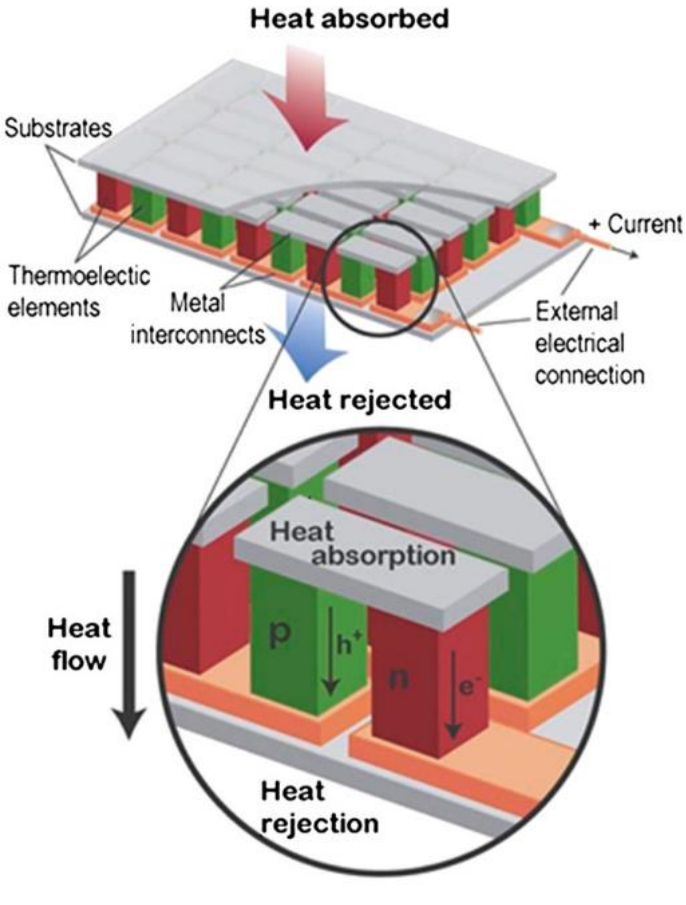

Figure 2. 5 Illustration of an Thermoelectric generator (5).

Thermoelectric modules are marked as advantageous devices for harvesting heat into electricity and also for use in cooling applications for sustainable and green energy sources. They can provide both heating and cooling effects on the same module by changing the direction of the applied current flow.

The maximum efficiency of a thermoelectric generator is denoted by the symbol η. The general formula η is given in Equation 4.

$$\eta = \frac{\Delta T}{T_h} \frac{\sqrt{1+ZT}}{\sqrt{1+ZT} + {}^{T_C}/_{T_h}} \qquad \text{Equation 4}$$

The Th, Tc and ZT are representing the temperature of the hot end, temperature of the cold end and average zT value between the ends, respectively. The first term in the Equation 4 representing the Carnot efficiency and the maximum efficiency of any thermoelectric generator restricted by this factor.

Good thermoelectric materials are those that have the potential for high zT values. The potential for high zT values is determined by the thermoelectric quality factor, denoted as B. The thermoelectric quality factor can be calculated using Equation 5.

$$B = \frac{8\pi k_B \, (2m_e)^{3/2}}{3eh^3} (k_B T)^{5/2} . \frac{\mu_w}{\kappa_L} \qquad \text{Equation 5}$$

The terms k_B, e, m_e, μ_w, h and κ_L represent the Boltzmann constant, charge of an electron, mass of a free electron, weighted mobility, Planck's constant, and lattice thermal conductivity, respectively. The equation represents the quality factor related to electronic properties assigned by the weighted mobility and thermal contribution defined by the lattice thermal conductivity. The thermoelectric quality factor can also be denoted by Equation 6.

$$B = \frac{B_E T}{\kappa_L} \qquad \text{Equation 6}$$

The term B_E represents the electronic contribution to the quality factor. The term B_E is independent of temperature and doping. Both the quality factor and its electronic contribution are used to determine the highest zT values for potential thermoelectric materials. Any improvement in the electronic contribution will increase B_E or the μ_w at a certain temperature value, while improvements in the thermal properties will lower the κ_L value. The weighted mobility, μ_w, is directly proportional to the electronic structure and phonon scattering of the material, both of which depend on temperature, making B_E a temperature-independent value. Improvements in thermoelectric materials, besides doping, affect the $^{\mu_w}/_{\kappa_L}\}$ ratio. Therefore, thermoelectric materials can be well described without any re-optimization of charge carrier concentrations to compare the materials with the factor B_E (14-18).

Figure 2. 6 represents the energy conversion efficiencies of power generation systems. To improve the conversion efficiency of the systems, a high temperature gradient and an improvement of the ZT_{avg} value are crucial. Compared to other energy conversion technologies, thermoelectric materials have low ZT_{avg} values. The highest ZT_{avg} value is obtained by coal-fired power generation technologies. The theoretical efficiency of thermoelectric devices can reach up to 8.7%, a value close to the efficiency of geothermal power. In this figure, the efficiency of thermoelectric devices, with a ZT_{avg} value in this temperature range of around 1, is approximately 5.6% for theoretical efficiency. Thus, improving the zT value of thermoelectric materials is a substantial task. However, thermoelectric devices are used in various applications, including power generators, cooling systems, deep-space probes, remote sensors, and refrigerators (19, 20).

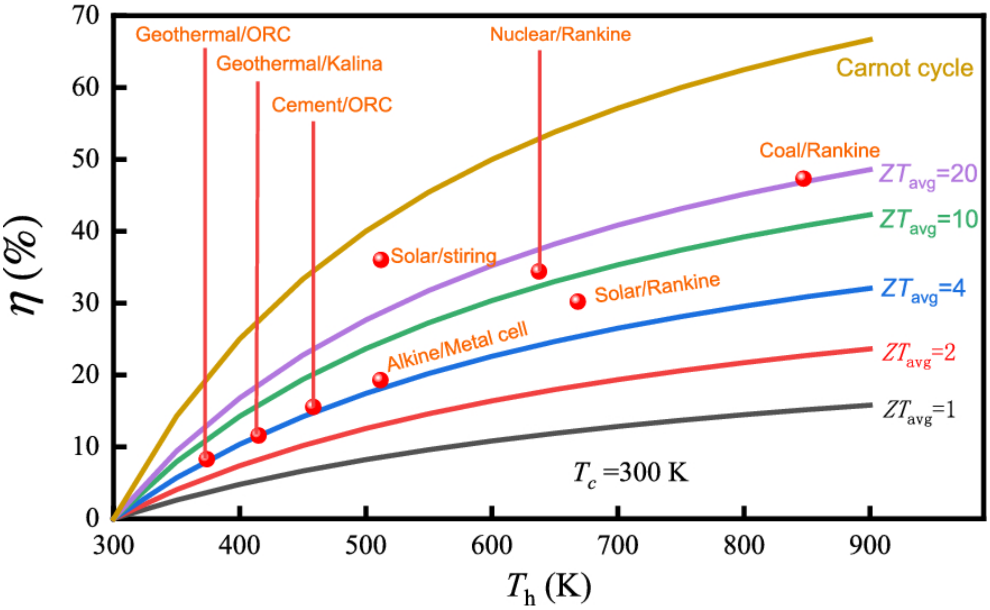

Figure 2. 6 Hot-side temperature dependence of the TE energy conversion efficiency for different ZT_{avg} values (20).

Thermoelectric material properties and regulations for approaching higher *zT* values can be stated as follows (21):

- Narrow bandgap materials are desirable for thermoelectrics as they can facilitate higher carrier mobility while simultaneously ensuring low thermal conductivity. The bandgap width influences electronic properties, such as the density of states near the Fermi level, which directly impacts thermoelectric performance.

- Carrier mobility is a major factor for efficient charge transport in thermoelectric materials. Higher carrier mobility enables enhanced electrical conductivity, contributing to improved thermoelectric properties. Achieving high carrier composition of the material.

- Lower thermal conductivity helps maintain a higher temperature gradient, thereby improving energy conversion efficiency.

- Thermoelectric materials ideally exhibit a combination of phonon-glass and electron-crystal behavior. The electrical properties resemble those of a crystalline material, allowing efficient charge transport. On the other hand, the thermal properties resemble those of an amorphous glass or glass-like material, resulting in low lattice thermal conductivity.

- Incorporating heavy elements into the material structure is an effective approach to reducing lattice thermal conductivity. This reduction is achieved through increased phonon scattering, as heavier elements tend to have stronger interactions with phonons, impeding their movement and reducing thermal conductivity.

- Complex crystalline structures can contribute to proper charge mobility. By introducing complex regulations within the material, the mean free path of free electrons is reduced, leading to enhanced charge transport. This can be attributed to the increased scattering events that occur within the complex structure, improving overall charge mobility.

2.4 Thermoelectric Transport Properties

The primary obstacle currently is enhancing the thermopower of materials while preventing any negative impact on their electronic conductivity.

2.4.1 Seebeck Coefficient

Seebeck coefficient, represented either by S or α, is a material property obtained from the Seebeck effect and stated as temperature gradient between two points in a semiconductor or a conductor generating an amount of voltage. The Seebeck coefficient is the measure of this voltage amount and expressed in units of V/K or $\mu V/K$.

The Seebeck coefficient, represented either by S or α, is a material property obtained from the Seebeck effect and is stated as the temperature gradient between two points in a semiconductor or conductor, generating a certain amount of voltage. The Seebeck coefficient is the measure of this voltage amount and is expressed in units of V/K or $\mu V/K$ (22) (6). To calculate the Seebeck coefficient of degenerate metals and heavily doped semiconductors, the Mott Formula (23) in the Equation 7 is used,

$$S = \frac{8\pi^2\kappa_B^2}{3eh^2} m * T \left(\frac{\pi}{3n}\right)^{2/3} = \frac{\pi^2}{3}\left(\frac{\kappa_B^2 T}{e}\right) \left(\frac{d \ln \sigma(\epsilon)}{d\epsilon}\right)_{\epsilon=0} \qquad \text{Equation 7}$$

Where κ_B, $m*$, n, e, h and $\sigma(\epsilon)$ represent the Boltzmann constant, density of states of effective mass, carrier concentration, electron charge, Planck's constant, and the electronic conductivity as a function of Fermi energy, respectively. In Equation 7, carrier concentration and band structure have a major impact on the Seebeck coefficient. The Seebeck coefficient measures the change in electrical conductivity above and below the Fermi level by calculating the logarithmic derivative of σ with respect to E, and it also measures the asymmetry of electronic structure and scattering rates near the Fermi level. For this reason, the interest lies in generating complexities within a small interval near E_F in either electronic structure or scattering rates or even both. Semiconductors with complex structures can be a good alternative for materials with complex electronic structures.

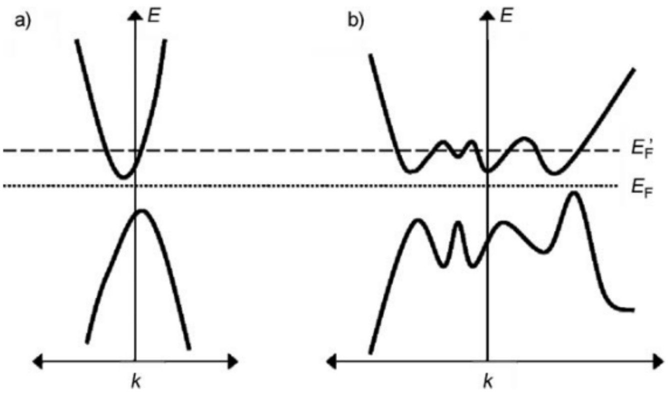

Figure 2. 7 Example of **a)** simple and **b)** complex band structure semiconductors (20).

Figure 2. 7 represents a semiconductor structure with a single valley in both the valence band and the conduction band, while the second one represents a complex structure with many valleys in both its valence and conduction bands. Simply put, the Seebeck coefficient of the complex structure has higher S values since it is directly proportional to the number of valleys in the band structure.

To obtain a higher value of thermal power in a thermoelectric generator, a single charge carrier should dominate the transport. The combination of p-type and n-type carriers will reduce the amount of voltage generated in a temperature gradient. Thus, conventionally good thermoelectric materials are made from degenerate metals and heavily doped semiconductors with Fermi levels near the edge of the bandgap to achieve single carriers and high carrier mobility (24).

2.4.2 Electrical Conductivity

Electrical conductivity is one of the material properties representing the measure of the material's ability to conduct electricity using either holes or electrons. It is commonly signified by the Greek letter σ (sigma), but κ (kappa) (in electrical engineering) and γ (gamma) are sometimes used. The SI unit of electrical conductivity is siemens per meter (S/m). According to Ohm’s law, electrical conductivity can be represented by Equation 8.

$$\frac{V}{\ell}\,\sigma = \frac{I}{A} \qquad \text{Equation 8}$$

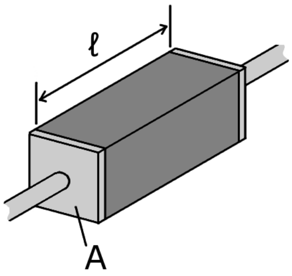

Figure 2. 8 Representative image of a resistor.

Where ℓ is the length in cm, and A is the cross-sectional area in cm^2 of the resistor. The representative image of a resistor is given in Figure 2. 8. The electrical field, , E (V/cm), is represented by the division of voltage by the length of the resistor, $\left(\frac{V}{\ell}\right)$, and the current density, J (A/cm^2), can be represented by the division of current per unit area of the resistor, $\left(\frac{I}{A}\right)$. By replacing these parameters, the electrical conductivity can be expressed by the Equation below,

$$J = \sigma . E \qquad \text{Equation 9}$$

In other way the current density can be represented as;

$$J = n . q . \bar{v} \qquad \text{Equation 10}$$

Where n is the number of charge carriers (carriers/cm^3), q is the charge in each carrier (1.6×10^{-19} C) and, ν is the average drift velocity (cm/s). By combining the Equation 9 and Equation 10 the electrical conductivity can be represented by a new formula,

$$\sigma = n . q . \frac{\bar{v}}{E} \qquad \text{Equation 11}$$

In Equation 11, the term $\left(\frac{\bar{v}}{E}\right)$ represents the mobility of the carriers, μ (cm^2/Vs), For metals, the mobility is related to electrons, while for semiconducting materials, the mobility is related to both electrons and holes. Using the mobility parameter, electrical conductivity can be represented by Equation 12.

$$1/\rho = \sigma = n . q . \mu \qquad \text{Equation 12}$$

The above equation describes the electrical conductivity affected by the charge carriers in the material, and the mobility of the charge carriers depends on the material type (25). However, in the semi-classical Drude model found in the 1900s, it is stated that the mobility has a direct relation between the effective mass of electrons m_e^*, scattering time (also noted as relaxation time, τ), and the charge of the electrons. By using the Drude model, the electrical conductivity can be represented by Equation 13 (26, 27),

$$\sigma = \frac{n.e^2.\tau}{m_e^*} \qquad \text{Equation 13}$$

The equation above states that the optimization of electrical conductivity is related to the scattering mechanism, charge carriers of the material, and the effective mass of the charge carriers.

2.4.3 Thermal Conductivity

Thermal conductivity, denoted by κ, is a material property that measures its ability to conduct heat through charge carriers (either electrons or holes), lattice waves (phonons), electromagnetic waves, spin waves, or other excitations (6, 28). To express thermal conductivity, Fourier's Law is used:

$$q = -\kappa \cdot \frac{d\mathrm{T}}{dr} \qquad \text{Equation 14}$$

Here, q represents the density of heat current flow through the material (J/m.s), $\left(\frac{dT}{dr}\right)$ is the temperature gradient (K/m) of the material, k is the thermal conductivity (W/m.K), and the negative sign in the formula represents the direction of heat flow from the hot side of the material to the cold side. As seen from the *zT* formula given in Equation 2, the decrement in thermal conductivity results in an increase in the value of *zT* (29). The heat transported by electrons and phonons is considered as independent variables. Thus, the thermal conductivity equals the summation of two parameters: the electronic thermal conductivity (κ_e) and the lattice thermal conductivity (κ_ℓ).

$$\kappa = \kappa_e + \kappa_\ell \qquad \text{Equation 15}$$

2.4.3.1 Electronic Thermal Conductivity

In conductive materials or metals, heat transport is primarily carried out by electron carriers, while the contribution of phonon carriers can be neglected (28). This behavior is supported by experimental evidence known as the Wiedemann-Franz Law, which describes the relationship between electronic thermal conductivity, κ_e , electrical conductivity, σ, and absolute temperature T as:

$$\kappa_e = L_o.\sigma.T \qquad \text{Equation 16}$$

Where L_o, σ, T represented the Lorentz number, electrical conductivity and, absolute temperature respectively (28) . The Lorentz number can be described by the Equation 17 below.

$$L = L_o = \frac{(\pi K_B)^2}{(3e^2)} = 2.44 \times 10^{-8}\ {V^2}/{K^2} \qquad \text{Equation 17}$$

Here, K_B represents Boltzmann's constant, e is the charge of the electron, and L is the Sommerfeld value, respectively. Thus, from the Equations 16 and 17 given above, electronic thermal conductivity (κ_e) can be related to the electrical conductivity (σ) and the temperature (T).

Given that increasing the electrical conductivity will produce an increase in the electronic thermal conductivity but decrease the thermopower value, it is concluded that the electronic thermal conductivity and electrical conductivity values are independent properties.

2.4.3.2 Lattice Thermal Conductivity

Lattice thermal conductivity occurs due to lattice vibrations, which are named phonons. Unlike κ_e, lattice thermal conductivity provides thermal conduction in insulating materials. κ_ℓ can be expressed by the phonon gas theory given by Equation 18.

$$\kappa_\ell = \frac{1}{3}\left(C_v V_s \lambda_{ph}\right) \qquad \text{Equation 18}$$

Where Cv, Vs, and λ_{ph} are the specific heat capacity of the lattice, sound velocity, and phonon mean free path, respectively. The Seebeck coefficient, electrical conductivity, and electronic thermal conductivity are connected with each other through carrier concentration and the effective mass of electrons. However, the lattice thermal conductivity is an independent parameter. Thus, increasing the power factor by decreasing the thermal conductivity is a promising regulation for the thermoelectric industry (29).

Also, the Equation 18 can be expressed differently as;

$$\kappa_{\ell} = \frac{\pi^2 . n . K_B^2 . T . \tau}{3 . m_e} \qquad \text{Equation 19}$$

As seen from Equation 19, the parameter λ_{ph}, which represents the mean free path or the maximum distance a phonon can travel, can be affected by scattering events. Therefore, to reduce the value of κ_{ℓ}, one can reorganize the unit cell structure, design a scattering mechanism, and produce an interface layer constructed with heavily bonded atoms. (30). The Figure 2. 9 is representing the phonon scattering events.

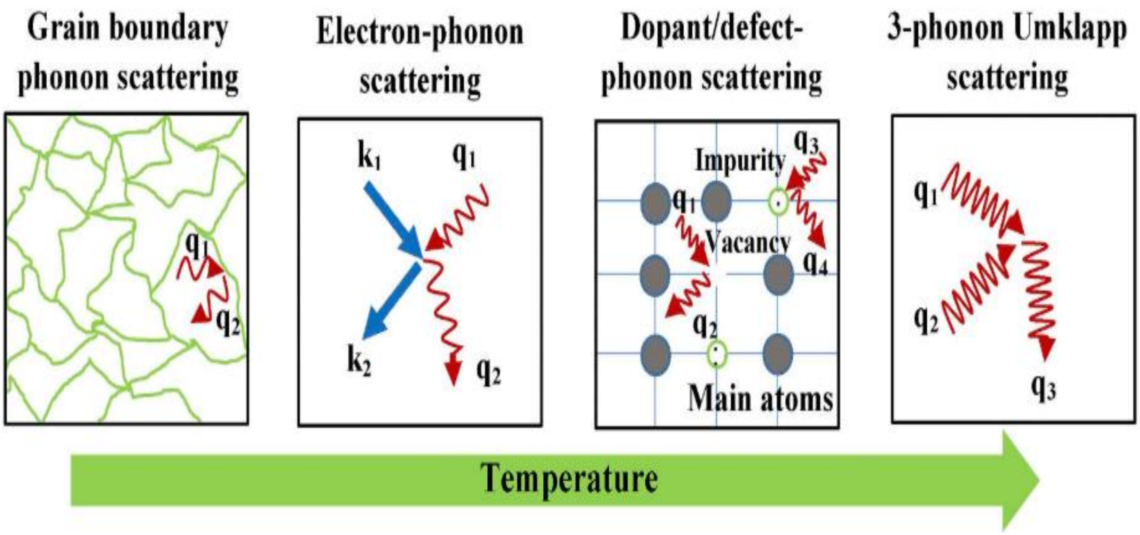

Figure 2. 9 Some phonon scattering events (31).

Chapter 3:

THERMOELECTRIC MATERIALS

3.1 Thermoelectric Phosphorus

3.1.1 Elemental Phosphorus

Phosphorus is the 15th element and is located in group five on the periodic table. It can form solid compounds with nearly all elements in the periodic table due to its high bonding potential. Over 90% of phosphorus exists in the form of metal phosphide compounds in the Earth's core (32). Phosphorus has a variety of physical states, with some considered stable. Hundreds of years ago, three main allotropic alterations of elemental phosphorus were determined. These allotropes are known as White, Black, and Red phosphorus. Further modifications of these allotropes enable the obtaining of highly dense and chemically stable forms of phosphorus. In 1669, the scientist named H. Brand made the start by discovering white phosphorus, which is the pyrographic and well-characterized form of the element. In 1847, A. Von Schrotter determined the well-known and commercially popular form, red phosphorus. Finally, in 1914, P. W. Bridgeman determined black phosphorus (33, 34).

3.1.2 White Phosphorus

White phosphorus is the oldest known form of phosphorus allotropes. This form of phosphorus is highly volatile and reactive. Additionally, it can be converted to liquid and vapor phases. White phosphorus is soluble in organic solvents; however, it is not soluble in water. The structure of white phosphorus is tetrahedral with a soft waxy texture and transparent crystals. It is highly air-sensitive and flammable when exposed to air, as its structure can burn in both oxygen and carbon dioxide environments. The boiling point is at 552K, and the melting point is at 317K to form a metastable liquid.

In 1953, scientists named Corbridge and Lowe determined that, at ambient conditions, white phosphorus has a cubic structure with a=18.51 Å and a density of 1.83 g/cm^3. The structure of white phosphorus can transform to a hexagonal form (β form) at 64 ºC, and under a pressure of 11.6 atm, the structure becomes monoclinic (γ form) with an even higher density of 1.94 g/ cm^3 (33, 34).

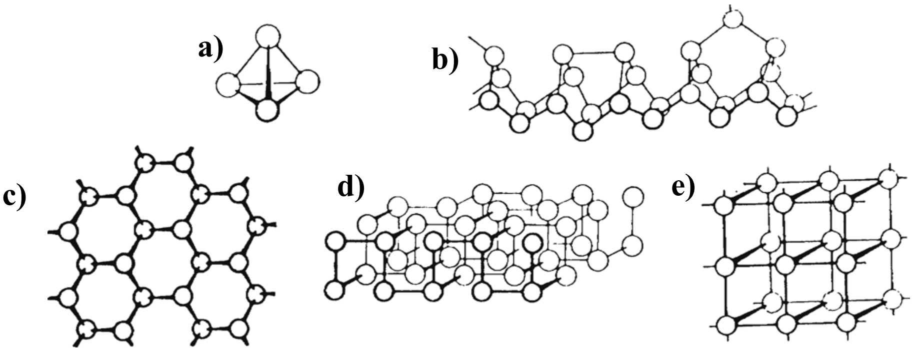

Figure 3. 1 Structures of elemental phosphorus. **a)** white P_4, **b)** violet P_n, **c)** rhombohedral black P_n **d)** orthorhombic black P_n and**, e)** cubic black P_n respectively (33).

3.1.3 Black Phosphorus

Thermodynamically, black phosphorus is the most stable form among the phosphorus allotropes. Black phosphorus has three different crystal modifications and an amorphous form. Under atmospheric conditions, the preparation of black phosphorus can result in amorphous and orthorhombic crystal structures. However, these structures can change to rhombohedral and cubic structures when exposed to very high pressures. The stable structure of black phosphorus is indicated as orthorhombic. Unlike white phosphorus, black phosphorus has a polymeric structure, is non-flammable, and has low vapor pressure properties. The appearance and texture of orthorhombic black phosphorus bear similarities to graphite due to its continuous double layer, with each phosphorus atom forming three bonds at a 2.23 Å bond length. (33, 34).

3.1.4 Red Phosphorus

Red phosphorus is a group of phosphorus forms that are more or less red in color, with densities between 2.0 to 2.4 g/cc and melting points between 585-610 ºC. In terms of stability conditions, red phosphorus is placed between white and black phosphorus. Despite this, red phosphorus can easily form compounds with oxygen, sulfur, halogens, and metals, even though the reactions are vigorous. Red phosphorus also has the most complex structure of all phosphorus allotropes. This phosphorus form is low in solubility. Because of this property, red phosphorus can only be obtained in the form of powder or lumps. The structure behaves like a polymer, and unlike white phosphorus, it is not flammable. However, at 240 ºC, red phosphorus can spark, but the form is non-toxic. The preparation of red phosphorus can be done either by applying heat around 260ºC to white phosphorus, 125ºC to black phosphorus, or at 550 ºC in the crystallization process of black phosphorus. Different synthesis methods will alter the structure and properties of red phosphorus (33, 34). The Figure 3. 1 represented structures of phosphorus.

3.1.5 Introduction to Thermoelectric Metal Phosphides

Phosphides represent a group of chemical compounds where elemental phosphorus is the primary element combined with a less electronegative element or elements, mostly metals. In 1789, Peltier started studying metal phosphides, and in 1832, the first Metallophosphorus complex was reported. In the 1930s, the first experimental use of Metallophosphorus compounds began. All metal phosphides have crystal structures, and their physical and chemical properties vary. Nearly all metals can form compounds with phosphorus; because of that, the dedicated amount of binary metal phosphides is over 200. In addition to binary compounds, there are also ternary phosphides and mixed metal phosphides.(33).

To design better thermoelectric materials, one can employ techniques such as phonon-glass electron-crystal engineering, nano structuring, manipulation of electronic band structures, and enhancement of experimental characteristics related to electrical and heat transport. However, to qualify as a thermoelectric material, it is necessary to satisfy criteria such as good electrical and thermal conducting properties, long-term stability, mechanical strength, and matching thermal expansion with the n-type and p-type legs that constitute the thermoelectric generator.

Electronic properties are intertwined with carrier concentration and the electronic band structure. Electronic band structure engineering is utilized to achieve high-performance thermoelectric materials by creating multi-valley degeneracy in the electronic band structure and optimizing carrier concentrations. Additionally, thermal conductivity needs to be minimized through nano structuring, which involves creating point defect scattering and alloy scattering. Increasing phonon scattering leads to higher electrical resistivity and lower intrinsic thermal conductivity. As a result, materials with large unit cells and complex structures may exhibit lower thermal conductivity. (35, 36).

Metal phosphides are considered good thermoelectric materials because of their excellent electrical properties, but they have never been used due to their high thermal conductivity values. Nowadays, metal phosphides are rapidly gaining attention as potential thermoelectric materials. Chemically, the diverse accessible anionic oxidation states of phosphorus enable a variety of structure types and chemical bonds in these structures. This property allows phosphides to have a high degree of covalent bonding and polyanion formation, resulting in complex chemical structure types. These complex structures lead to low lattice thermal conductivity, and the low atomic mass of the phosphorus atom creates a low zT value. Additionally, phosphides are chemically versatile and abundant in Earth's crust. This property makes them economically favorable. Thus, scientists have revealed that metal phosphides can be promising candidates for high-performance thermoelectric materials with a semiconducting or semimetallic band structure. (35, 36).

Recent studies have shown that metal phosphides, especially phosphide skutterudites, exhibit high experimental power factor ($P=\alpha^2/\rho$) values. However, their thermoelectric performance is hindered by their high thermal conductivity. Similarly, black phosphorus with a two-dimensional structure indicates similar performance issues with high thermal conductivity values, leading to a low zT (37). However, some metal phosphides, such as $Ag_6Ge_{10}P_{12}$, have demonstrated that metal phosphides can be promising candidates for thermoelectric materials with high zT values due to their complex crystal structure and enhanced electronic properties (38).

In particular, the complex structure of the $Ag_6Ge_{10}P_{12}$,seen from Figure 3. 2, composition reveals that the electrical and thermal properties of some metal phosphides indicate high thermoelectric performance (39). Metal phosphides with compositions of XP and XYP (GaP, NaSnP, and SrLiP), where X is a metal and Y is an alkali metal, have high predicted power factors and low thermal conductivity values, as revealed by the determination of thermoelectric performance with thermal conductivity model calculations. The previously given Figure 1. 3 is a representative image of materials with high zT values, surpassing state-of-the-art thermoelectric materials.

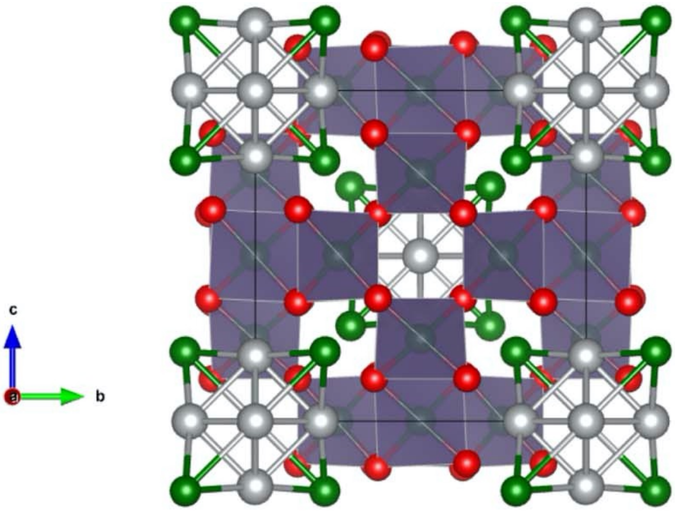

Figure 3. 2 Christal Structure of phonon-glass electron-crystal of $Ag_6Ge_{10}P_{12}$ thermoelectric material (35).

3.1.6 Determination of the Ternary Metal Phosphides

Scientists have conducted repeated experiments since the 1960s to discover new thermoelectric materials or improve the properties of current ones. To overcome the unnecessary and time-consuming repetition of experiments, computational tools are used. The Materials Project database has the largest selection of materials with electronic transport properties. From this database, metal phosphide compounds are revealed to be promising thermoelectric materials (36). Comparisons of the electronic and thermal properties of the metal phosphides, XP, and XYP compositions show an n-type power factor due to their multi-valley degeneracy and low lattice thermal conductivity. These properties are higher than the current materials categorized as effective thermoelectric materials (i.e., PbTe and Bi_2Te_3). Based on these calculations, GaP, NaSnP, and SrLiP are chosen to determine the transport properties and mechanical properties of the metal phosphides. The Figure 3. 3 represented the crystal structure of these metal phosphides.

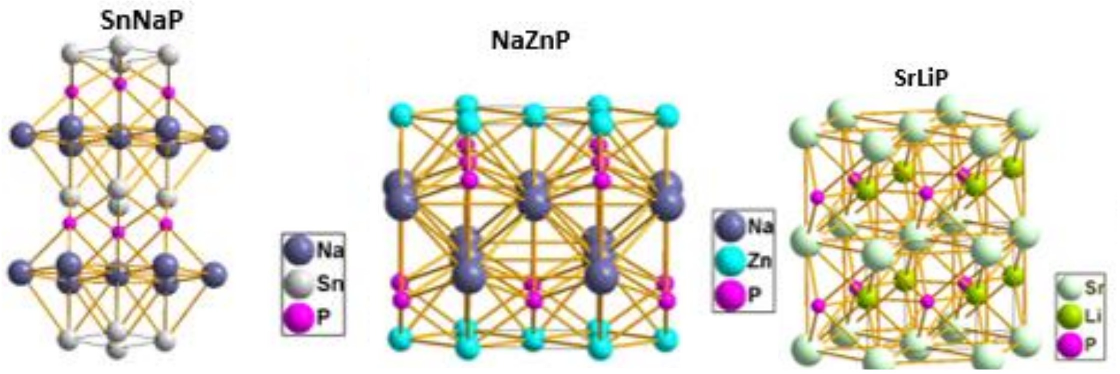

Figure 3. 3 Crystal structure of XYP composition metal phosphides (NaSnP, NaZnP and SrSnP)

3.1.6.1 Electronic Band Structure and Thermoelectric Performance of NaZnP

Computational methods have determined that NaZnP ternary phosphides are promising materials for effective thermoelectric applications. Figure 3. 4 represented the crystal structure of NaZnP. NaZnP has a direct band gap with semiconducting behavior, making it a good option for photovoltaic applications. This composition crystallizes in the $\alpha, \beta \; and \; \gamma$ phases with a tetragonal Cu2Sb-type structure under ambient conditions. Additionally, it can transition from the tetragonal Cu2Sb-type to cubic structures in the $\alpha \; (or \; \beta)$phase under high pressures. In the Cu_2Sb-type structure, NaZnP is determined to be a direct band gap semiconducting material.

The transport properties of NaZnP are determined by the electronic band structure. Figure 3. 5 shows that the NaZnP ternary phosphide has a direct band gap, where the upper valence band and lower conduction band are located at the center of the Brillouin zone, having a band gap value of 1.80 eV.

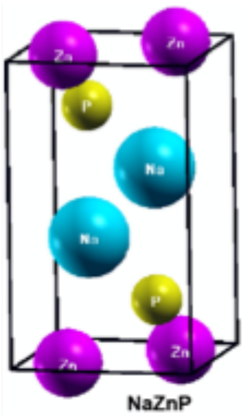

Figure 3. 4 Crystal structure of NaZnP (40).

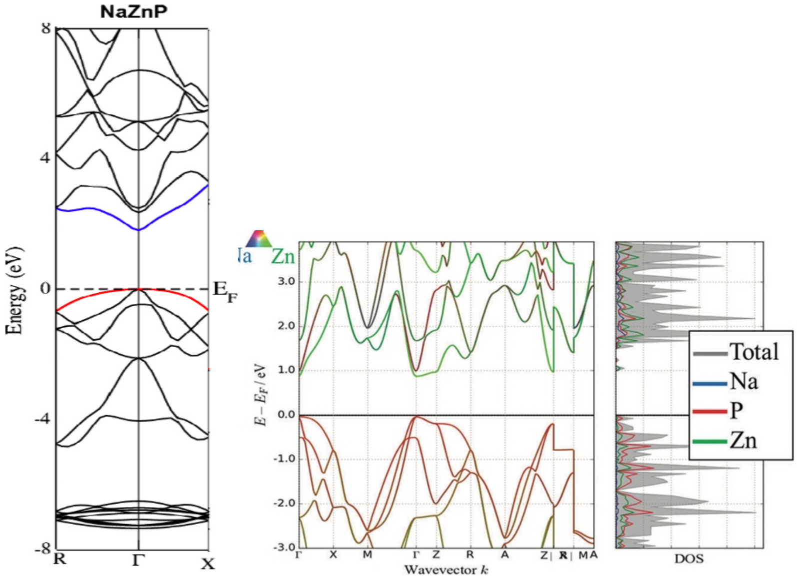

Figure 3. 5 The calculated electronic band structure of NaZnP (36, 40)

From the semi-classical Boltzmann theory, NaZnP exhibits higher electrical conductivity with an n-type semiconducting behavior. Additionally, the composition has a minimum thermal conductivity (40).

As mentioned earlier, electrical conductivity is directly related to the charge carrier concentrations. This can be achieved by increasing temperature values to enhance mobility or by doping with elements that can generate extra charge carriers. Reshak and Aulucuk compared the NaZnP compound with NaZnAs and NaZnSb ternary phases. In Figure 3. 6, they obtained computational results indicating that the highest carrier concentration is achieved by the NaZnP ternary phase. They also reported that the highest electrical conductivity can be observed in the NaZnP compound (40).

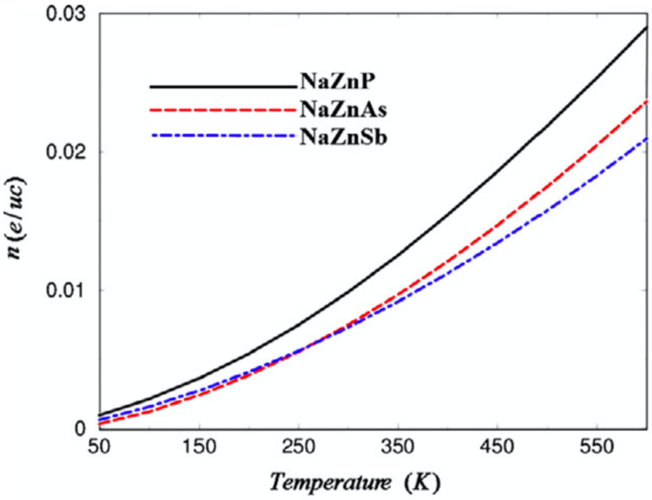

Figure 3. 6 Comparison of the carrier concentration values as a function of temperature (40)

The electrical conductivity and Seebeck coefficient for NaZnP at 300K and 600K are also calculated. As seen in Figure 3. 7, the electrical conductivity has the highest value (5.4 x 10^{20} (ohm.ms)$^{-1}$) compared to other ternary phases. The Seebeck value for NaZnP exhibits two different peak values at 300K, reaching -290 µV/K for both n-type and p-type, respectively(40).

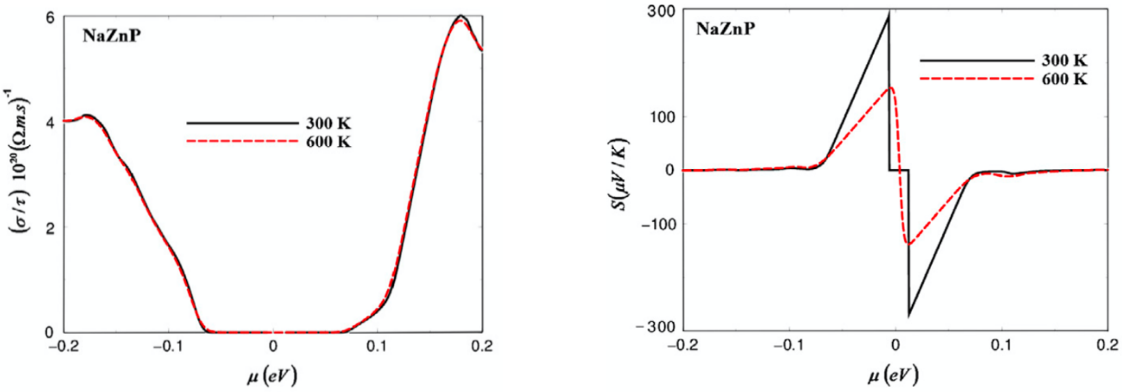

Figure 3. 7 Calculated electrical conductivity values and Seebeck coefficient values of NaZnP as a function of chemical potential at constants temperatures between 300K and 600K (40).

3.1.6.2 Electronic Band Structure and Thermoelectric Performance of SrLiP

SrLiP, a ternary phosphide composition, crystallizes in a hexagonal crystal structure with the P63/mmc space group. Figure 3. 8 represents the unit cell of SrLiP, which contains one alkaline earth metal Sr, two Li atoms, and two P atoms. The thermoelectric properties of SrLiP have been calculated using classical Boltzmann transport equations and also by self-consistent phonon theory. The structure of SrLiP exhibits different characteristics in various directions of the α (or β) and γ axes. This unique property of SrLiP can be classified as an anisotropic material with relatively strong anharmonicity.

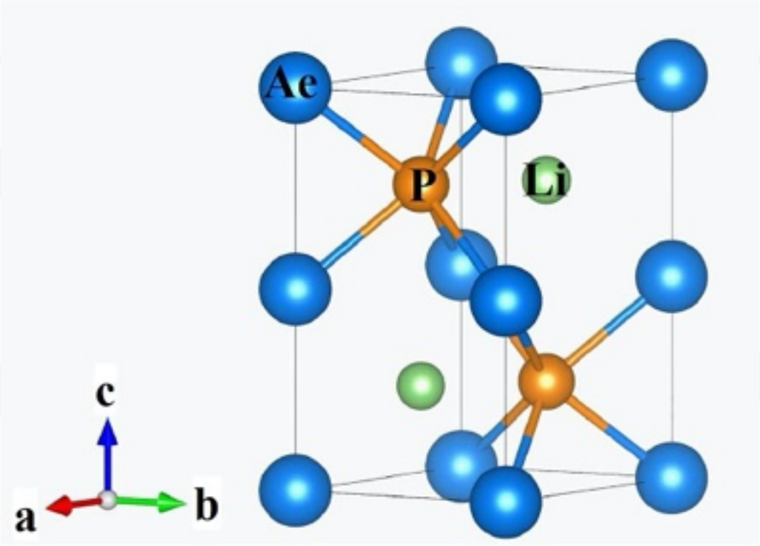

Figure 3. 8 Crystal structure of SrLiP. Blue atoms representing Sr, orange atoms representing P and green atoms repressing Li (41).

Utilizing the Born-Huang criteria, the stability analysis of the hexagonal structure of SrLiP at temperatures of 300 K, 600 K, and 900 K confirms that it is mechanically stable. Subsequently, calculations of the bulk modulus (B), Young's modulus (E), and shear modulus (G) demonstrate that the SrLiP composition has good strength. The harmonic phonon dispersion curve of SrLiP is given in Figure 3. 9. The absence of any imaginary frequency lines in the result indicates that the system is dynamically stable. Additionally, at the M-point, there is a softening representing low lattice thermal conductivity.

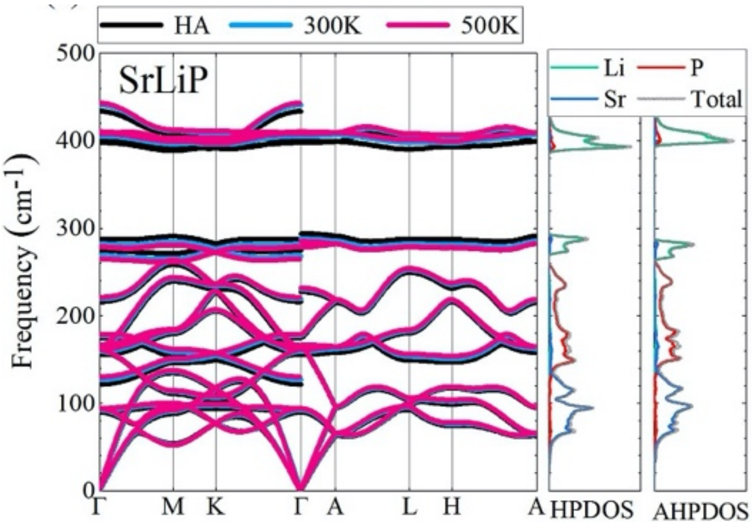

Figure 3. 9 Harmonic phonon dispersion curves and phonon density of states (HPDOS), non-harmonic phonon dispersion curves and phonon density of states (AHPDOS) for SrLiP (41).

The lattice thermal conductivity values of SrLiP are determined at different temperatures. The conductivity value decreases with increasing temperature values. Additionally, the anisotropy of the structure yields different values along different crystal axes. At room temperature, the lattice thermal conductivity of SrLiP is 2.98 98Wm^{-1}K^{-1} in the α (and β) axis and 2.87 98 Wm^{-1}K^{-1} for the γ-axis.

The band gap of SrLiP is 2.02 eV, and electronic band structure calculations for SrLiP reveal that the structure behaves like an indirect bandgap semiconductor, with the conduction band minimum at the M point and the valence band maximum at the Γ point, as shown in the Figure 3. 9. The valence band maximum is contributed to by the P atoms, while the conduction band minimum is associated with Sr atoms. As observed in Figure 3. 10, the Li atoms show a high degree of localization due to the loss of all valence electrons. Therefore, Li atoms do not contribute to the Fermi level. The high electron transport property of the structure indicates high electrical conductivity and high carrier concentrations. Additionally, the valleys near the conduction band minimum provide a large density of states, indicating a good Seebeck coefficient value (41). Visual simulation for determine electron localization of SrLiP can be seen in Figure 3. 11.

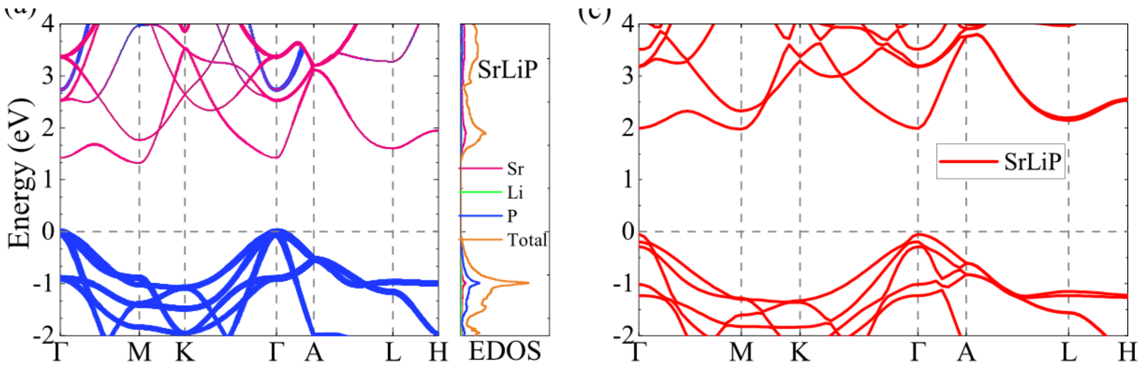

Figure 3. 10 Calculated projected electronic band structure and corresponding electronic density of states (EDOS) for SrLiP (41).

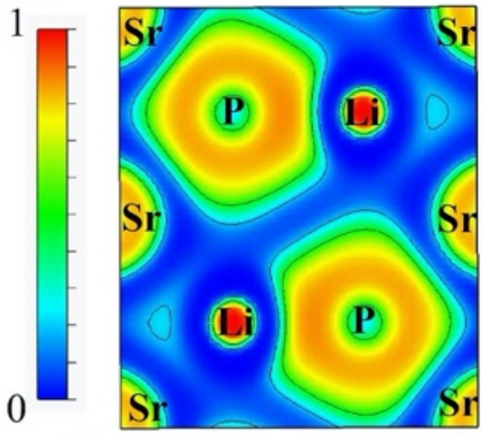

Figure 3. 11 VESTA simulation to visualize SrLiP projected electron localization function (ELF) on the (110) Plane (41).

3.1.6.3 Electronic Band Structure and Thermoelectric Performance of GaP

The semiconducting III-V phosphides have gained considerable attention in solid-state physics due to their good electronic properties (42). GaP, one of the members of this group, has gained popularity due to its high thermal conductivity values and wide energy band gap (43). In ambient conditions, GaP crystallizes in a zinc-blend (zb) structure (44). However, several crystal structures like wurtzite (wz), rock salt phase (NaCl) are also reported. Arbouche et al. (45) sed the full-potential augmented plane-wave plus local orbitals (FP-LAPW+lo) method to calculate the phase transition of zb-GaP under high pressures. The calculations demonstrated that zb-GaP has the most stable structure.

The $P6_422$ P6422 space group GaP has a hexagonal structure with a=b=3.899Å a=b=3.899 Å and c=8.79 Å c=8.79Å with a 2.419 Å bond length. The hexagonal structure of GaP has a density value of 4.446 g/cm³, higher compared to the cubic structure, because the volume per molecule in the hexagonal phase is smaller (45). In Figure 3. 12, the hexagonal and cubic structured GaP are shown.

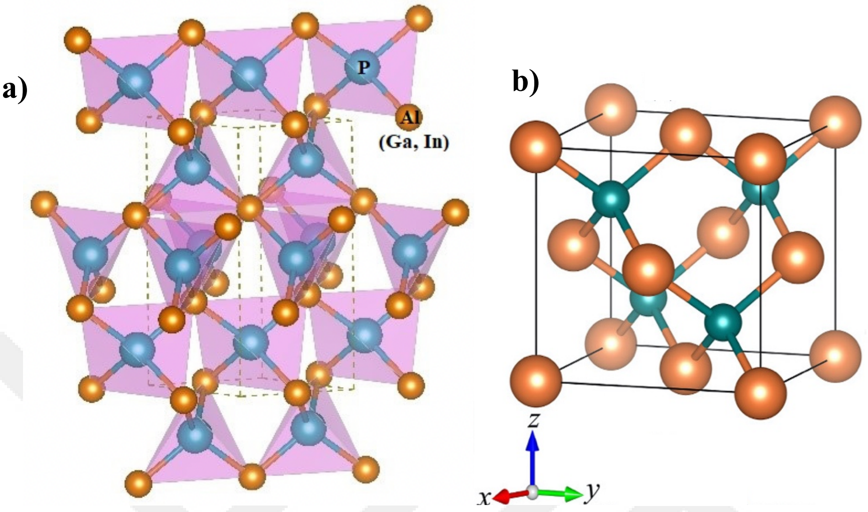

Figure 3. 12 a) Hexagonal structured (45) and **b)** cubic structured GaP (44).

Miamo et al. (45) used Heyd–Scuseria–Ernzerhof (HSE06) calculations to determine the electronic band structure of hexagonal GaP. Additionally, Gajaria et al.(46) calculated the electronic band structure of cubic GaP using first-principle electronic band structure calculations. Figure 3. 13 shows both the cubic and hexagonal GaP electronic band structures.

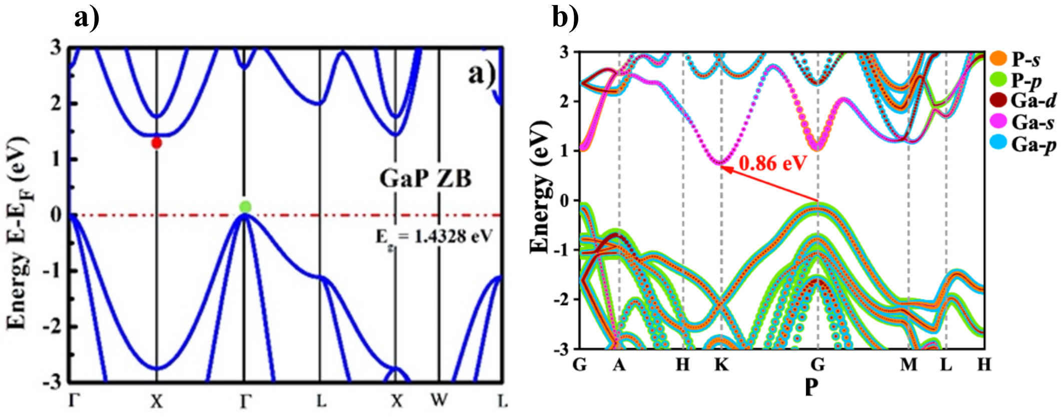

Figure 3. 13 Electronic band structure of **a)** cubic (46) and **b)** hexagonal GaP (45).

According to Miamo et al. (Figure 3. 13b), hexagonal GaP has an indirect band gap with a value of 0.86 eV, where the conduction band minimum (CBM) and valence band maximum (VBM) are located at the G (0.00, 0.00, 0.00) and K (0.33, 0.67, 0.00) points, respectively. Additionally, Gajaria et al. reported that cubic GaP has an indirect band gap with a value of 1.4328 eV. Comparing to the Materials Project calculations, the cubic structured GaP has an indirect band gap, while the hexagonal structure has a direct band gap.

In addition to analyzing the electronic band structure, Gajaria et al. (46) conducted computational calculations to assess the thermoelectric performance of both hexagonal and cubic structured GaP over a temperature range from 50K to 1200K, in comparison with other III-V semiconducting materials. As stated earlier, the thermoelectric performance of the materials strongly depends on carrier concentrations. Thus, Gajaria et al. first determined the highest power factor value as a function of carrier concentration at 10^{20} cm^{-3} and continued the thermoelectric performance calculations by fixing the carrier concentration at this level. For the Seebeck coefficient, it has an increasing trend with increasing temperature values. On the other hand, the electrical conductivity has an opposite trend with increasing temperature. The power factor shows different values for both the zincblende (zb) and wurtzite (wz) structures of GaP. The electronic thermal conductivity values are low under 200K but show an increasing trend as the temperature goes to 1200K. Observing from the graphs in Figure 3. 14 and Figure 3. 15 indicates that enhancing the power factor values along with electronic thermal conductivity will result in higher zT values for thermoelectric applications.

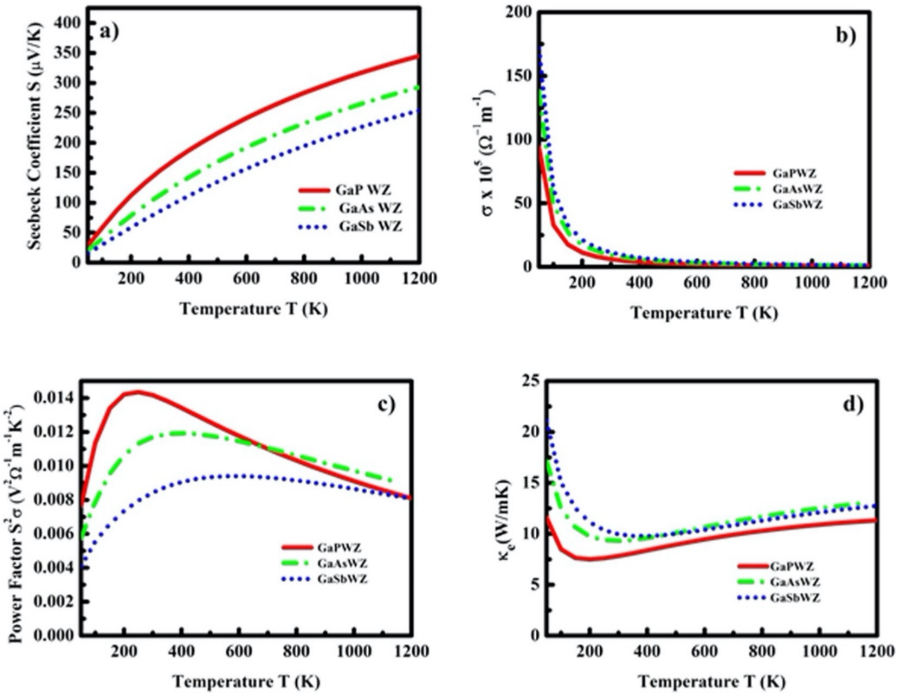

Figure 3. 14 Thermoelectric parameters: **a)** Seebeck co-efficient (S), **b)** electrical conductivity (σ), **c)** Power factor (S2σ) and **d)** electronic conductivity (κe) as a function of temperature for GaX compounds in WZ phase (46).

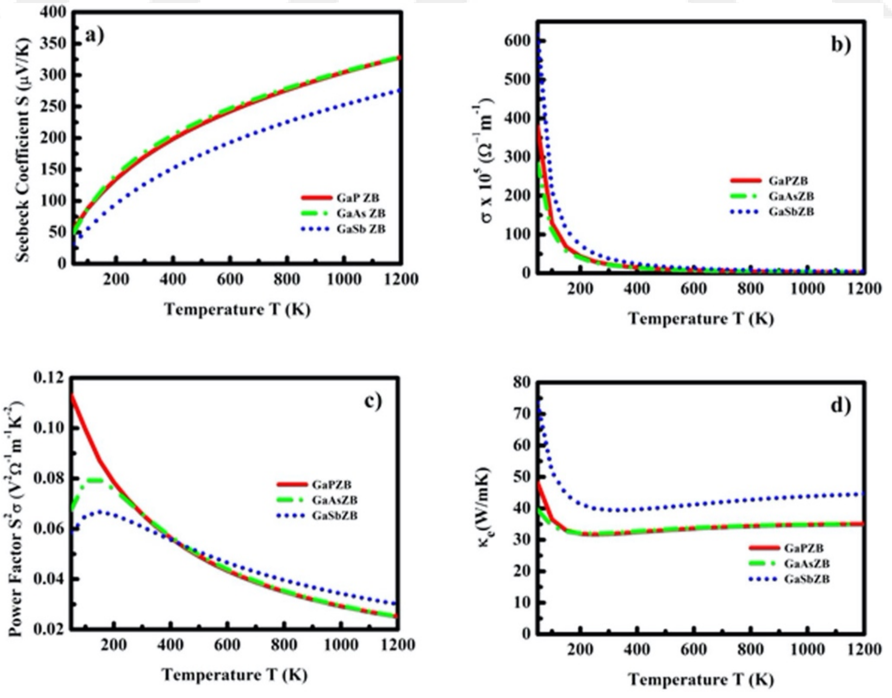

Figure 3. 15 Thermoelectric parameters: **a)** Seebeck co-efficient (S), **b)** electrical conductivity (σ), **c)** Power factor (S2σ) and **d)** electronic conductivity (κe) as a function of temperature for GaX compounds in ZB phase (46).

3.1.7 Research Summary

The aim of this thesis is to explore more about ternary thermoelectric phosphides, which have received less attention compared to other thermoelectric materials. With nano structuring, electronic band structure engineering, and improved experimental characteristics of electrical and heat transport properties, NaSnP and SrLiP with n-type or p-type ternary state-of-the-art thermoelectric compounds can be designed. Successful results in this project will pave the way for an all-phosphide thermoelectric generator with higher conversion efficiency than the current thermoelectric modules operating at mild temperatures.

The ternary phosphide family, specifically XYP compounds, can be good thermoelectric materials because of their excellent electrical and thermal properties. The high electrical conductivity of XYP composition, assigned with a parabolic band structure, also makes them have high n-type power factor values. Additionally, multiple band degeneracy in some compounds will result in a higher Seebeck coefficient. Similar to state-of-the-art materials, very low thermal conductivity values mean that the calculated zT value can reach up to 6.88.

3.2 Thermoelectric Zintl Phases

3.2.1 The History Behind the Zintl Phases

In the 1930s, Zintl phases were discovered by a German scientist named Edward Zintl, who conducted preparations and structural characterizations on numerous binary intermetallic compounds. These binary compounds are combinations of alkali metals from groups 1 and 2, and post-transition metals of the main group metalloids from groups 13, 14, 15, and 16 (47, 48). Zintl conducted X-ray diffraction measurements on these binary compounds and determined their crystal structure to have a salt-like nature. His primary aim was to form salt-like structures from heavier elements in groups 14 and 15. After Zintl's passing, another scientist named F. Laves referred to these binary compounds as salt-like structured Zintl phases. The first introduced Zintl compound is NaTl. In this compound, Na atoms act as donors to Tl, and this electronic transformation causes a polyanionic substructure formed by the larger Tl-ions. This electronic transfer concept is generalized with the NaTl compound under a concept called the Zintl-Klemm concept. This concept points out that the anions in the polyanionic substructure are the same as those of the neutral main group elements with the same number of valence electrons (49).

3.2.2 Introduction to Zintl Phases

The Zintl concept begins with the notion that certain intermetallic compounds can be studied as valence species. In an ideal scenario, these compounds achieve charge balance, where electropositive species can donate their excess electrons to more electronegative ones, creating bonds to satisfy valence requirements. Zintl phases constitute a class of polar intermetallic compounds categorized as polyanionic compounds, positioned electronically between the classes of intermetallic and insulating valence compounds. Moreover, these phases exhibit both ionic and covalent bonding, allowing for a wide variety of compositions, structures, and electronegativities. Semiconducting behavior is expected from Zintl compounds due to their filled valence states of anions or the polyanion arrays and the non-filled valence states of the electropositive electron donors (47, 50).

Zintl phases are classified as semiconducting compounds, and some compounds in this group have structures like a Zintl phase, but the electronic resistivity shows metallic behavior. These compounds are combinations of main group metalloids with alkali or alkali earth cations. These phases result from the reaction between the elements in groups 1 (alkali metals) and 2 (alkali-earth metals) and any post-transition metals or metalloids located in groups 13, 14, 15, or 16. Therefore, these binary compounds form a subgroup of intermetallic compounds. The electropositive elements from groups 1 and 2 act as electron donors to the electronegative elements in groups 13, 14, 15, or 16 to create a reasonable amount of bonding to fill each shell of the elements (47). According to Miller, Zintl phases are compounds where the bonding and non-bonding states are fully occupied and separated from the antibonding states by not more than 2 eV (51).

A scientist named Hume-Rothery found the valence electron count (VEC) rule, defined by the equation below (Equation 20). After the discovery of intermetallic Zintl compounds, the equation became unsuitable for these compounds. The Hume-Rothery rule predicted the optimal electron concentration as $3/2e^-$. However, the structure found by Zintl has $1\text{-}5/2e^-$ per atom (52).

$$VEC\ (X) = \frac{m.e(M) + x.e(X)}{x} \qquad \text{Equation 20}$$

After many approximations, the bonding in Zintl compounds has been treated in two different ways (47):

1. The valence electron count, VEC(X): The total number of all valence electrons in relation whit the number of anionic atoms.
2. The *8-N* rule: a covalent model with collective counting electrons. Generally used for binary compounds with a general formula expressed as M_mXx.

After all, the accepted definition of Zintl compounds is expressed by the second rule. The 8-N rule was proposed by scientists named E. Mosser and W.B. Pearson, which applies to binary compounds. Considering an element from the fourth to the seventh group of the periodic table, assumed to be named as X, the valence electrons of this atom can be demonstrated as e(X). This X atom needs to fill the valence band according to the octet rule; therefore, another more electropositive atom is needed. This more electropositive atom can be referred to as M. If there are covalent bonds existing between the M atoms, then not all valence electrons are turned to X. The particular reason for this circumstance is that the number of available valence electrons needs to be reduced by b[MM]. Also, when the X atom forms a covalent bond with each other, the required electron number to fill the valence state will be reduced and can be stated as b[XX]. This is actively demonstrated in a formula given in Equation 21, where the number of bonds between the X atoms is:

$$b(XX) = 8 - VEC(X) \qquad \text{Equation 21}$$

Therefore, the Zintl concept provides simple and effective bonding description that can be used in chemical applications to tune carrier concentration and mobility in semiconductors (50, 52).

To sum up some characteristics that has been stated so far of the Zintl phases are,

- Containing an alkali or alkali-earth metal or an element that can be metal, semimetal or small gap semiconductor.
- Structure need to be electronically balanced or closed shell compound.
- Showing semiconducting or poor conducting behavior.
- Because of the charge balances they show diamagnetic or very weak, temperature independent paramagnetic behavior.

3.2.3 Thermoelectric Zintl Phases

An ideal thermoelectric material should have a high Seebeck coefficient, metal-like electrical conductivity, and glass-like thermal conductivity values, which are outcomes of a phonon-glass electron-crystal structure. In Zintl compounds, anions provide the electron-crystal structure, and the cations provide phonon-glass characteristics. As previously stated, Zintl phases exhibit favorable characteristics for thermoelectric applications primarily due to their tunable transport properties, complex structures, and diminished thermal conductivities associated with a phonon-glass electron-crystal structure. Because of all these properties, Zintl phases have gained interest in the thermoelectric industry for commonly designing power generation owing to their electron-crystal, phonon-glass composition.

Progress was made in 2005 on $Yb_{1-x}Ca_xZn_2Sb_2$ which showed a reasonable amount of thermoelectric properties (53, 54). After a year or so, a p-type Zintl compound, $Yb_{14}AlSb_{11}$ was discovered with zT values near 1 at high temperatures without doping. However, if the structure is doped with Mn rather than Al, the zT value will show even higher values (19, 54, 55). After the discovery of the potential thermoelectric Zintl compound $Yb_{14}AlSb_{11}$, many other Zintl structures, such as complex structures, cage structures, layer structures, disordered, and defected structures, have been reported (53). Most of these discovered Zintl phases have promising zT values with p-type characteristics. The progress on thermoelectric Zintl phases are represented in Figure 3. 16.

Ortiz et al. developed a metric to quantify thermoelectric performance based on the thermoelectric quality factor (β), as mentioned in Chapter 2. He stated that even though most of the discovered Zintl phases have p-type properties, calculations based on β showed that n-type Zintl phases perform better compared to their p-type counterparts (53, 56). For instance, LiZnSb Zintl phases, one of the members of the 1-1-2 phase, show potential n-type thermoelectric material (57, 58).

Mg_3Sb_2 is a member of the 1-2-2 family discovered in 1933. Tamaki et al. recently synthesized this component with n-type behavior using excess Mg (26). Because of the unique conduction band complexity, with six conduction carrier pockets along the M-L line, Mg_3Sb_2 is an outstanding thermoelectric material. Band structure calculations show an indirect band gap of 0.6 eV with a valence band maximum located at the Γ point and a conduction band minimum at the K point in the Brillouin zone, generating a valley degeneracy of 2. This valley degeneracy leads to a higher thermoelectric quality factor found in good thermoelectric materials such as Bi_2Te_3 (59, 60). Tamaki et al. also synthesized the $Mg_{3.2}Sb_{1.5}Bi_{0.49}Te_{0.01}$ composition with a zT value of 1.5 at 715 K. This determination leads to the conclusion that excess Mg is the main reason for the material to be n-type and responsible for the n-type charge carriers (60).

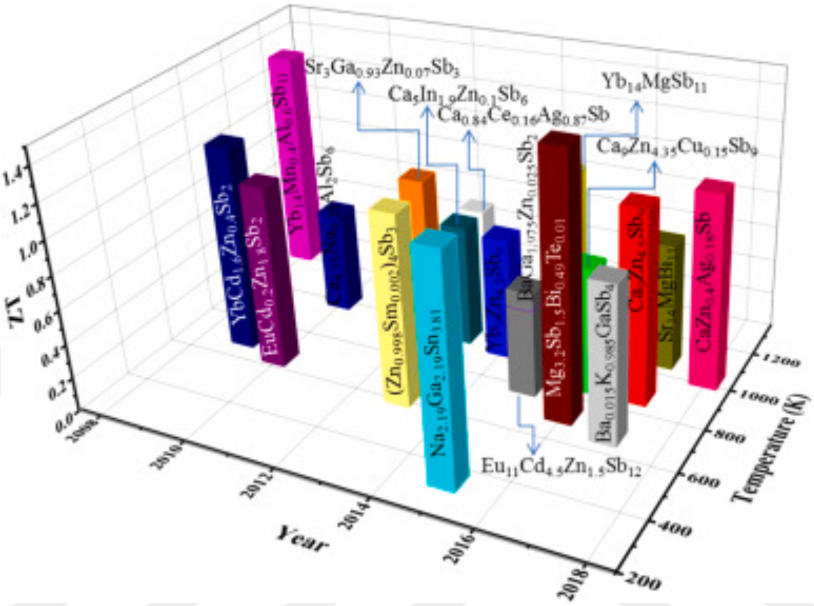

Figure 3. 16 Recent progresses of thermoelectric materials of Zintl phases of the years (54).

3.2.3.1 Mg_3Sb_2 Zintl Phase As A Promising Thermoelectric Material

The conventional thermoelectric materials, mainly PbTe and Bi_2Te_3, have made considerable advancements in utilizing the thermal and electronic strategies of Thermoelectrics. However, the toxicity and high-cost properties of these elements have limiting effects on the large-scale production of these promising thermoelectric materials (61).

Mg-Sb alloys were discovered and demonstrated a very similar structure to Pb-Te alloys but with smaller mass density and lower vapor pressure values (62). Mg_3Sb_2 compounds are classified under Zintl components, crystallized in a $CaAl_2Si_2$-type structure (*P-3m1*) (61, 62). The crystallographic structure of Mg_3Sb_2 consists of two different Mg sites. One is octahedrally coordinated by the Sb atoms, and the other is tetrahedrally coordinated with the Sb atom(63). These magnesium atoms are electropositive Mg^{+2} cations and negatively charged $[(Mg_2Sb_2)^{-2}]$

polyanions, with Mg^{+2}acting as a valence electron donor to the $[(Mg_2Sb_2)^{-2}]$ charged polyanions because of the electronegativity difference.

As seen in Figure 3. 17, the $[(Mg_2Sb_2)^{-2}]$ charged polyanions form a covalently bonded layered framework along the ab-plane with Mg^{+2} cations placed between and ionically bonded with the layered polyanion framework. While the Mg^{+2} cations provide good tunability and low thermal conductivity, $[(Mg_2Sb_2)^{-2}]$ charged polyanions create a complex structure with high hole mobility (64, 65).

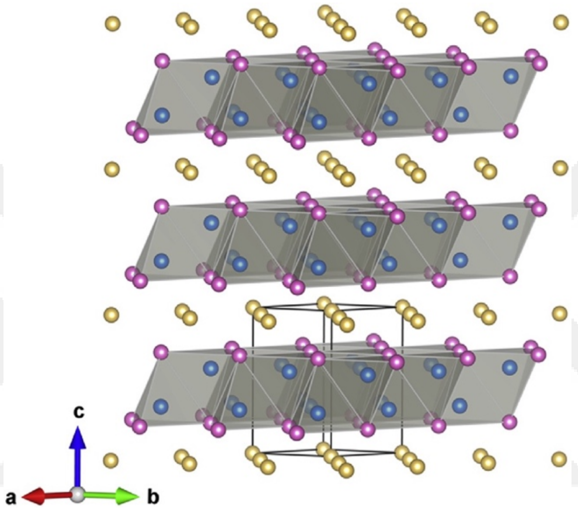

Figure 3. 17 Crystal structure of Mg_3Sb_2 and its derivatives (AB_2C_2) with a structural prototype CaL_2Si_2 (53)

The performance and high *zT* values of an n-type Mg_3Sb_2 are related to the large effective mass, high carrier mobility, relatively high conduction band degeneracy, and low lattice thermal conductivity. The effective mass and band degeneracy factors are used to determine the electronic transport properties, and these properties can be calculated through density functional theory calculations. In the Mg_3Sb_2 structure, the valence band maximum is located at the Brillouin zone center, seen from Figure 3. 18, and the p-orbitals of the Sb atoms and octahedrally bonded Mg atoms are related to this. However, the tetrahedrally bonded Mg atoms are related to the bottom of the conduction band. The p-states of the Mg and the Sb create a hybridized density of states that defines a covalently bonded Mg-Sb, which is favorable for the electronic transport properties (59, 61, 63, 66).

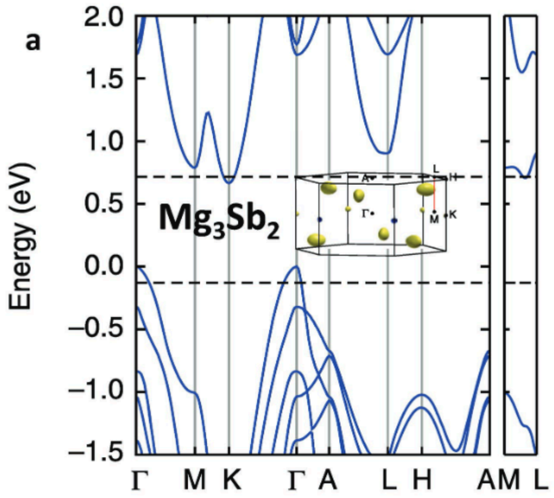

Figure 3. 18 The band structure and the electron Fermi surface for Mg_3Sb_2(61)

Mg_3Sb_2 Zintl components have generally p-type electronic transport characteristic because the valence band maximum is located at the high-symmetry \Gamma-point with low valence band degeneracy. Also, the p-type Mg_3Sb_2 phases have low power factor compered to its n-type counterparts (61, 63, 67, 68). To increase the valence band degeneracy, energy values of the nondegenerate band $\Gamma(p_z)$ and doubly degenerate band $\Gamma\left(p_{x,y}\right)$ re-organized which stated the first and the second valence band maximum (69). With the determination of Density Functional Theory (DFT) calculations n-type Mg_3Sb_2 have maximum valence band at Γ point and minimum conduction bant at the K point resulting 6 valley degeneracy while p-type Mg_3Sb_2 have only one valence degeneracy value at Γ point. This difference resulted the n-type material have higher carrier mobility compared to p-type materials. (70). These valley degeneracy values also observed with Fermi surface. In n-type structure 0.03eV valued energy level is located at the M-L line with Valley degeneracy of 6 (59, 71). However, for the p-type structure only have one. The Fermi surface can be seen for both structures in Figure 3. 19 (15, 25).

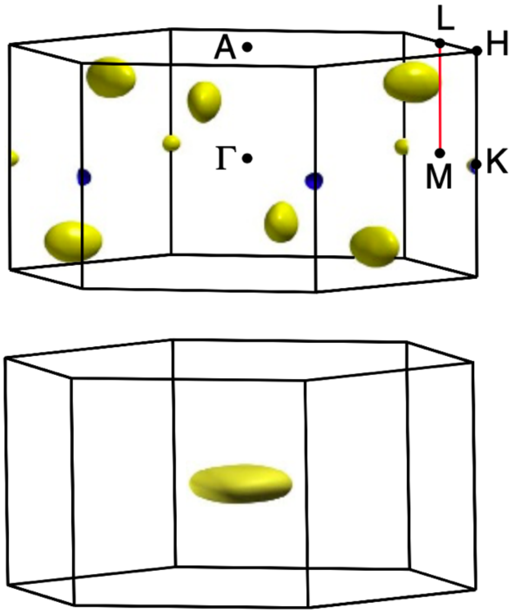

Figure 3. 19 Calculated Fermi surfaces n-type and p-type Mg_3Sb_2 at the Fermi level 0.03eV above conduction band minimum and 0.1eV below conduction band minimum respectively (59).

3.2.3.2 Improving the Thermoelectric properties of Mg_3Sb_2 Zintl compound

An ideal thermoelectric material requires good electronic properties and also a fairly low thermal conductivity. Recently, a few strategies have been employed to optimize the thermoelectric performance of Mg_3Sb_2 Zintl compounds. These strategies include doping, orbital engineering, carrier concentration tuning, grain boundary engineering, nano structuring, and others. (54, 72).

The electronic transport properties of Zintl phases are directly affected by their electronic band structure and carrier concentrations. Mg_3Sb_2 is mostly predisposed to p-type conduction due to Mg vacancies, resulting in low carrier mobility and relatively stronger bond polarity. However, it can exhibit intrinsic or, in fact, n-type conduction (54). The first successful synthesis of an n-type $Mg_3Sb_{1.5}Bi_{0.5}$ component was performed by Tamaki et al (26). Tamaki used an excess amount of Mg to create Mg vacancies. Ohno et al. explained the theory to create n-type $Mg_{3.2}Sb_{1.5}Bi_{0.49}Te_{0.01}$ using a phase boundary mapping technique.

P-type conduction is based on the Mg vacancies, which accept low-energy electrons and produce extra holes. As seen in Figure 3. 20 a, a Mg excess region will create higher Mg vacancies compared to the Sb excess region. Additionally, Figure 3. 20 b represents the Mg_3Sb_2 compound behaving as a line compound, similar to other Zintl semiconductors. This can be understood from the very narrow single-phase Mg_3Sb_2 region. To achieve a positive formation energy of vacancies at the edge of the conduction band, the synthesis of Mg_3Sb_2 at the Mg excess side enables the composition to have n-type conduction (60).

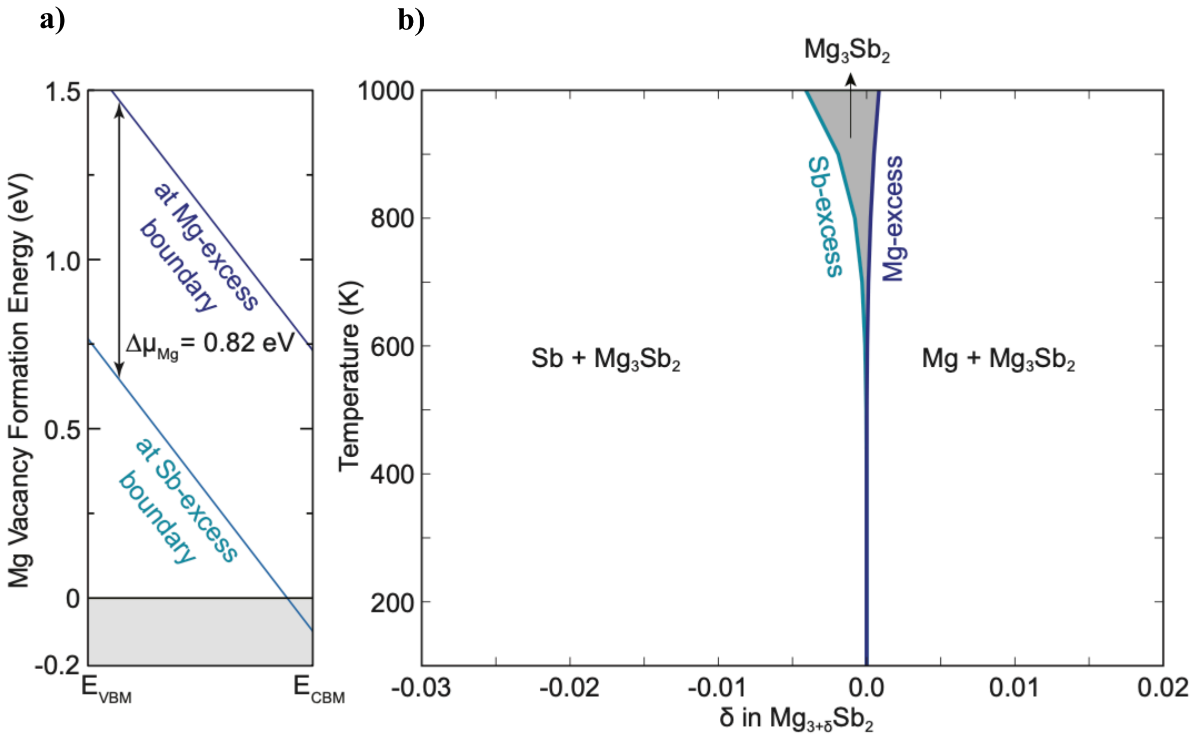

Figure 3. 20 a) The Mg vacancy formation energy in Mg_3Sb_2 as a function of Fermi level (Ef) showing that when Mg excess Mg_3Sb_2 region having higher vacancy formation energy. **b)** Calculated Mg-Sb phase diagram near Mg_3Sb_2 with the solubility limits (60).

Scattering mechanisms can be optimized to improve the electrical transport properties of Mg_3Sb_2-based Zintl compounds. Tuning the carrier scattering mechanism has a range of states, mainly focusing on either ionized impurity scattering or acoustic phonon scattering (73, 74). The Mg vacancies in the Mg_3Sb_2 structure will be able to change the Hall carrier concentrations between the heating and cooling steps through the ionization and deionization of these vacancies.

To optimize the electrical transport properties of Mg_3Sb_2 Zintl compounds, tuning the carrier concentration values between 10^{19} to $10^{20}cm^{-3}$ can be used. In Mg_3Sb_2 components, controlling the carriers can be achieved by incorporating group 3 elements (e.g., Sc, Y, and La) substituting on the Mg site, and group 16 elements (e.g., S, Se, or Te) on the Sb site act as extrinsic dopants (70). Additionally, Gorai et al. conducted calculations on the solubility limits, interstitial defects, defect formation energies, and phase stability limits, which help determine proper n-type or p-type doping elements (75). With the same purpose, several studies have been conducted to increase the zT value of the p-type Mg_3Sb_2 with alkali elements (Li, Na) and Ag doped on the Mg site, Pb element on the Sb site to increase the carrier concentration(76-78). Overall, the first doping element, Te, still has the highest effect on tuning the carrier concentration of the Mg_3Sb_2 components (70).

Orbital engineering is another promising strategy to optimize the electrical properties of Zintl compounds, confirmed with calculations and experimental results. As mentioned before, the valence band edge of Mg_3Sb_2 is located at the Brillouin zone center at the Γ point. Zhang et al. (69) reported that because of crystal splitting energy, the pz orbital splits from the px and py orbitals in layered materials. This splitting can be seen in Figure 3. 21 a. The splitting energy results in a separation in the valence band at the Γ point, represented by a doubly degenerate band Γ(Px,y) and a nondegenerate band Γ(pz) structures. The crystal splitting energy describes the difference between these band structures and can be represented by Equation 22 below.

$$\Delta = E(\Gamma(pxy)) - E(\Gamma(\mathrm{pz})) \qquad \text{Equation 22}$$

By changing the bond length and the angle, the lattice structure parameters, as well as doping, alloying, and composing solid solutions, can reduce the orbital splitting energy (34). Obtaining a near-zero crystal splitting energy value will allow for good electrical transport performance, thus with a high power factor (69, 79). In Figure 3. 21 b and c, two different band engineering results are given. In Figure 3. 21 b, Zhang et al. reported a Mg_3Sb_2-based Zintl structure (80) with Bi alloying on the Sb side having an effect on the conduction band edge, resulting in a more dispersed conduction band along the $\Gamma - \mathrm{A}$ direction, which led to a reduction in the band gap. After introducing Ag on the Mg side, the electronegativity difference between Ag and Sb/Bi will refer to a smaller effective mass, increasing the covalency of the chemical bonding, thus resulting in a decrease in the band gap. In Figure 3. 21 c, Imasato et al. (81) reduced the internal effective mass of the Mg_3Sb_2 structure by alloying with Mg_3Bi_2. The alloying changes the dominant band structure and the effective valley degeneracy, thus reducing a narrowed band gap.

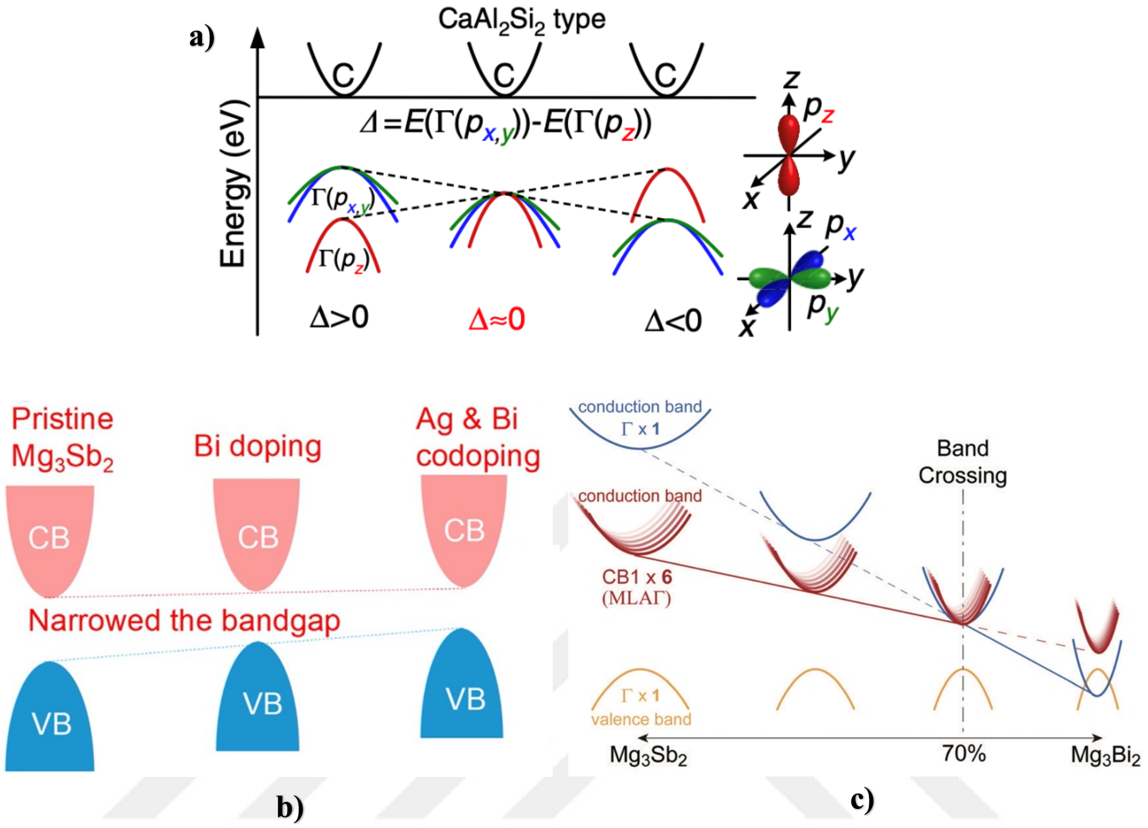

Figure 3. 21 a) Illustration of the nondegenerate and doubly degenerate band structures from the $CaAl_2Si_2$ structure at the Γ point (61, 69). **b)** Systematic diagram of narrowed band gap Mg_3Sb_2 structure after Ag and Bi doped (80). **c)** Systematic view of the band engineering effects when doping Mg_3Bi_2 to Mg_3Sb_2 structure (81) .

3.2.4 Summary of the Research

Finding highly efficient n-type Zintl compounds has seen an increasing demand in the thermoelectric field due to their environmental friendliness, and predictions suggest that they have better performance compared to their p-type counterparts (82, 83). The discovery of new n-type Zintl phases with higher zT values compared to their p-type counterparts will have a positive effect on building full Zintl thermoelectric generators. Recently, 1-2-2 compounds ($CaAl_2Si_2$ structure) have shown promising results in producing n-type Zintl compounds. Tamaki et al. produced a promising n-type Mg_3Sb_2 structure by doping with Bi and Te (26). The main motivation in this thesis is to change the electronic conduction of p-type $CaMg_2Sb_2$ and $CaMg_2Bi_2$ structures to n-type conduction using doping strategies.

Chapter 4:

EXPERIMENTAL AND CHARACTERIZATION METHODS

The compositions in this study were synthesized using the mechanical alloying technique and solid-state synthesis. The materials used in this study are known to be air-sensitive; therefore, to eliminate any surface oxidation, weighing, and raw material preparation steps were conducted in a glovebox (MBraun) under an inert argon atmosphere with a level of oxygen lower than 0.1 ppm. To achieve homogeneity, reduce particle size, and synthesize the desired product, the initial elements were introduced into a high-energy ball mill, specifically the SPEX800D. After obtaining the fine powder of the desired compositions, a spark plasma sintering instrument was used for the consolidation operation. After completing the synthesis route, chemical and thermoelectric characterizations were implemented using the techniques discussed below.

4.1 Materials

The starting chemicals used in this experiment and their properties are given in Table 1. The elements that are part of the composition are directly placed in a high-energy ball mill, a clean alumina crucible, or a clean quartz tube without any primary purification.

Table 1. Starting Chemicals.

Chemicals	**Formula**	**Physical State**	**Melting Point**	**Purity**	**Company**
Antimony	Sb	Shot	630℃	99,999%	Sigma Aldrich
Bismut	Bi	Shot	271℃	99,999%	Alfa Aeser
Calcium	Ca	Pieces	842℃	99,999%	Sigma Aldrich
Lantanum	La	Pieces	920℃	99,9%	Sigma Aldrich
Magnesium	Mg	Powder	650℃	99,8%	Pavezyum
Tellurium	Te	Shot	449,51℃	99,9999%	Alfa Aeser
Red Phosphorus	P	Powder	590℃	98,00%	Alfa Aeser
Sodium	Na	Rod	97,8℃	99,99%	Sigma Aldrich

Tin	Sn	Shot	231,9°C	99,9999%	Sigma Aldrich
Stronsium	Sr	Dendritic pieces	777°C	99,99%	Sigma Aldrich
Gallium	Ga	Shot	29,76°C	99,99%	Sigma Aldrich

4.2 Sample Preparation Methods

4.2.1 Solid-State Synthesis

To determine the synthesis route of the ternary phase phosphides, solid-state synthesis is applied. The first step of this process starts with cleaning the aluminum crucibles in the oven for one day. Afterward, all the preparation steps are carried out under an argon atmosphere. The proper stoichiometric ratios of Na pieces, Sn shots, and P powder are placed inside the alumina crucible. The prepared aluminum crucible is then placed carefully inside a quartz tube on top of a glass hole. Afterwards, the quartz tube is closed and placed into a vacuum oven with an argon gas flow. The tube is first heated to 280 ºC in 30 minutes and held for 2 hours. Then, the tube is heated to 500 ºC in 3 hours and held for 48 hours. When the heating is done, the tube is cooled down in 12 hours. However, the synthesis is unsuccessful.

The same process is applied without the alumina crucible. The same elements are placed with the correct stoichiometric ratios inside a quartz tube under an argon atmosphere. Then, the loaded quartz tube remains in a vacuum until the vacuum level reaches 10^{-2} Torr to prevent any oxidation, and after the quartz tube is sealed under vacuum. The sealed tube is placed vertically with the help of an aluminum crucible inside the oven with the same temperature program that was applied previously. Unfortunately, this process also results in failure.

4.2.2 Mechanical Alloying

To reduce the particle size of the starting elements and produce homogeneous components, a high-energy ball milling device (SPEX 800D) was selected for use. Two identical vials are placed between the clamps of the high-energy ball mill. Depending on the synthesis route, the vials included stainless steel balls with variable sizes. Regarding the working principle, the speed of the vials reached up to 825 cycles per minute with a back-andforth shaking motion, including short-range lateral movement and G-forces. Throughout the synthesis, the starting elements reacted with each other to become a homogeneous powder, and mechanical alloying took place. The schematic view of the SPEX800D is given in Figure 4. 1 and Figure 4. 2

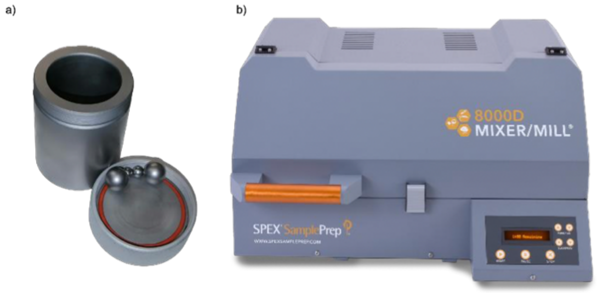

Figure 4. 1 a) Stainless still vial with stainless still balls and **b)** high energy ball milling device.

Figure 4. 2 Schematic view of the high energy ball milling process.

In this study, ternary and binary phase phosphides (NaSnP, SrLiP, and GaP), 1-2-2 Zintl compounds ($CaMg_2Sb_2$ and $CaMg_2Bi_2$) are synthesized using high-energy ball milling. Desired amounts of the starting elements (antimony shots, bismuth shots, calcium pieces, lanthanum piece, magnesium powder, tellurium shot, tin shots, powdered phosphorus, sodium pieces, and strontium pieces) were weighed and placed inside the high-energy ball mill vial with four-quarter inch and two half-inch stainless steel balls, depending on the composition. To eliminate any oxidation, weighing and sealing were done in an argon-filled glove box. The mechanical alloying process was applied for 2 hours for the phosphorus compounds and between 90 to 120 minutes, depending on the composition, for the Zintl phases. Within a 30-minute time range, the vial was placed in the glove box, and the powder that stuck to the sides of the vial was rubbed off to obtain homogeneous samples. At the end of the mechanical alloying process, the vial was placed back inside the glove box and taken out for characterization and SPS steps.

4.2.3 Spark Plasma Sintering

The Spark Plasma Sintering (SPS) application was implemented after the mechanical alloying process to increase the density of the obtained fine powder. In this study, the SPS machine (AGUS-PECS SPS-320Sx) is provided by SUGA Co. Ltd. The SPS technology, as shown in Figure 4. 3, is an improved version of the conventional hot-pressing method. By raising the temperature values to create Joule heating, a pulsed DC electric current is directly applied through the sample or the mold (graphite die) that includes the sample. The process stands out by rapidly increasing the temperature within a very short time (in seconds) and applying ultra-high pressure to create a spark plasma effect. (84)

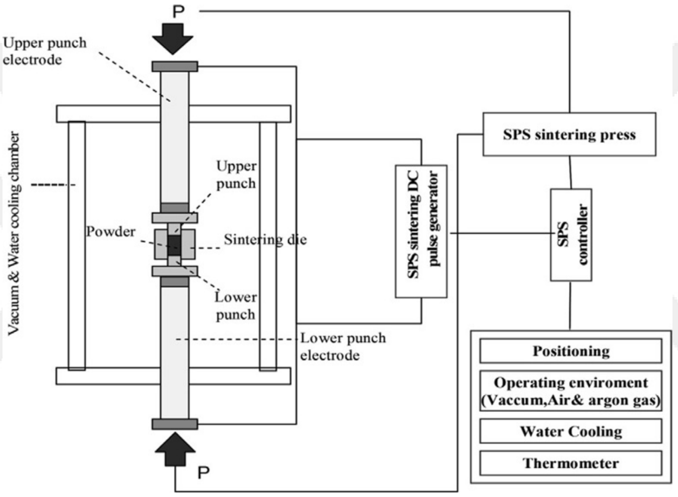

Figure 4. 3 Basic SPS configuration (84).

The system consists of a hydraulic sintering press machine, punch electrodes combined with a water cooler, a vacuum chamber, a vacuum air/argon atmosphere controller, a DC pulse sintering power generator, a Z-axis, and a temperature-measuring control unit. The powder sample is placed in a mold without any preliminary application. A high-intensity/low-voltage electrical current is directly passed through the powder inside the mold. The hydraulic system applies pressure in the direction of the Z-axis. The punches also act as electrodes that conduct the electrical current. The hydraulic pistons are water-cooled to prevent overheating. The DC pulse generator controls the pressure amount during the sintering process to prevent excess pressure. A thermocouple is used as a temperature-controlling agent, depending on the maximum temperature required for the sintering process. The thermocouple is placed in the middle of the mold inside a small hole. (84) (85).

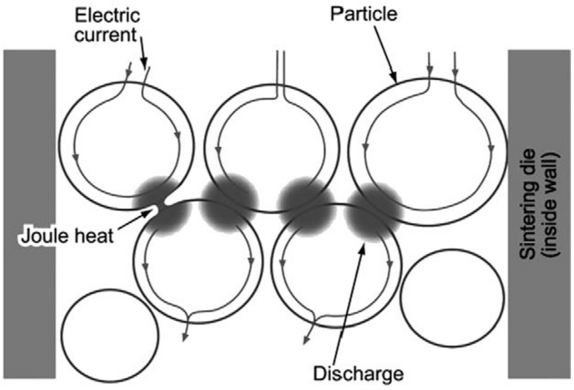

Figure 4. 4 Pulsed current flow through powder particles (84).

In theory, the pressure is applied at the beginning of the process and remains constant during sintering. Between the contact points of the particles, a spark discharge appears due to the motion of electrons. Because of the electron motion, a temperature gradient of several thousand degrees Celsius causes a local high-temperature state, leading to evaporation and melting on the surface of the powder sample during the sintering process. The term 'necks' is formed around the area of contact points between the particles at this stage, as seen in Figure 4. 4. The heat provided by the applied DC current causes a Joule heating effect, occurring at the center of the spark discharge column, and diffusing to the surface of the sphere. After the intergranular bonding portion quickly cools and forms a plastic deformation, the densification of the materials proceeds further. Figure 4. 5 demonstrates the neck formation in the spark plasma sintering process (84, 86).

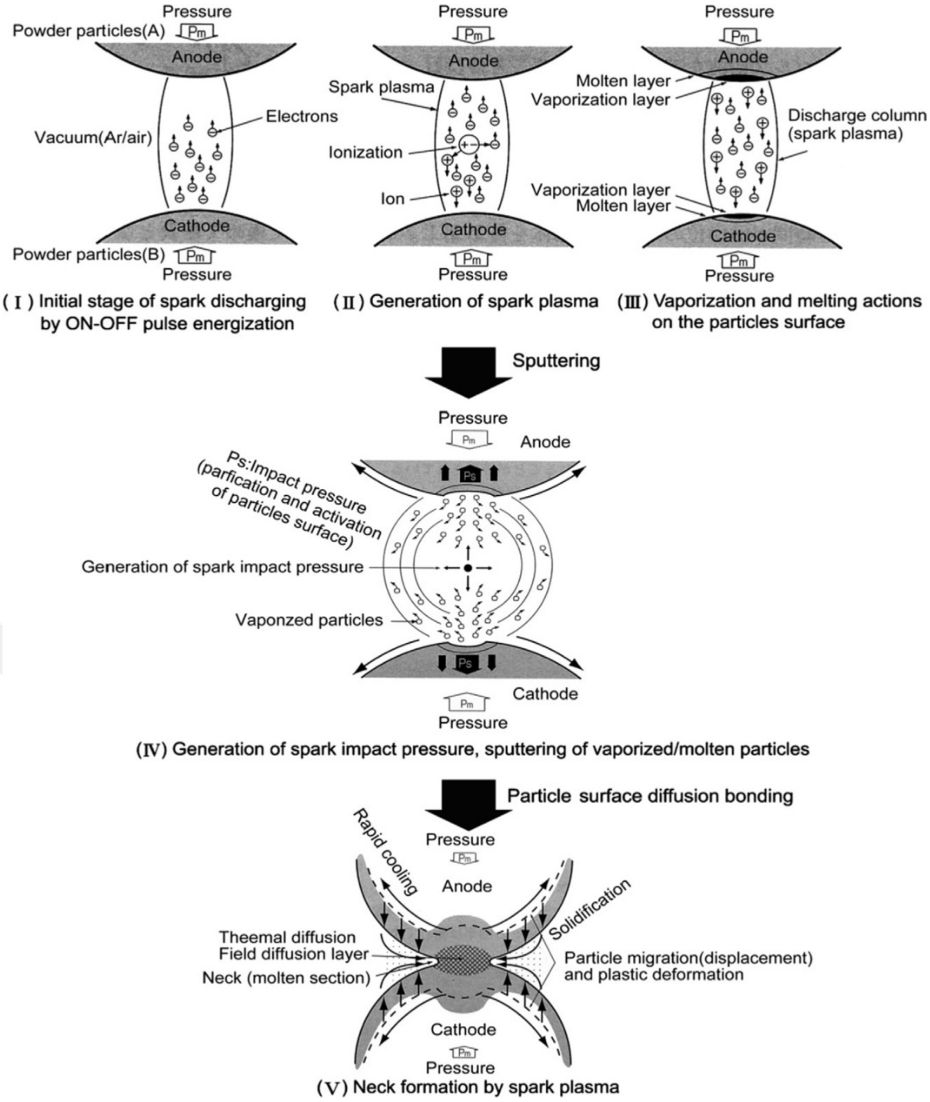

Figure 4. 5 Basic mechanism of neck formation by spark plasma sintering (84).

The powders are placed in a graphite die with a 10 mm inner diameter. To increase conductivity and facilitate the removal of consolidated samples, graphite foils are placed inside the graphite die and at the ends of the punches. After placing the powder samples, cold pressing is applied. All preparation steps are done under an argon-filled glove box to prevent any oxidation. The sintering process is carried out under vacuum with a 50 MPa pressure at 600ºC for 10 minutes. After the pressure is released, the vacuum chamber is allowed to cool until room temperature is reached. To prevent the evaporation of excess Mg content, Spark Plasma Sintering (SPS) is performed up to 550ºC.

4.2.4 Dimond Wire Saw Cutting

Determining the thermal diffusivity, thermal conductivity, electrical conductivity, and Seebeck coefficient requires size reduction. Horizontal and vertical cuts on the densified samples are made using a diamond wire saw cutter. LFA measurements require cylindrical samples with a thickness of 1.5 mm to 2 mm to obtain accurate values. To achieve the required size, samples are polished and placed on top of a sample holder in a horizontal direction. After the LFA piece is cut correctly, the remaining dense sample is placed vertically. The sample is then measured, and a bar-shaped sample with dimensions of 3x3x6 mm is cut for ZEM-3 measurement. In all cutting processes, water is used as a coolant, and a lubricant is added to the water to prevent oxidation or corrosion and to improve cutting performance. Properly cut samples are sanded with SiC paper to obtain a regular, smooth shape for the upcoming measurements. The Figure 4. 6 a represented the the Dimond wire Saw and Figure 4. 6 b and c represented the cutting process.

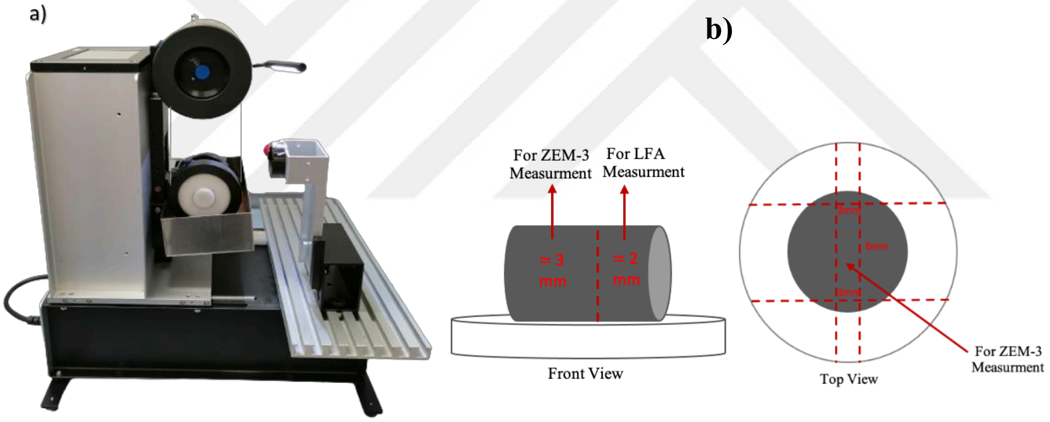

Figure 4. 6 a) Diamond Wire Saw instrument and **b)** placement of samples to the holder and their cutting directions.

4.3 Material Characterization Techniques

4.3.1 X-Ray Diffraction Technique

X-ray diffraction, or XRD, is one of the most developed and widely used material characterization techniques. This method requires relatively simple equipment and offers the advantage of being nondestructive. The samples used for XRD measurements require minimal or no primary preparation. XRD is primarily employed for crystalline samples, but some information can be obtained from amorphous samples as well. XRD measurements can provide useful information about crystal geometry, compositional details, and the arrangements of atoms. The technique can also offer quantitative information, such as estimating the amount of different phases present within the sample.

The XRD equipment used in this study (Rigaku Miniflex XRD) employed Cu Kα (λ=1.540598 Å) radiation, a 40 kV voltage, and a 20-mA current to characterize both powder and bulk samples.

When an X-ray beam is directed towards a material volume, it undergoes various interactions resulting in different absorption and scattering effects. One such interaction is known as Rayleigh scattering, involving the elastic and coherent scattering of photons by the electrons in the material's atomic nuclei. The atoms in crystalline materials are arranged in a regular and periodic manner. As a result, when the X-ray interacts with the crystal lattice, the scattered radiation experiences constructive and destructive interference. This phenomenon helps determine and understand the characteristic diffraction pattern used to investigate the crystalline structure of the material. The principle of the method involves analyzing the angles and intensities of the diffracted X-rays, using Bragg’s Law (87, 88). The Bragg’s Law given in the Equation 23 below.

$$2dsin\theta = n\lambda \qquad \text{Equation 23}$$

In order, λ is the wavelength of the incident beam in nm, d is the lattice spacing in nm, and θ is the angle of the diffracted X-ray beam in degrees. Each diffraction pattern is inherently unique. Comparing the diffraction pattern of the synthesized material with those stored in the database helps to identify and determine unknown materials based on their diffraction signals.

4.3.2 Scanning Electron Microscopy

Scanning electron microscopy, or SEM, is a powerful imaging technique used to observe the surface morphology and topology of materials at high magnification. The principle of the method involves focusing an electron beam onto the sample surface and interacting it with the atoms to generate detailed images with exceptional resolution.

The fundamental parts of the SEM include the optical column, which comprises the electron gun system, lens system (condenser and objective), and a detector with a vacuum system. The electron gun emits electrons with a constant beam and increases the speed of the electrons through the sample. The sample is placed on a sample holder located near the lower part of the column. As electrons accelerate, they pass through a series of lenses, including condenser lenses and an objective lens. These lenses help focus the electron beams on the top of the sample to create excitation on the sample surface. Vacuum pumps are used to eliminate the effects of air molecules. The detector system is used to determine the energy of electrons coming from the material surface. Depending on the interaction between the sample and the electron beam, various signals can be emitted from the surface, such as secondary electrons, backscattered electrons, Auger electrons, and X-ray electrons (89, 90).

Secondary electrons are commonly used signals with low energies around 3-5 eV. They provide information about the topology and visualize the surface texture or roughness. Secondary electrons can resolve surface structure down to the order of 10 nm because they can only escape from the specimen's surface. They are generated when the primary electron beam dislodges a loosely bonded electron from the material's surface and can only be detected when they are dislodged near the reaction vessel due to their low energy values. The secondary electrons give a very similar image to that of the specimen's surface when illuminated with light. Detectable secondary electrons appear brighter, while the undetectable ones appear darker, creating a shadow-like appearance.

Backscattered electrons are the second most used signals that provide information about both the topology and the composition of the material. These incident electrons can approach the nucleus of an atom sufficiently close to be scattered with large angles due to elastic scattering and re-emerge from the surface with energy greater than 50 eV. Around 10-50% of the incident beam emitted from the electron gun is detected as backscattered electrons, and around 60-80% of this value maintain their initial energy. The atomic number (Z) also has an effect on the amount of backscattered electrons. Elements with higher atomic numbers have higher positive charges on the nucleus; due to this, the number of backscattered electrons follows a linear increment (91, 92).

In this study, SEM measurements were performed using the Zeiss Ultra Plus Field Emission Scanning Electron Microscope located in KUYTAM laboratories. Before the analysis, bulk samples were prepared in the metallography laboratory by embedding them in a Bakelite sample holder and placing them in a polishing device. The samples were then polished with different-sized (800, 1200, 1500) grinding papers with the addition of Diamond solution to achieve a smoother and brighter sample surface. After the preparation, the samples were placed on a carbon tape, and the measurements were successfully achieved.

4.3.3 Transmission Electron Microscopy

TEM stands for Transmission Electron Microscopy, which is a high-resolution microscopy technique that utilizes high-energy monochromatic electron beams (typically ranging from 100 to 300 kilowatts) with a resolution of 10 nm. It gathers valuable information about the chemical composition, crystal structure, and enhanced morphological and structural details of specimens.

TEM shares similar features with SEM in terms of the arrangement of the electron gun, condenser lenses, and detectors. However, the outstanding distinction lies in sample preparation and data collection methods. In TEM, images are formed by transmitting high-energy electrons through very thin samples. For electrons to pass through the samples, the thickness should be around 100 nm.

The basic components of a TEM include the electron source, sample illumination part, imaging lenses, magnification part, and detectors. The electron gun generates electron beams, and electromagnetic lenses, located on the column, focus the generated electron beams on the sample. Some electrons are transmitted through the thin sample, while others are diffracted. Afterwards, the transmitted electrons are refocused and magnified by an electromagnetic lens system to project the image onto a screen. Depending on the transmitted and diffracted electrons, bright (only transmitted) and dark (only diffracted) field images can be observed.

In this thesis, the Hitachi Field Emission Transmission Electron Microscope (HF5000) located in KUYTAM was used to determine the orientation of the grains, crystal configuration, and identify dislocations (89, 93, 94).

4.4 Physical Property Measurements

4.4.1 Thermal Diffusivity and Thermal Conductivity

The laser flash method is used to determine the thermal diffusivity values of the synthesized samples. In this thesis, the NETZSCH LFA 467 HT Hyper Flash device in Figure 4. 7 a is utilized to determine diffusivity values. Thermal diffusivity is the rate of transferred heat through the material's hot end to the cold end and is also calculated by dividing thermal conductivity by density and specific heat capacity at constant pressure. The LFA measurement is conducted in a vertical setup, as seen in Figure 4. 7 b, where a light source at the bottom of the tube heats the horizontally placed samples. The samples are heated from the bottom through the top, and a detector located on top of the system determines the time-dependent temperature rise. When the signals form a straight line, the thermal diffusivity values are known to be higher. Thermal diffusivity can be expressed by Equation 24, where the material thickness (d) and half maximum time $t_{1/2}$ determine the diffusivity values.

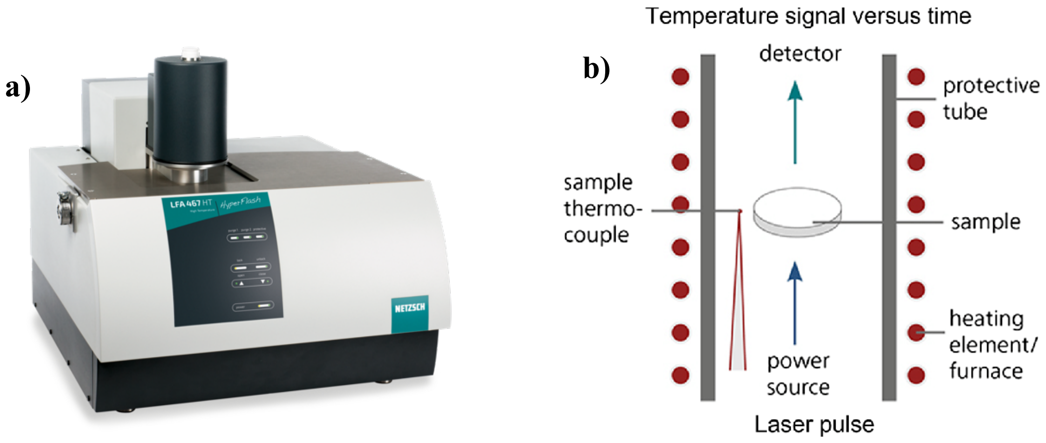

Figure 4. 7 Illustration of the laser flash analyzing **a)** device and **b)** laser flash analyzing method.

$$\alpha = 0.1388.\frac{d^2}{t_{1/2}} \quad \text{Equation 24}$$

Thermal diffusivity measurements are performed under argon atmosphere, starting from 50ºC and reaching a maximum of 400ºC for 10mm diameter pellet samples. To determine the thermal conductivity at specified temperature values, the obtained thermal diffusivity values can be used with the following Equation 25.

$$\kappa(T) = d(T).C_p(T).\alpha(T) \qquad \text{Equation 25}$$

Here, κ is the thermal conductivity (W/K·m), d is the density (g/cm³), C_p is the specific heat (J/g·K), and α is the thermal diffusivity (mm²/s) respectively. All the measurements were conducted by placing the pellet sample inside 12.7mm diameter-sized holders, and the determination of the sample density was done using the Archimedes method with ethyl alcohol at room temperature.

4.4.2 Electrical Conductivity and Seebeck Coefficient

The electrical conductivity and Seebeck coefficient measurements are performed using the ULVAC ZEM-3 Seebeck Coefficient / Electrical Resistance Measurement System, as shown in Figure 4. 8.

Figure 4. 8 Electrical resistivity and Seebeck coefficient measurement system.

In the analysis, a rectangular-shaped block sample is placed vertically between the upper and bottom block-shaped electrodes. The sample is heated to a specified temperature and held in place while the bottom block electrode heats the sample by 10, 20, and 30 K to create a heat gradient effect. Seebeck coefficient measurements are performed by measuring the temperature values of the two electrodes pressing against the side wall of the sample. The same side electrodes are also used to measure the dE, Thermal electromotive force, values. To measure the electrical resistance, the DC four-terminal method is used. The principle of the method involves applying a constant current (I) to both ends of the sample to measure and determine the voltage drop (dV) between the same wires of the thermocouple by subtracting the thermo electromotive force between leads (95). The Figure 4. 9 represented the measurement procedure.

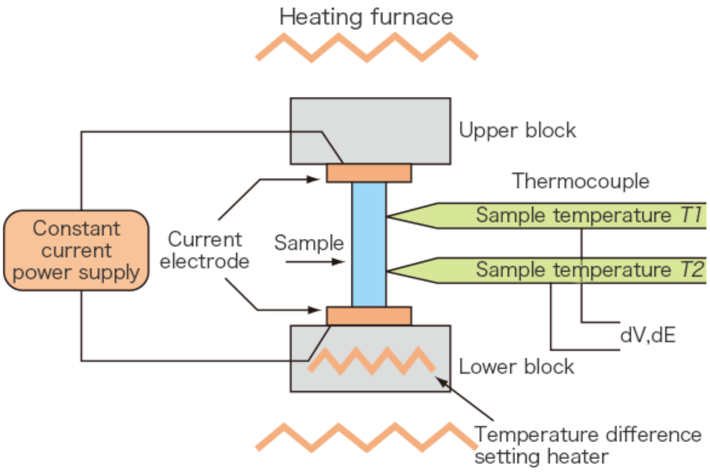

Figure 4. 9 Schematic view of the electrical resistivity and Seebeck coefficient measurement system.

The ZEM-3 measurement requires a rectangular-shaped sample with dimensions of 3x3x6mm, and all the measurements are conducted under a low helium (He) atmosphere to create a conductive environment.

4.4.3 Vickers Hardness Test

The micro hardness of the samples is determined using the Shimadzu HMV-G Series Micro Vickers Hardness Tester. The basic principle involves applying varying loads to a sample surface and measuring the diagonals of the resulting marks, which provide the Vickers hardness value. An illustration of the Vickers test is given in Figure 4. 10 below.

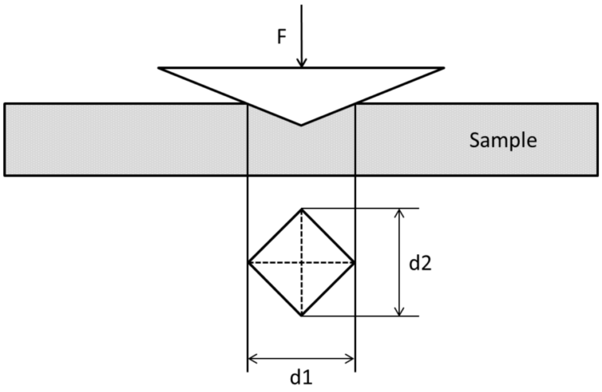

Figure 4. 10 The illustration of the Vickers Hardness Test

Before starting the measurement, the sample is polished to obtain a smoother and flatter surface. Afterward, several loads are applied to a sharp-tipped diamond indenter. The applied load is kept around 10 to 15 seconds straight without moving or slipping the indenter, followed by removing the indenter from the surface of the sample. The indenter diagonals are measured to determine the Vickers values. The equations 26 and 27 given below are used for determining the Vickers hardness.

$$d = \frac{d_1+d_2}{2} \qquad \text{Equation 26}$$

$$HV = 0.102.\frac{2.F.sin\frac{136°}{2}}{d^2} = 0.1891 * \frac{F}{d^2} \qquad \text{Equation 27}$$

Chapter 5:

RESULTS AND DISCUSSION

5.1 Results of Thermoelectric Phosphides

In this section, we analyze the results of the synthesized binary and ternary metal phosphides GaP, NaSnP, and LiSrP.

5.1.1 Preparation

The preparation methods are explained in detail in Chapter 4. The solid-state and mechanical alloying methods are tested to determine the proper synthesis method for the metal phosphides. Since raw materials and the target compounds can be highly air-sensitive and reactive, all the precursors were weighed under an argon-filled glovebox with the proper stoichiometry of GaP, NaSnP, and LiSrP.

The solid-state synthesis method is tested on the NaSnP ternary phase. Three different synthesis reactions were performed using an excess amount of Sn (17 wt.%, 9.5 wt.%, and 7.7 wt.%) to determine the proper stoichiometry for obtaining the ternary phase. The proper amount of elements was weighed inside the argon-filled glovebox. Afterward, they were placed inside an aluminum crucible, and then the crucible was placed inside a quartz tube on top of a glass wool to prevent the breakage of the tube. Further, the quartz tube was closed. The prepared quartz tube was removed from the glovebox and placed in a vacuum oven with an argon gas flow. Then, the heat treatment method was applied at 275 ºC for 2 hours and then at 500 ºC for two days. When the heat treatment is completed and the quartz tube has cooled to room temperature, the argon flow was cut, and it was taken out from the furnace. After that, the tube was carefully opened under a hood to prevent the high reactivity of phosphorus, and then the aluminum crucible was taken out. Figure 5. 1 b shows the quartz tube taken out from the furnace and the aluminum crucible holding the end product. The end result from the 9.5 wt. % and 7.7 wt. % is seen in Figure 5. 1 c, and it did not yield successful results. These results have prompted us to consider adjusting the parameters in our experiments.

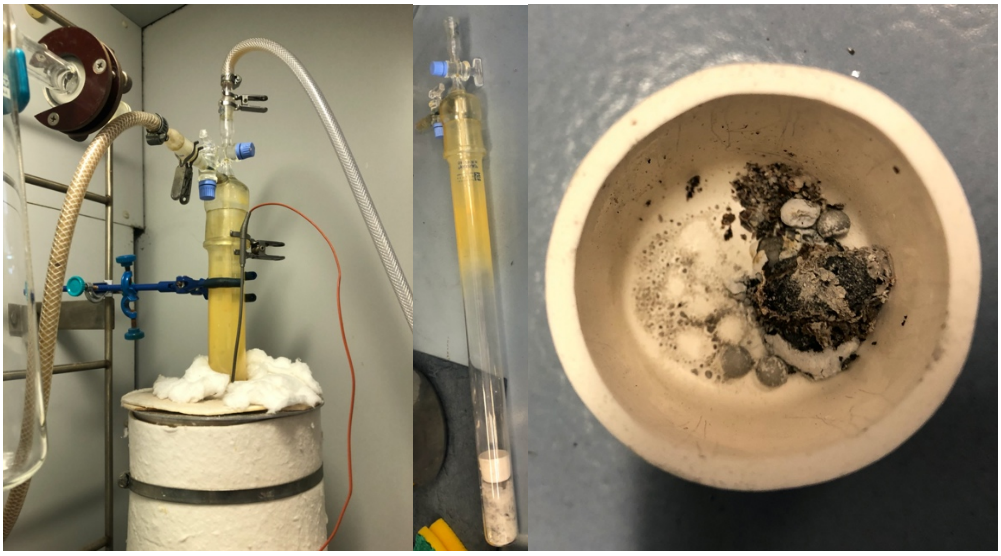

a) **b)** **c)**

Figure 5. 1 a) Quartz tube inside the vacuum oven after heat treatment, **b)** quartz tube removed from the vacuum oven after the heat treatment, **c)** sample after the heat treatment.

When the first setup was not successful, we attempted the 17 wt. % sample in another solid-state synthesis without using the aluminum crucible. Similar to the previous synthesis, elements were weighed with the proper stoichiometric ratios in an Ar-filled glove box and placed inside a smaller-size quartz tube, which was then sealed under vacuum. The quartz tube was placed in an oven inside an aluminum crucible on top of a glass hole with a vertical direction. Heat treatment was applied, starting with 275°C for 12 hours and 500°C for a day. After the heat treatment was complete, the quartz tube was allowed to cool to room temperature, then taken out from the oven and placed under a hood to prevent the reaction of excess phosphorus with the air. The tube was opened with the help of a hammer, and the sample was extracted. Figure 5. 2 showed the before and after pictures of the heat-treated sample tube, displaying the removed sample. When the sample was taken out from the tube, it immediately changed color from grey to a yellowish hue. After a couple of minutes, the sample started to react in the air atmosphere and ignited. This synthesis became unsuccessful because of the inhomogeneous appearance of the sample, which was similar to the previous synthesis. Rather than changing the parameters, we decided to change the synthesis route.

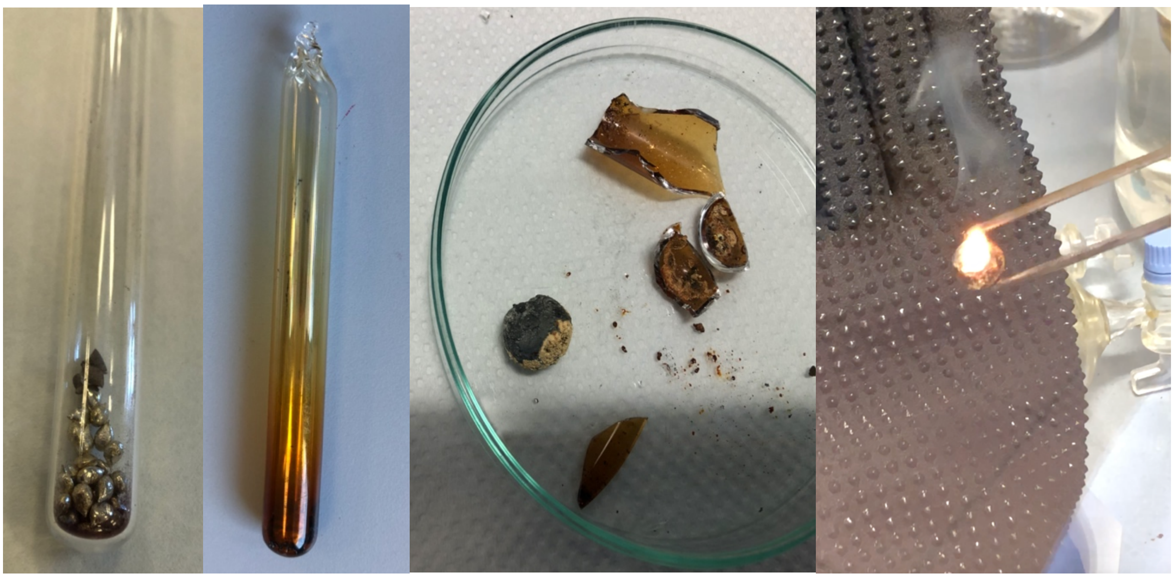

Figure 5. 2 a) Quartz tube sealed under vacuum, **b)** quartz tube after taken out from the oven, **c)** sample taken out from the tube, **d)** sample that is reacted after a while.

For the mechanical alloying process, the weighed samples were placed inside a stainless-steel vial with four-quarter inch and two half-inch stainless-steel balls, tightly closed inside the glovebox. Mechanical alloying was carried out with SPEX 8000D. To determine the correct synthesis time, ball milling was done in two-hour periods. Between the periods, the stainless-steel vial was placed back inside the glove box, and the sides of the vial were scraped out using a spatula to acquire a homogeneous sample. Later, the proper reaction time was determined as 4 hours. To obtain the desired products, stainless-steel vials were placed back inside the glovebox, and the prepared black powders were taken out. Furthermore, to achieve denser products, powders were sintered using SPS, which was explained in detail in Chapter 4. However, NaSnP and SrLiP showed high air sensitivity, causing samples to flame when exposed to air or moisture as represented in Figure 5. 3. Only GaP samples were able to densify with SPS.

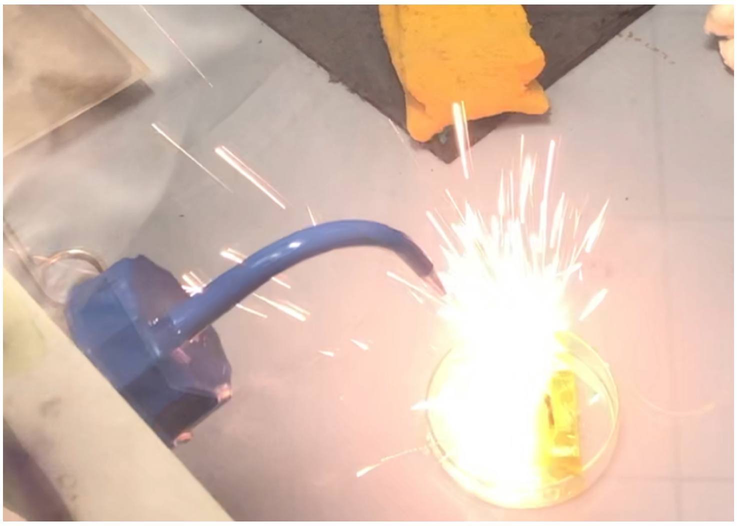

Figure 5. 3 SrLiP sample synthesized with mechanical alloying technique when it is exposed to moisture.

Before undergoing the SPS treatment, the graphite dies were covered with a 1mm-thick graphite foil. The synthesized powder metal phosphide samples were placed between layers of graphite punches covered with 10 mm diameter graphite foil stamps. Before placing the graphite die into the SPS, cold pressing was applied to obtain better results. Prepared graphite dies with powder samples inside were placed between punch electrodes in the vacuum chamber. After achieving a vacuum environment, the sintering process was carried out. All SPS processes were conducted under a 50MPa pressure at 600°C, with varying time periods between 5 to 10 minutes.

We aim to explore the thermoelectric properties of metal phosphides by synthesizing binary GaP and ternary SrLiP and NaSnP phases using both solid-state and mechanical alloying techniques, varying the stoichiometric ratios and synthesis durations as tabulated in Table 2.

Table 2 Preparation conditions of Metal Phosphide Samples.

Sample Name	**Composition**	**Excess Addition**	**Heat Treatment Temperature**	**Time Duaration for Heat Treatment**	**Ball Milling Time**	**SPS Temperature (C^o)**	**SPS Time (min)**
BG-FLX1	$NaSn_4P$	17 wt. % Sn	500 C^o	2 days	-	-	-
BG-FLX2	$NaSn_8P$	9.5 wt. % Sn	500 C^o	2 days	-	-	-
BG-FLX3	$NaSn_{10}P$	7.7 wt. % Sn	500 C^o	1day	-	-	-
BG1	NaSnP	-	-	-	2h	-	-
BG2	NaSnP	-	-	-	4h	-	-
BG3	NaSnP	-	-	-	6h	-	-
BG4	$NaSn_{0.95}P$	-	-	-	4h	400	5
BG5	$NaSn_{0.9}P$	-	-	-	4h	-	-
BG7	GaP	-	-	-	2h	600	5
BG9	GaP	-	-	-	2h	600	10
BG10	GaZnP	-	850 C^o	-	2h	600	10
BG13	GaZnP	-	-	-	2h	900 C^o	20
BG11	GaSP	-	450 C^o-850 C^o	1day-1day	2h	800C^o	30
BG34-1	SrLiP	-	-	-	4h	-	-

5.2.2 Crystal Structure Characterization

We employed XRD using a Cu-Kα source with a wavelength of 1.5406 Å to determine the crystal structures and specify the phase purities of all the samples. Figure 5. 4 a shows XRD results of NaSnP compounds with different ball milling times, named as NaSnP-2h (BG1), NaSnP-2h-2h (BG2), and NaSnP-2h-2h-2h (BG3), respectively.

As seen in Figure 5. 4 a, all the main peaks from hexagonal NaSnP ($P6_3mc$ space group) matched the synthesized samples' XRD patterns well. In the 2h ball milled NaSnP sample, elemental Sn peaks represented with α were very intense; thus, trying 4h and 6h ball milling synthesis times was considered. The 4h ball-milled sample, represented by the blue line, had reduced Sn peak intensities but was not fully eliminated. After trying 6h ball milling synthesis, represented by the green color, Sn peaks were further reduced, but as with the 4h sample, they were not fully gone. Due to this circumstance, we reduced the Sn amount and synthesized the same composition with a 4h ball milling time. Figure 5. 4 b provided the XRD patterns of $NaSn_{0.95}P$ (BG4) and $NaSn_{0.9}P$ (BG5) samples. As decided, a 4h ball milling process within 2h scraping was applied for both. However, the elemental Sn peaks represented with α still existed for both $NaSn_{0.9}P$ (green) and $NaSn_{0.95}P$ (pink) samples. To obtain a perfect match with the theoretical pattern for NaSnP compound, samples were attempted to be sintered at 400°C for 5 minutes. Unfortunately, the synthesized samples were only stable in an inert atmosphere, and when exposed to air or moisture, they rusted, changed color, or ignited immediately.

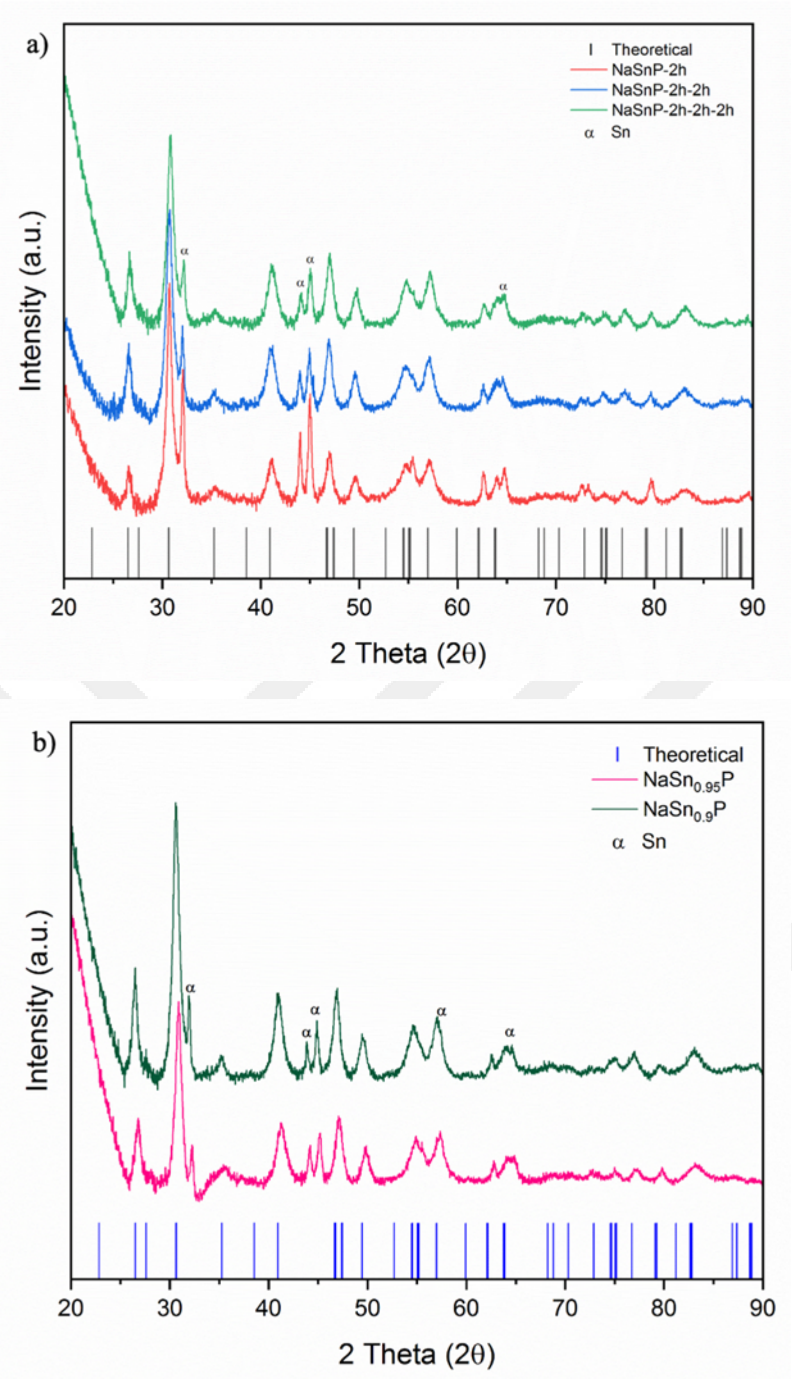

Figure 5. 4 XRD patterns of **a)** NaSnP samples. NaSnP-2h (red) ball milled for 2 hours, NaSnP-2h-2h (blue) ball milled for 4h and in between 2h scraped in glove box and NaSnP-2h-2h-2h (green) ball milled for 6h and in between 2h periods sample is scraped in glove box. **b)** $NaSn_{0.9}P$ (green) and $NaSn_{0.95}P$ (pink) samples.

After this negative result, the SrLiP ternary phase was tested. It was observed from the XRD pattern in Figure 5. 5 that the synthesized SrLiP matched well with the hexagonal $P6_3/mmc$ space group theoretical pattern without any impurity or excess compound. Unfortunately, when exposed to air or moisture, the synthesized powder sample showed high air sensitivity. Therefore, we decided not to proceed with the thermoelectric property measurements for these ternary phosphides.

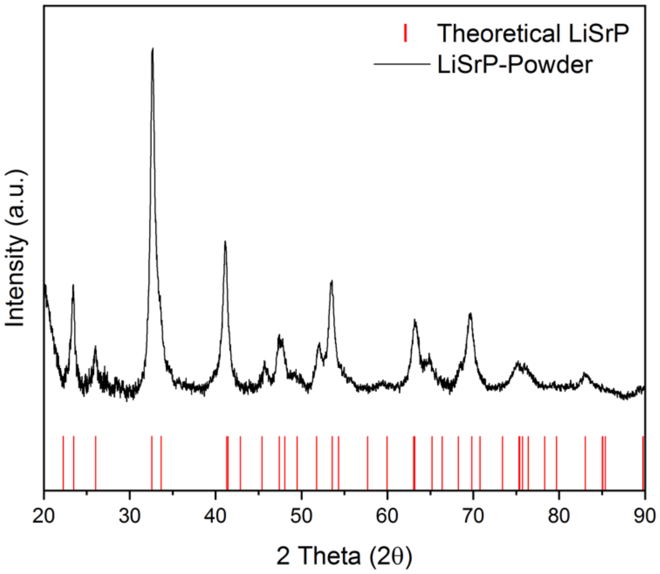

Figure 5. 5 XRD pattern of hexagonal SrLiP synthesized whit mechanical alloying.

Besides the ternary phosphides, we tested a binary compound, GaP which should be stable in air. The XRD pattern of the synthesized GaP and theoretical peaks is given in Figure 5. 6. As seen in the Figure 5. 6 a, the powder sample (light pink) matched the theoretical pattern well. To densify the powder and obtain crystalline peaks, the SPS process was applied at 600°C in changing periods. The orange line represented the GaP sample sintered for 5 minutes, and the purple line represented the sample sintered for 10 minutes. As seen in Figure 5. 6 a, when the sample was exposed to temperature for long periods, the phosphorus content was vaporized, leaving elemental gallium behind. The peaks in the purple line, represented with Φ, were the elemental gallium peaks. However, we could not make further thermoelectric measurements due to the high resistivity of GaP that we couldn’t even measure with our ZEM-3 system.

After obtaining negative results from undoped GaP samples, we attempted to dope the samples to achieve high carrier concentrations for measuring thermoelectric properties. Miyauchi et al. (96) reported that Zn-doped samples synthesized with the solution-growth method have p-type conduction with high carrier concentration. Thus, we decided to dope the samples with Zn by changing the synthesis method to high-speed ball milling. The XRD measurements of GaP samples doped with elemental Zn are given in Figure 5. 6 b. The synthesized powder GaP-Zn (light pink) matched the theoretical GaP peaks well, but the doped Zn could not be detected from the powder sample. To remove excess P, Ga, or Zn, the sample was annealed under an Ar atmosphere at 850°C placed in a quartz tube. After the annealing process was done, the tube had a yellowish color, representing the excess P vaporized during the annealing process. The XRD pattern of the annealed sample was represented by the light green line, and all the peaks matched the theoretical pattern well with high crystalline peaks. To obtain high-density samples, the annealed sample was sintered for 20 minutes at 900°C without using a thermocouple in the SPS. The purple line represented the sintered sample XRD pattern, and it had a slight shift to the left side of the theoretical pattern, which may indicate that Zn2+ (ionic radii = 88 pm) successfully replaced the smaller Ga3+ (ionic radii = 76 pm) (97). However, the high resistivity of the sample again prevented us from performing electronic transport measurements.

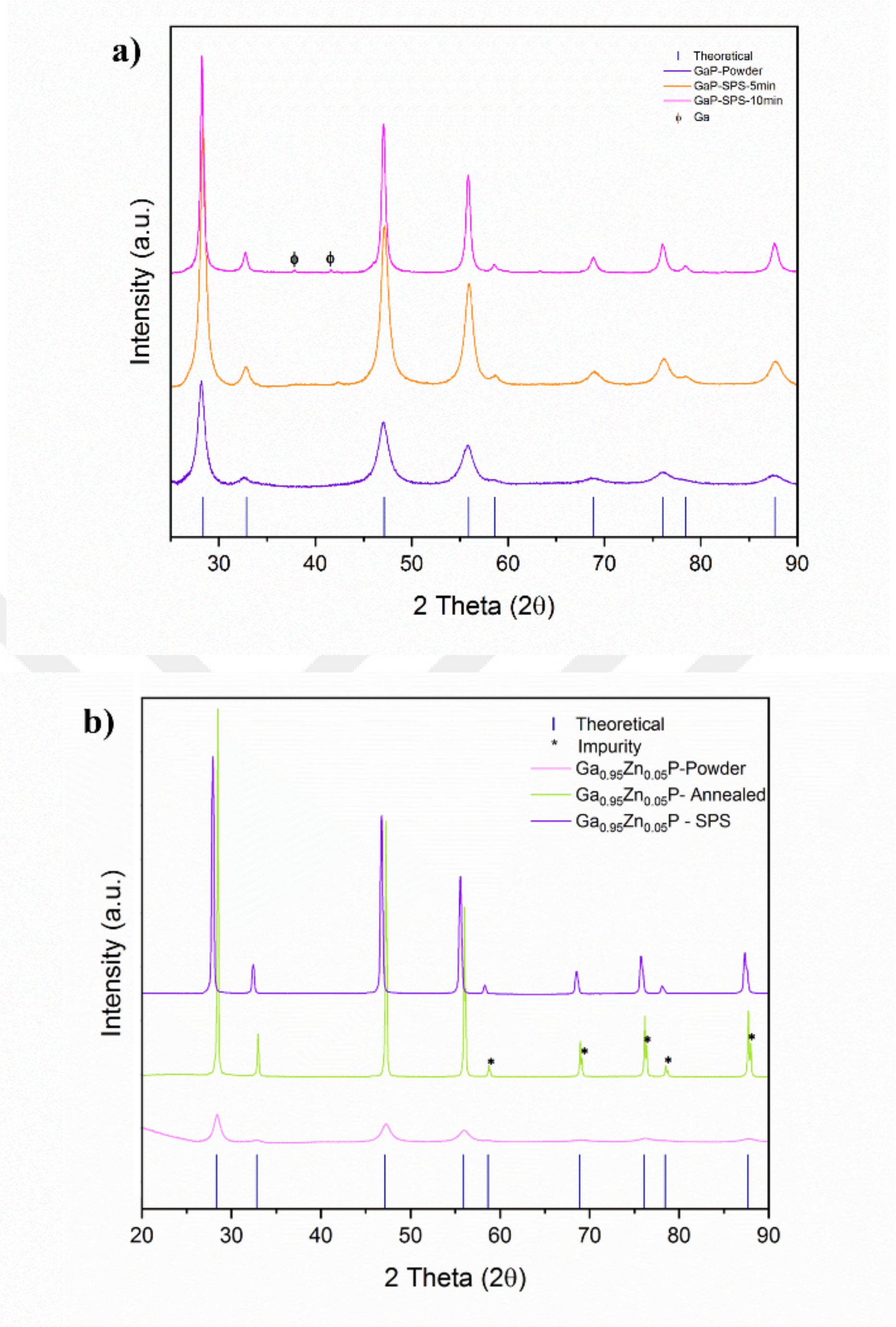

Figure 5. 6 XRD patterns of the **a)** undoped GaP powder (pink), after 5min sintering process (orange) and after 10min sintering process (purple), **b)** the elemental Zn doped GaP powder sample (pale pink), GaZnP powder sample after annealing with Ar (green) and annealed GaZnP sample sintered for 20 min at 900 C°.

5.2 Results of Thermoelectric Zintl Phases

In this section, the n-type properties of $CaMg_2Sb_2$ and $CaMg_2Bi_2$ as 1-2-2 Zintl phases were discussed. As considered before, the n-type Mg_3Sb_2 compound had better electrical properties compared to its p-type counterparts (53, 56). Because of this particular reason, a similar strategy in the $Mg_{3.2}Sb_{1.5}Bi_{0.49}Te_{0.01}$ compound was selected to change the electrical conduction of these p-type compounds to n-type. $CaMg_2Sb_2$ and $CaMg_2Bi_2$ compounds exhibited p-type conduction at low temperatures. However, doping with a proper amount of La and Te could change the conduction of p-type $CaMg_2Sb_2$ and $CaMg_2Bi_2$ compounds to n-type.

5.2.1 Preparation

The preparation route was detailed in Chapter 4. Elemental Mg exhibited air-sensitive properties when exposed to air. Additionally, the high-energy ball milling technique intensified the reactivity rate of this element; therefore, all the preparation steps were conducted under an Ar-filled glove box. Depending on the compositions, the proper amount of elements to obtain $Ca_{0.8}La_{0.2}Mg_{2.1}Sb_2$, $Ca_{0.9}La_{0.1}Mg_{2.1}Sb_{1.95}Te_{0.05}$, $Ca_{0.8}La_{0.2}Mg_{2.1}Bi_2$, and $Ca_{0.9}La_{0.1}Mg_{2.1}Bi_{1.95}Te_{0.05}$ was weighed and placed inside stainless steel vials. The vials were also filled with either two half-inch stainless steel balls or, in certain cases varying by composition, a combination of two half-inch and four-quarter-inch stainless steel balls was used. After placement, the vial was tightly sealed and placed inside the SPEX800D for 90 minutes. Every 30 minutes, the vial was returned inside the glovebox, and the sides were scraped to obtain a homogeneous powder. After mechanical alloying was completed, a dark gray powder was removed from the vial inside the glovebox. SPS was conducted to achieve higher density bulk products.

Before starting the SPS treatment, graphite dies were covered with a 1mm thickness of graphite foil after powder samples were placed between the graphite punches, as shown in Figure 4. 3. Additionally, 10mm diameter size stamp-shaped graphite foils were placed before the powder sample on top of the punches. The filled graphite dies were placed inside the vacuum chamber between the punch electrodes. After the vacuum level dropped to below 2.3 Pa, the sintering process was carried out. The SPS process ran for 10 minutes at 600°C and 50 MPa pressure for all the samples.

By changing the dopants and their amounts on the 1-2-2 compounds ($CaMg_2Sb_2$ and $CaMg_2Bi_2$), the effects on the thermoelectric properties of these materials are investigated (Table 3).

Table 3 Preparation conditions of the $CaMg_2Sb_2$ and $CaMg_2Bi_2$ based compounds.

Sample Name	Composition	Milling Time (min.)	Ball Size and Amount	SPS Time (min.)	SPS Temperature (C^o)
BG 28	$CaMg_2Sb_2$	90	1/4", 4 and 1/2" ,2	10	600
BG24	$Ca_{0.8}La_{0.2}Mg_{2.1}Sb_2$	90	1/4", 4 and 1/2" ,2	10	600
BG25	$Ca_{0.9}La_{0.1}Mg_{2.1}Sb_{1.95}Te_{0.05}$	90	1/4", 4 and 1/2" ,2	10	600
BG32	$CaMg_2Bi_2$	90	1/4", 4 and 1/2" ,2	10	600
BG26	$Ca_{0.9}La_{0.1}Mg_{2.1}Bi_{1.95}Te_{0.05}$	90	1/4", 4 and 1/2" ,2	10	600
BG27	$Ca_{0.8}La_{0.2}Mg_{2.1}Bi_2$	90	1/4", 4 and 1/2" ,2	10	600

5.2.2 Cristal Structure Characterization

To specify the crystal structure and identify possible impurities, an XRD with a Cu-K_α source (1.5406Å) was used. For characterization, a 40kV voltage and 20mA current were applied. Figures 5. 7 a and 5. 7 b show the XRD patterns of the Sb-based and Bi-based Zintl compounds in powder and pellet forms after the SPS treatment.

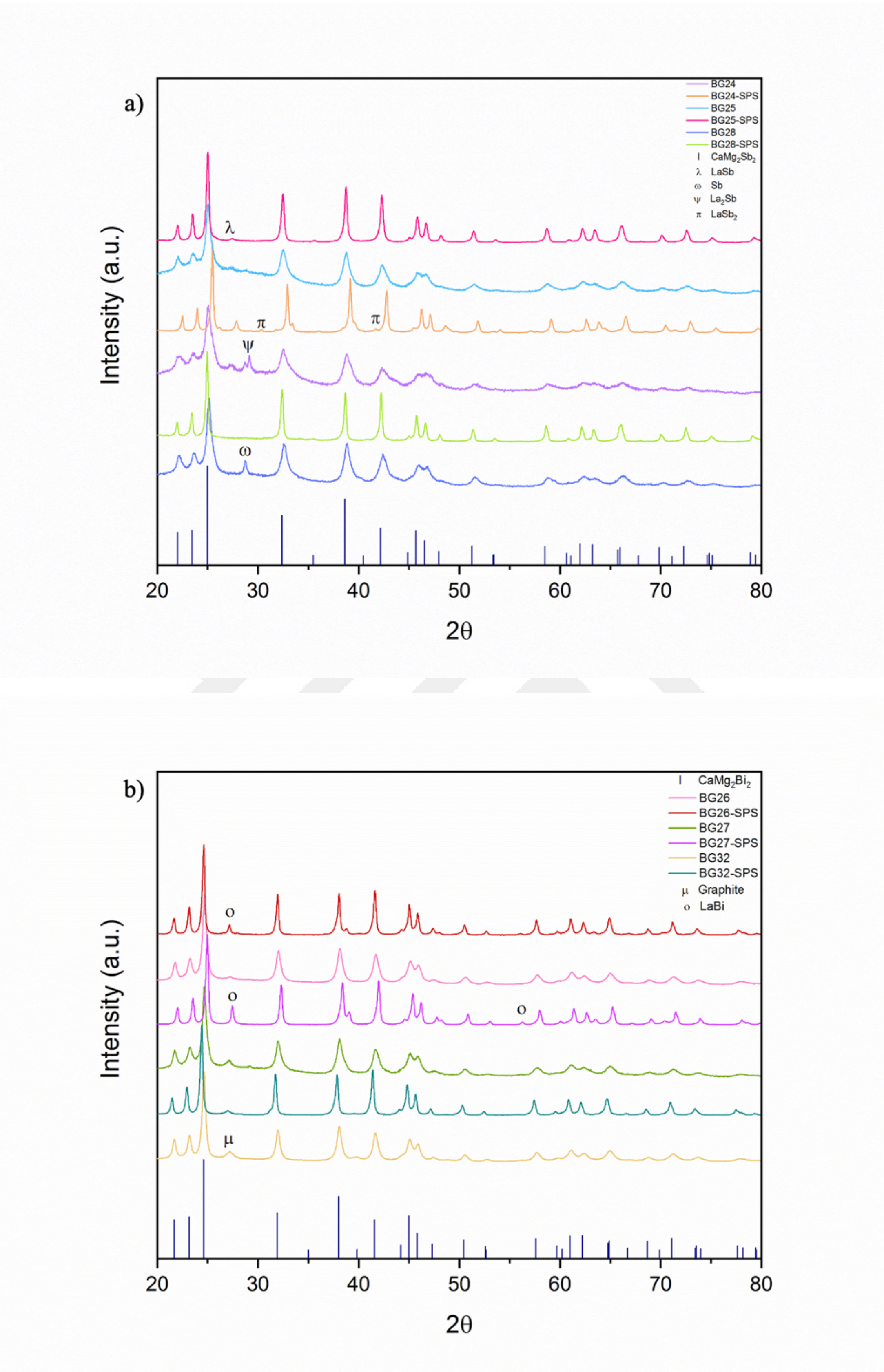

Figure 5. 7 XRD patterns of **a)** $CaMg_2Sb_2$ based compounds **b)** $CaMg_2Bi_2$ based compounds before and after SPS treatment.

As seen above, all the XRD peaks in Figure 5. 7 a and b well matched with the trigonal $CaMg_2Sb_2$ and the $CaMg_2Bi_2$ from the $P\overline{3}m1$ space group, respectively. First, to determine the conductivity type of these compounds, undoped samples BG28 and BG32 were synthesized. In Figure 5. 7 a, the undoped $CaMg_2Sb_2$ powder sample (BG28) showed elemental Sb, which could be related to the loss of Ca and Mg in the synthesis step. After determining the conduction type of the structure, doping the samples with La and Te was conducted. However, after doping with La, Sb peaks were either fully gone or significantly reduced.

Elemental Mg has a high vapor pressure; thus, to reduce the possible deficiency of Mg in the synthesis, La and Te-doped samples with excess elemental Mg are performed. To achieve all n-type samples, the doping principle that Tamaki et al. (60) established is considered, and elemental Te doping was introduced to the structure along with elemental La doping. The compounds $CaMg_{2.1}Sb_2$ and $CaMg_{2.1}Bi_2$ form the basis of this thesis.

Due to La doping, Sb-based compounds (BG24 and BG25) included binary compounds like LaSb, $LaSb_2$, and La_2Sb. Comparing the La-doped samples, as seen in Figure 5. 7 a, the $Ca_{0.8}La_{0.2}Mg_{2.1}Sb_2$ (BG24) sample had a high-intensity LaSb and $LaSb_2$ peak compared to the $Ca_{0.9}La_{0.1}Mg_{2.1}Sb_{1.95}Te_{0.05}$ (BG25). Since LaSb is the most stable structure in the formation energy diagram, intense LaSb peaks were expected to be revealed (98). Unfortunately, doping levels below 100% represented that the doping yield is lower than expected.

As represented in Figure 5. 7 b, due to La doping, the BiLa compound peak is determined for Bi-based compounds. Similar to the Sb-based compounds, the higher La doping sample (BG27) had a higher BiLa content. The graphite peaks valid in the undoped sample are not permanent and could be eliminated by sanding.

5.2.3 Transport Property Analysis

5.2.3.1 Results from La and Te Doped $CaMg_2Sb_2$ Samples

In our study, we prepared all the samples of $CaMg_2Sb_2$ using the method described in Chapter 4. We compared undoped $CaMg_2Sb_2$ (yellow line) with samples doped with La and Te. The undoped sample exhibited higher resistivity values and showed hysteresis during heating and cooling. This higher resistivity of the undoped sample caused lower electrical conduction of the material. The insets within Figure 5. 8 a provided close-up view of the doped samples. The blue line represented the La and Te doped sample, while the red line represented the La doped sample. Doping with La decreased the resistivity, and further doping with Te reduced it even more. All the samples exhibited decreasing resistivity as the temperature reached 450K. However, the resistivity reduction in the La and Te doped sample (blue line) continued at higher temperatures, indicating that it behaved as a semiconductor throughout the temperature range. After doping the $CaMg_2Sb_2$ sample with La and Te, the samples showed a significant decrease in resistivity at lower temperatures, with minimal change at moderate temperatures. The sharp reduction in resistivity may have stemmed from the high n-type carrier concentration introduced with external doping. Wang et al. reported that increasing the Mg content and use Te as a substituting dopant on the Sb side lower the resistivity value by increasing the carrier concentration and the mobility of the sample (99).

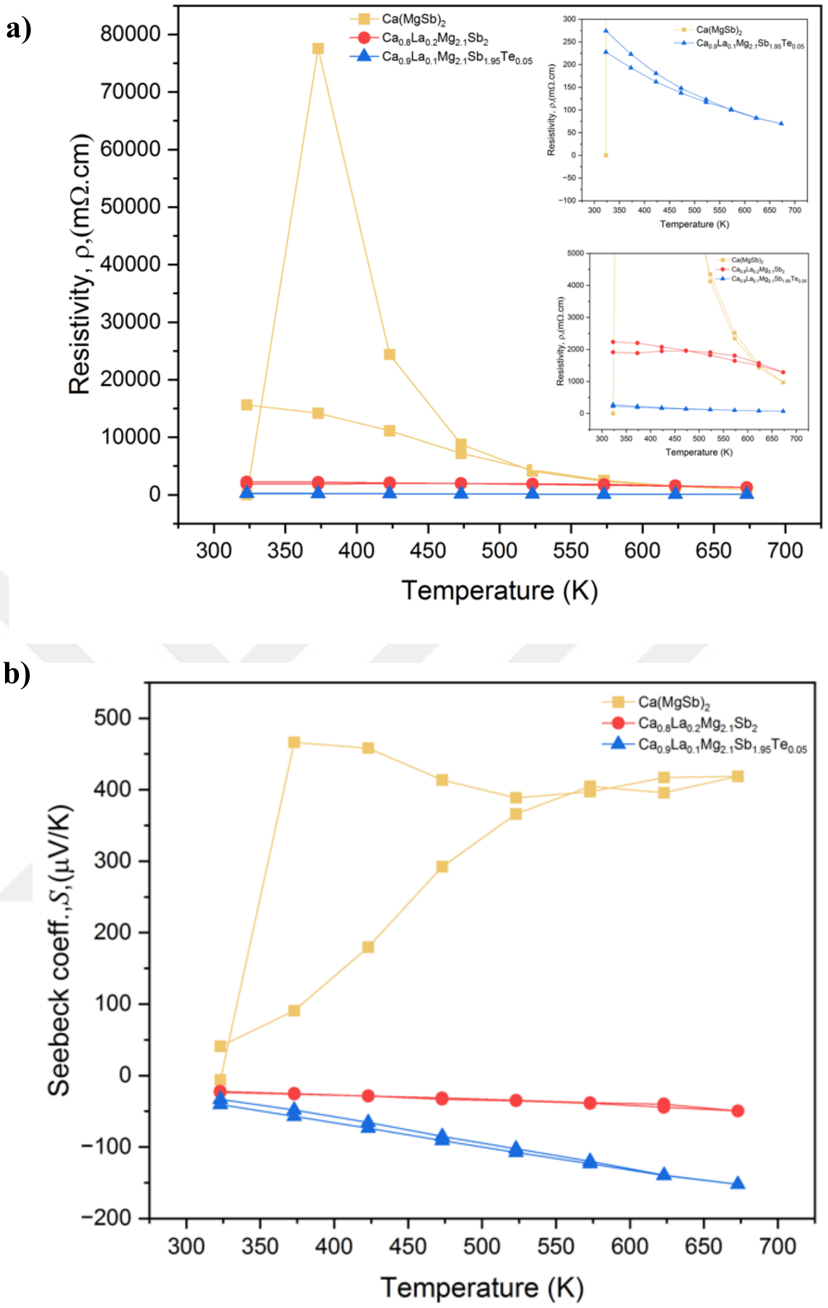

Figure 5. 8 $CaMg_2Sb_2$ compounds thermoelectric measurements **a)** Resistivity and **b)** Seebeck coefficient as a function of temperature.

In Figure 5. 8 b, the undoped sample (yellow line) initially showed a negative Seebeck coefficient value and later exhibited a positive Seebeck coefficient, indicating that the material displays p-type conduction for most temperature values. This behavior was attributed to the loss of Mg and Ca during the synthesis; thus, increasing the Mg content in the doped samples was feasible (99, 100). After the samples are doped, the Seebeck coefficient values turned negative, representing that the materials had gained n-type conduction characteristics. The sample doped only with La (red line), when compared with the Te-doped sample, had consistently lower absolute Seebeck coefficient values. However, both follow similar paths throughout the temperature range.

Figure 5.9 depicts the thermal conductivity values of $CaMg_2Sb_2$-based samples as a function of temperature. As illustrated, the thermal conductivity values exhibited a decrease with the incorporation of doping elements into the sample. The most substantial decrease is observed in the sample doped with both La and Te. Such a high reduction of thermal conductivity should have been due to alloy scattering. When the resistivity of the samples significantly decreases, we expect an increase in the electronic thermal conductivity due to the introduction of doping. The electronic contribution of the thermal conductivity is proportional to the number of free charge carriers.

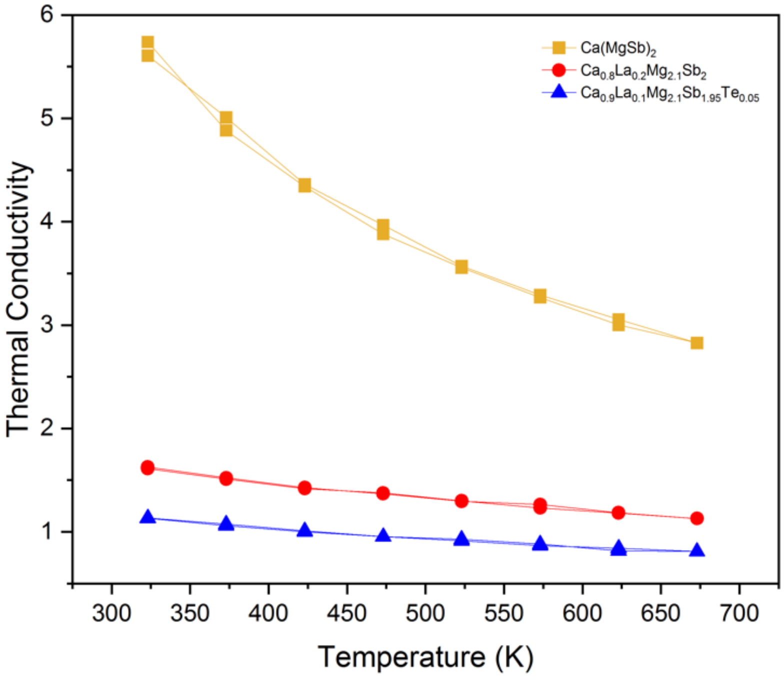

Figure 5. 9 $CaMg_2Sb_2$ compounds thermal conductivity values as a function of temperature.

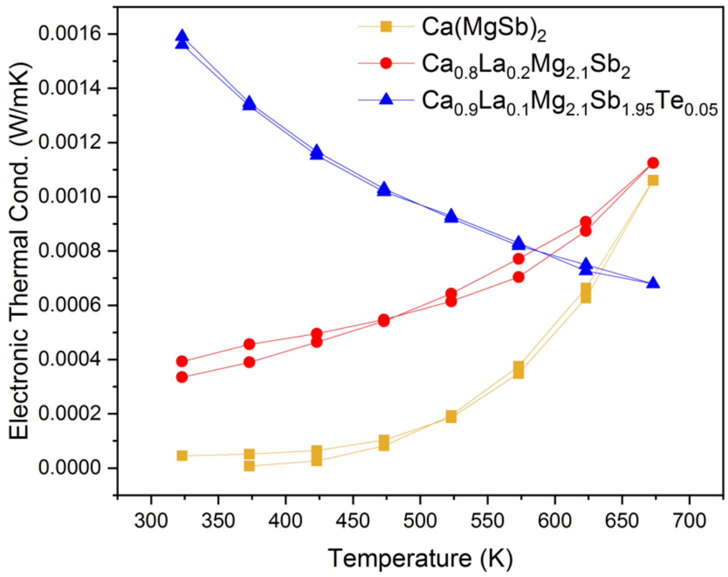

Figure 5. 10 $CaMg_2Sb_2$ compounds' electronic thermal conductivity values as a function of temperature.

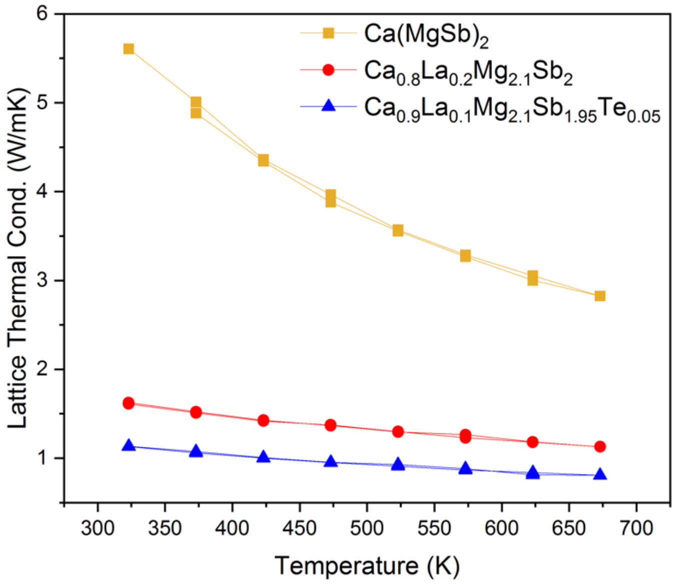

Figure 5. 11 $CaMg_2Sb_2$ compounds' lattice thermal conductivity values as a function of temperature

As represented in Figure 5.10, the introduction of La and Te to the system increases the electronic thermal conductivity values. In Figure 5.11, the change in lattice thermal conductivity is represented. It seems that the lattice thermal conductivity values decreased after the introduction of La and Te because the doping created additional scattering centers in the structure. This occurred because of La is a larger atom compared to Ca, and Te is a heavier atom compared to Sb. The results consistently show that both La and Te doping contribute to lowering lattice thermal conductivity. This indicates that the combined doping of La and Te enhances phonon scattering mechanisms within the crystal lattice, significantly impeding the phonons' ability to transport heat (99). The total thermal conductivity is dominated by the lattice contribution due to the very high resistivity observed for all the investigated samples.

5.2.3.2 Results from La and Te Doped $CaMg_2Bi_2$ Samples

All sample preparations were conducted consistently and were comprehensively explained in Chapter 4. Referring to Figure 5. 12, it was evident that the Te-doped sample (burgundy line) exhibited significantly higher resistivity values compared to the undoped sample. The insets on the right side of the graph represented the undoped $CaMg_2Bi_2$ (cyan line) and La-doped (pink line) samples. Notably, all the samples exhibited a similar trend as semiconductor-like behavior. Both doped samples displayed high resistivity values, indicative of low electrical conductivity. Doping the $CaMg_2Bi_2$ sample with La (pink line) resulted in a limited increase in resistivity at lower temperatures, although this difference lessened at moderate temperatures. In contrast, the addition of Te to the La-doped sample had a substantial impact on resistivity values, with the highest effect observed. During the cooling phase, the resistivity values of the doped samples mirrored the trajectory observed during the heating phase.

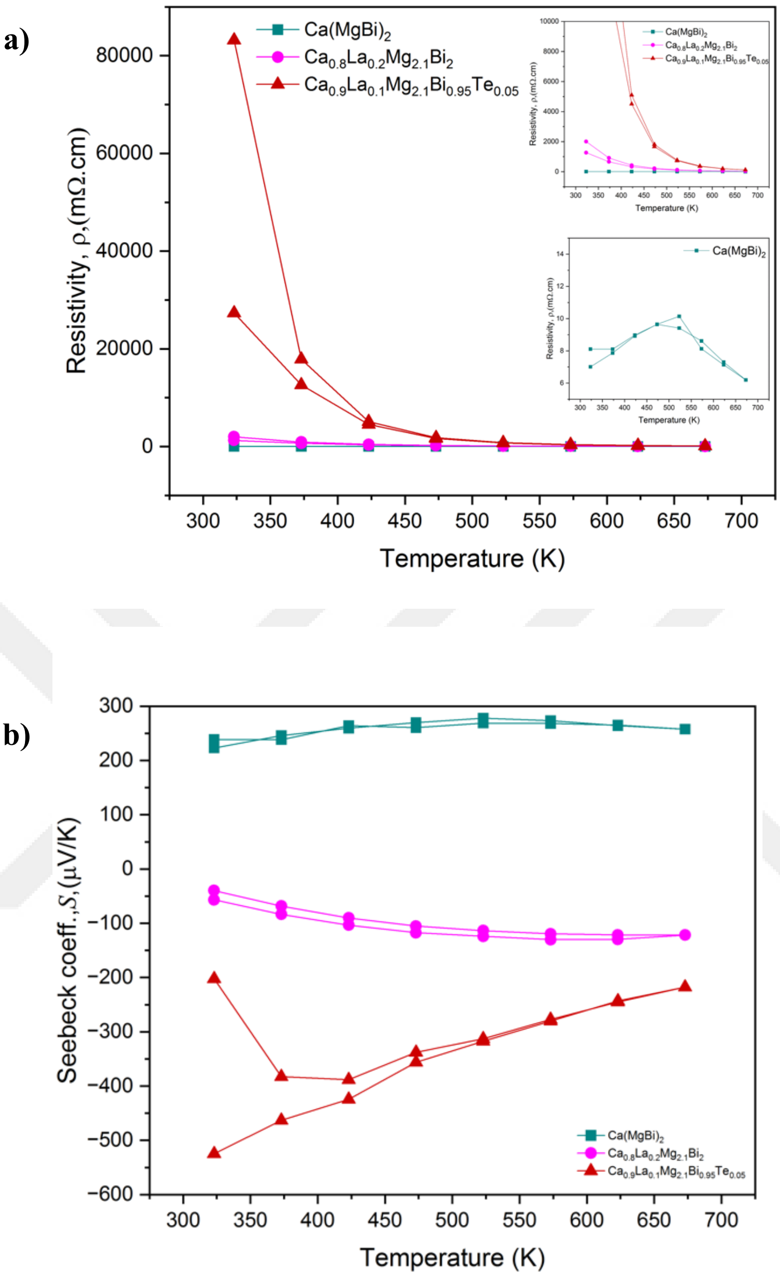

Figure 5. 12 $CaMg_2Bi_2$ compounds thermoelectric measurements **a)** Resistivity and **b)** Seebeck coefficient as a function of temperature.

As seen from Figure 5. 12 b, the undoped $CaMg_2Bi_2$ sample had positive Seebeck values, demonstrating p-type conduction. Similar to the previous samples, this could be explained by the decreased amounts of Ca and Mg in the sample during the synthesis reaction, resulting in increased Mg content in the doped samples. After doping, the samples' Seebeck coefficient values became negative, indicating n-type conduction. When comparing doped samples to each other, the sample with La and Te showed higher absolute negative Seebeck coefficient values that increased with temperature. Zhang et al. obtained the same trend with his Te doped samples (59). Decreasing trend of the Te and La doped sample can be explained by the degenerate semiconducting behavior of the sample (101). However, both doped samples followed a similar trajectory.

Figure 5.13 represents the thermal conductivity values of undoped and doped $CaMg_2Bi_2$ samples. The highest thermal conductivity value is observed in the undoped sample. After increasing the Mg content and doping the sample, thermal conductivity values decreased, and the lowest thermal conductivity value was obtained in the sample including both La and Te, similar to the $CaMg_2Sb_2$ case. The decreased in the thermal conductivity can be attributed by the Umklapp phonon scattering at high temperatures (59, 102). Lowering resistivity values should increase the values of electronic thermal conductivity. Figure 5.14 above represents the electronic contribution, and Figure 5.15 represents the lattice contribution of thermal conductivity values of $CaMg_2Bi_2$, respectively. As expected, the sample with the highest resistivity showed the lowest electronic thermal conductivity values. Similar to Sb based samples, the lattice thermal conductivity values of samples after doping with La and Te showed lower values because La is a larger atom compared to Ca, and Te is a heavier atom compared to Bi.

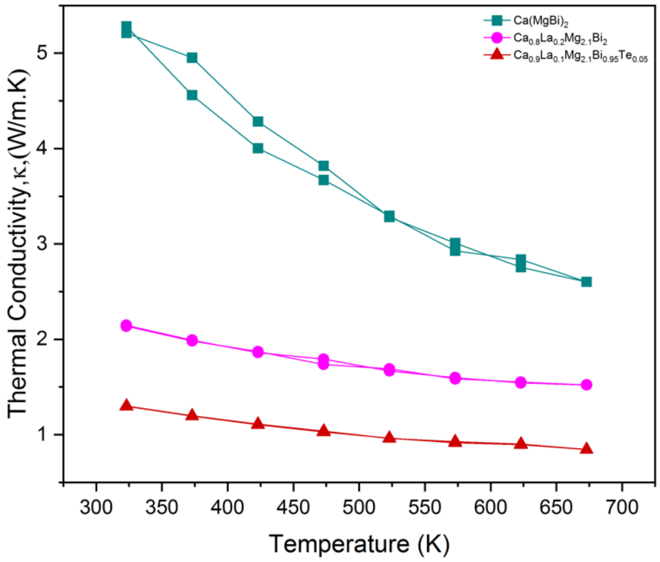

Figure 5. 13 $CaMg_2Bi_2$ compounds thermal conductivity values as a function of temperature.

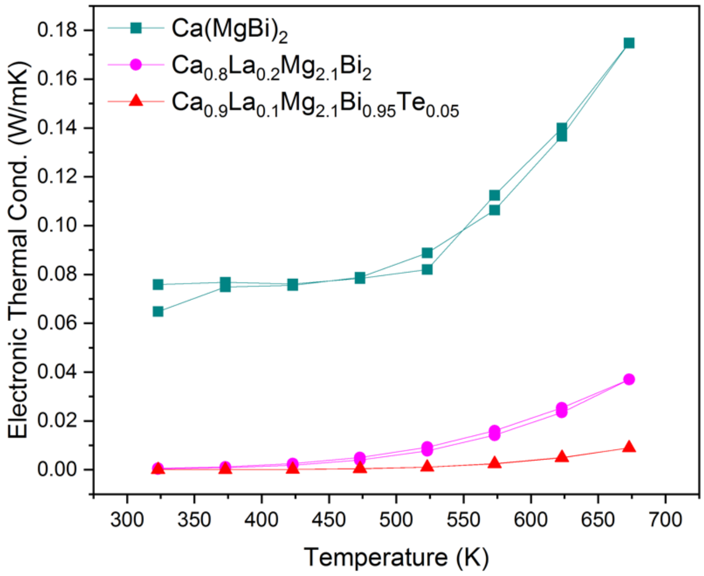

Figure 5. 14 CaMg$_2$Bi$_2$-based compounds' thermal conductivity values as a function of temperature.

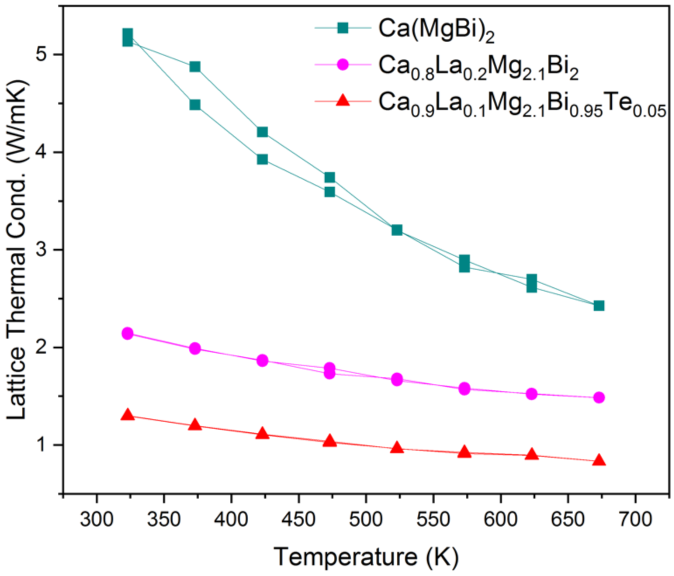

Figure 5. 15 CaMg$_2$Bi$_2$-based compounds' lattice thermal conductivity values as a function of temperature.

This can be explained by the fact that introducing La and Te to the structure creates mass disorder and strain into the crystal lattice, resulting in phonon scattering. Fundamentally, since the electronic resistivity of the samples is high, the main contribution of the thermal conductivity comes from the lattice part, and the electronic contribution can be neglected.

5.2.4 Electronic Transport Properties

$CaMg_2Sb_2$ and $CaMg_2Bi_2$ exhibited nondegenerate semiconducting behavior with low p-type carrier concentrations at increasing temperature values. Correspondingly, the resistivity values followed a decreasing path for both structures.

In Figure 5. 16 a, the Hall mobility of all samples was given. The red line and blue line represented the $CaMg_2Sb_2$-based samples without and with Te doping, respectively. The red line (BG24) represented the $CaMg_2Sb_2$ sample with La doping on the Ca side and had positive Hall mobility values throughout the entire temperature range, indicating that the sample had p-type carriers. The blue line (BG25) represented the $CaMg_2Sb_2$-based sample with La doping on the Ca side and Te doping on the Sb side, exhibiting negative Hall mobility values until it reached 650K. After doping with Te, sample gained semiconducting behavior witch changed the conduction type from p-type to n-type (99). After passing 650K, the Hall mobility values turned positive. This phenomenon could be attributed to the semiconducting behavior of the material, where the major charge carriers were electrons at lower temperature ranges, and at higher temperatures, positive charge carriers dominated. Also, at the temperature where the transition point occurred, positive carriers may have dominated the initial negative charges. The burgundy line representing the BG27 sample without Te doping ($Ca_{0.8}La_{0.2}Mg_{2.1}Bi_2$) had negative Hall mobility values along the full temperature range, indicating that the sample was dominated by negative charge carriers. From 425K to 500K, a continuous value change was observed. This change could be attributed to temperature-dependent scattering effects.

The pink line representing the BG27 sample with the $Ca_{0.8}La_{0.2}Mg_{2.1}Bi_2$ structure started with negative Hall mobility values, indicating that the dominated charge carriers were electrons. At 350K to 450K, a transition phase occurred, and the dominated charge carriers became holes rather than electrons. As the temperature increased, factors such as increasing scattering, impurities, or defects may have become prominent and changed the dominated charge carriers to electrons. The $CaMg_2Bi_2$-based samples showed the same pattern: as temperature increased, the mobility values decreased, indicating that acoustic phonons were the primary scattering sources.

In Figure 5. 16 b, carrier concentrations of all the samples are represented. As expected from the Seebeck data of the $CaMg_2Sb_2$ and $CaMg_2Bi_2$ samples, the samples with lower absolute Seebeck coefficients had higher n-type carrier concentrations. The Hall mobility data shown in Figure 5. 16 a is drawn with negative values on purpose to demonstrate that the samples displayed n-type conduction. The Bi samples showed much higher Hall mobility values than the Sb-based samples, which agreed with the literature (103, 104).

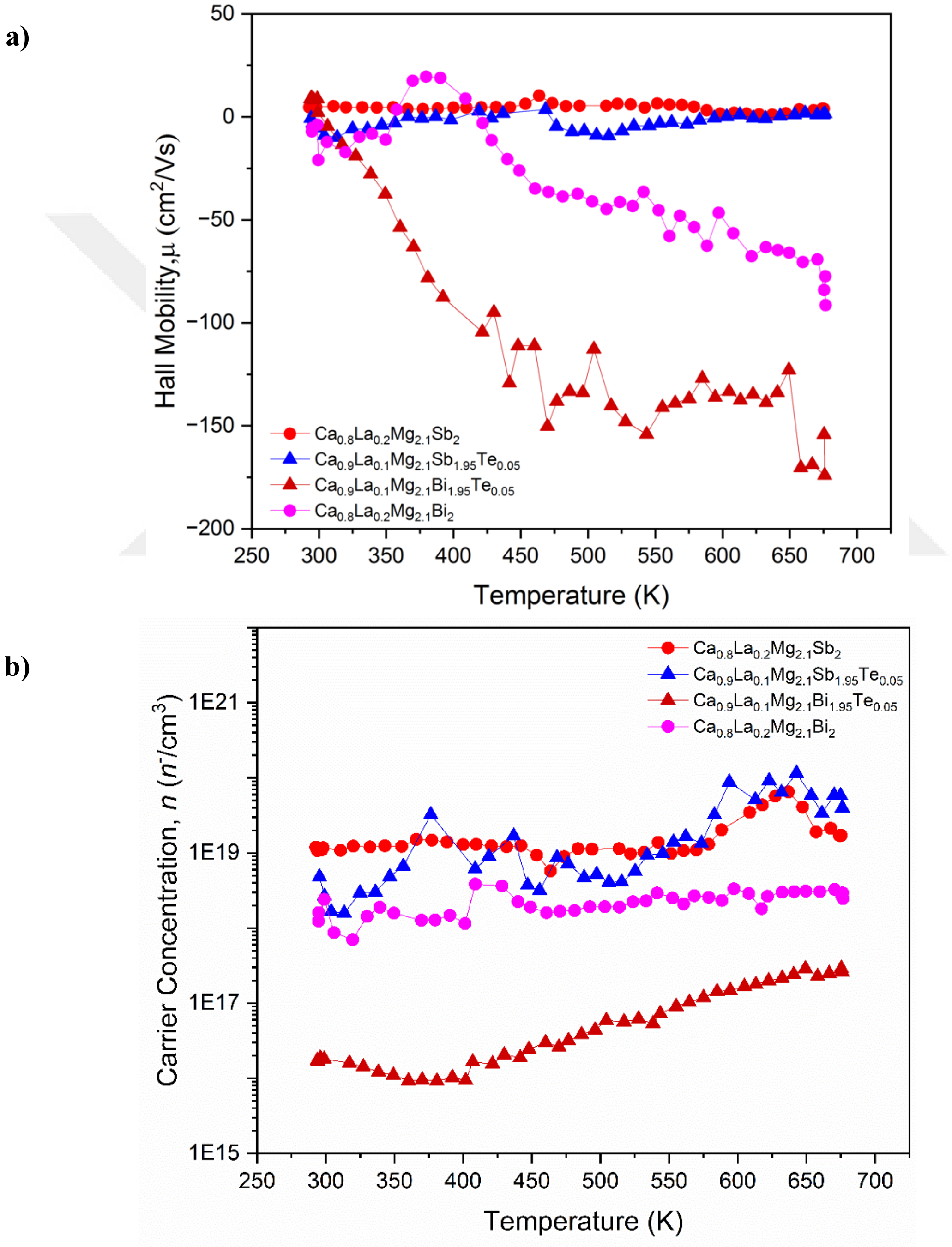

Figure 5. 16 The temperature dependence of **a)** Hall Mobility and **b)** Carrier concentration for $CaMg_2Sb_2$ and $CaMg_2Bi_2$ samples.

5.2.5 Chemical and Microstructural Characterization

5.2.5.1 La and Te Doped Sb Based Samples

To ascertain the chemical composition of the samples, Wavelength-Dispersive X-ray (WDX) analysis was employed. Figure 5. 17 a and b displayed the backscattered electron (BSE) and light optical images of the undoped $CaMg_2Sb_2$ (BG28) sample. In Figure 5. 17 a and b, red arrows indicated minority phases within the composition. In Figure 5. 17 c, the lighter spots, and in Figure 5. 17 d, the darker regions, represented by red dots, constituted the main matrix of the sample.

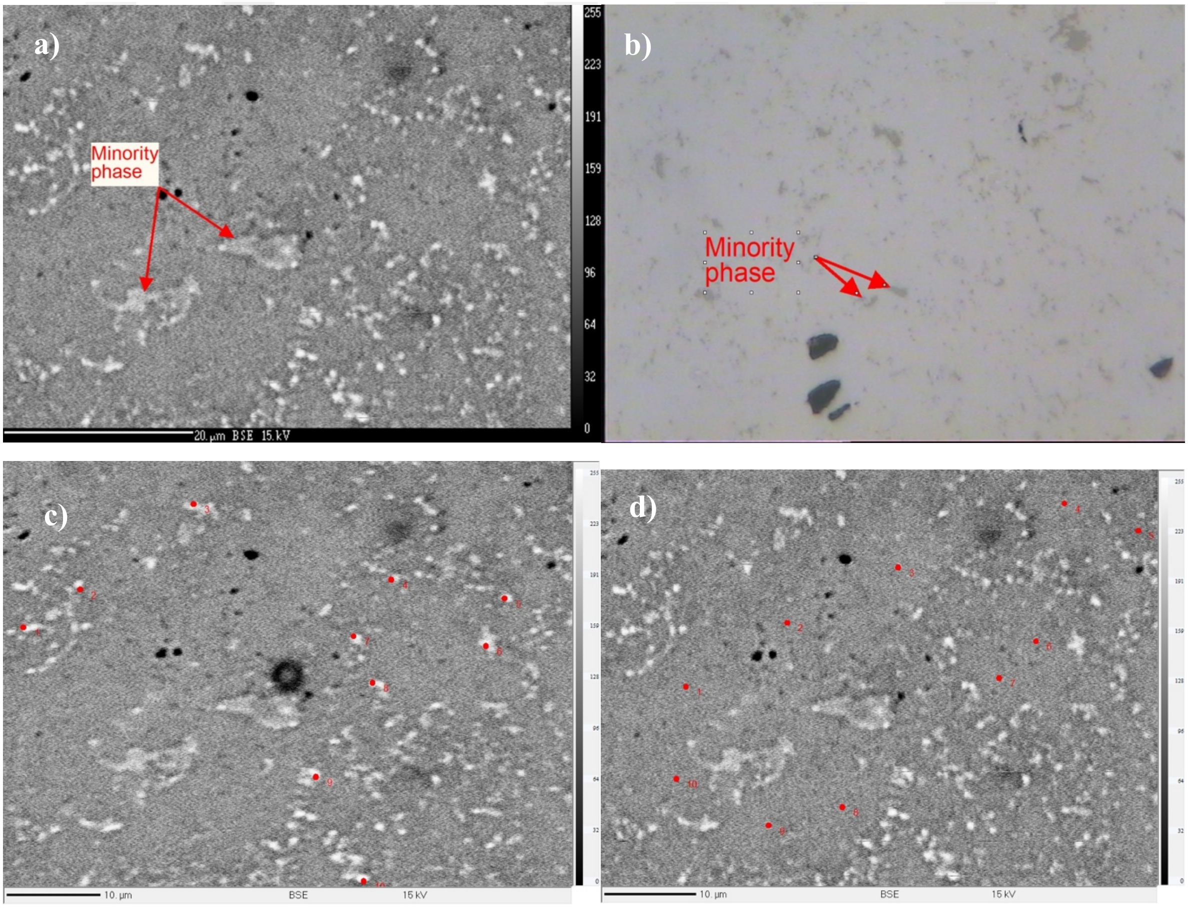

Figure 5. 17. a) BSE, **b)** Optical images of the minority phases and **c, d)** main matrix BG28 samples

By the Energy-Dispersive X-ray spectroscopy (EDX) measurements taken from the Figure 5. 17 a is given blow. Due to its higher atomic number and high electron density brighter spots were composed of Sb and Ca while darker regions were composed of Sb and Mg. Also, the Sb is precipitated in some areas while Mg and Ca dispersed uniformly resulted in a minor inhomogeneity. Also, these minority phases can explain the Sb peaks in the XRD pattern of BG28. Even though, the BG 28 sample has some minority phases, density calculations made by the Archimedes method resulted in a value of 3.87 g/cm^3 which is nearly 100% compared to the theoretical density.

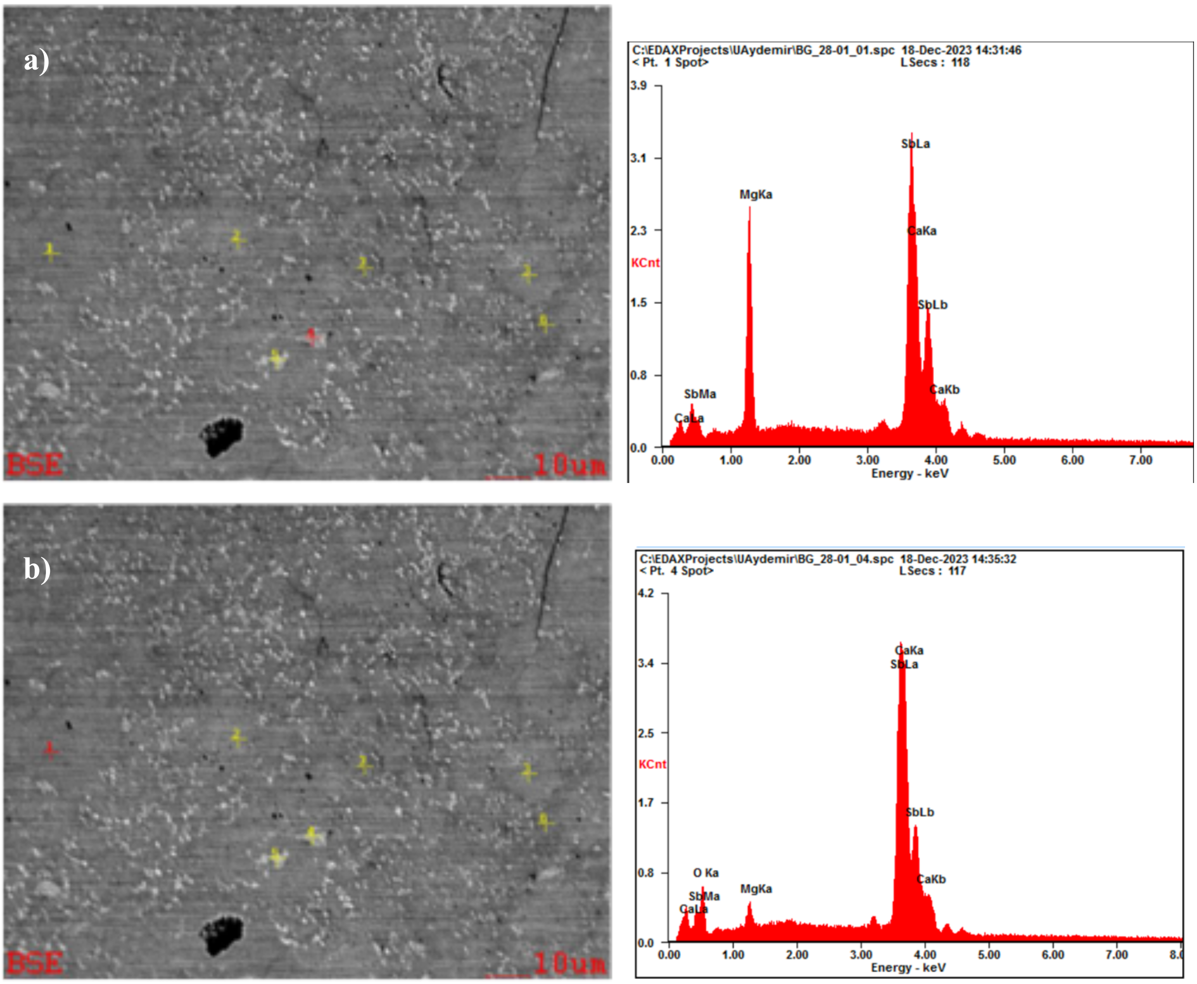

Figure 5. 18 SEM images and EDX measurements of **a)** blither and **b)** darker regions.

Table 4 displays the atomic percentages of constituent elements in undoped CaMg$_2$Sb$_2$ (BG28), differentiating between the sample's minority and actual phases.

Table 4 Calculated compositional measurements of BG28 ($CaMg_2Sb_2$) samples main, minority and bright phase regions.

	Atomic %		
	Main Phase	**Minority Phase**	**Bright Phase**
Mg	41.32	28.48	38.26
Ca	19.36	29.31	21.27
Sb	39.32	42.21	40.47
Total	100	100	100
Actual Composition	$Ca_{4.27}Mg_{4.06}Sb_2$	$Ca_{1.94}Mg_{2.88}Sb_2$	$Ca_{3.60}Mg_{3.81}Sb_2$

To change the p-type conduction properties of BG28 to n-type conduction, BG24, and BG25 samples, were prepared. Specifically, BG24 ($Ca_{0.8}La_{0.2}Mg_{2.1}Sb_2$) has underwent modification with La, while BG25 was modified with both La and Te. These adjustments aimed to influence and enhance the electrical characteristics of the samples, moving towards a desired n-type conduction behavior.

Figure 5. 19a represented the BSE image, while Figure 5.19b displayed the optical image of the BG24 sample. In the optical image, three darker regions were discernible, which remained undetected in the BSE images. During WDX analysis, the white region, marked by the red rectangle in the optical image, exhibited strong scattering. Interestingly, these darker regions, although imperceptible in the electronic image, possessed the same brightness as the primary phase of the sample.

Figures 5. 19 c and d provided magnified views of the BSE images. Notably, numerous small, brighter dots were scattered across the sample in these close-up images. This observation indicated that the WDX results for the brighter phase did not comprehensively capture the actual composition of the sample.

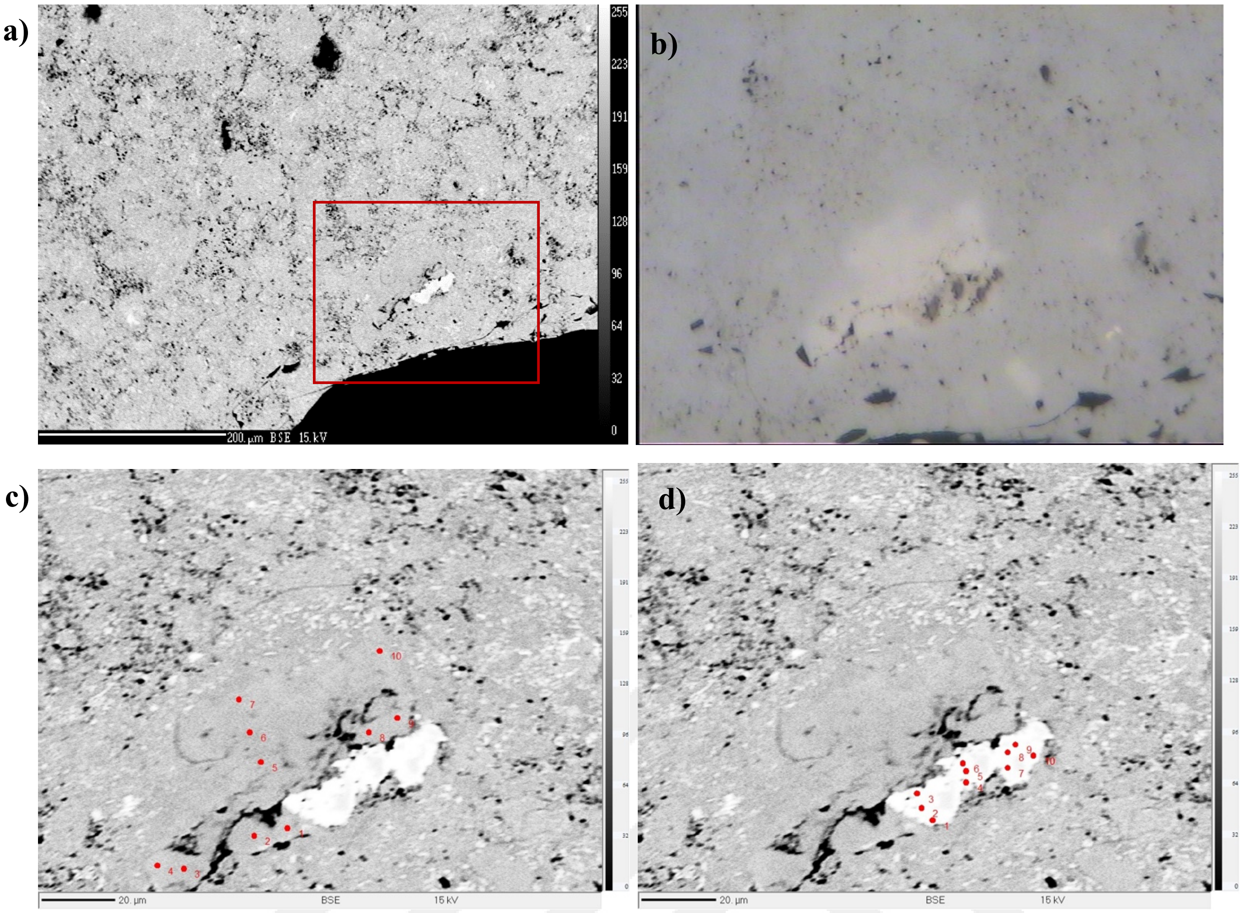

Figure 5. 19 BG24 samples **a)** BSE image, **b)** optical microscopy image, **c)** SEM image of the main phase, **d)** SEM image of the brighter region

The atomic percentages of La-doped BG24 samples, along with the calculated actual composition from WDX analysis, were presented in the Table 5 below. Additionally, SEM images in Figure 5. 20 depicted the regions of interest for EDX analysis and elemental mapping.

In Figure 5. 20 a, the darker regions were identified as a combination of Mg and Sb, while the brighter regions in Figure 5. 20 b consisted of La and Sb. This distribution was anticipated due to the higher electronic density of La compared to Mg.

After La doping, there was an observable increase in the black regions, considered as pores.

Table 5 Compositional calculations of BG24 samples bright and bright inclusion phases.

	Atomic %	
	Bright Inclusion	**Bright Phase**
Mg	19.05	49.89
Ca	2.86	44.85
Sb	48.56	48,56
Te	0.04	0.05
La	29.5	1.82
Total	100	100
Actual Composition	$Ca_{0.12}La_{1.21}Mg_{0.78}Sb_2$	$Ca_{0.15}La_{0.08}Mg_{2.2}Sb_2$

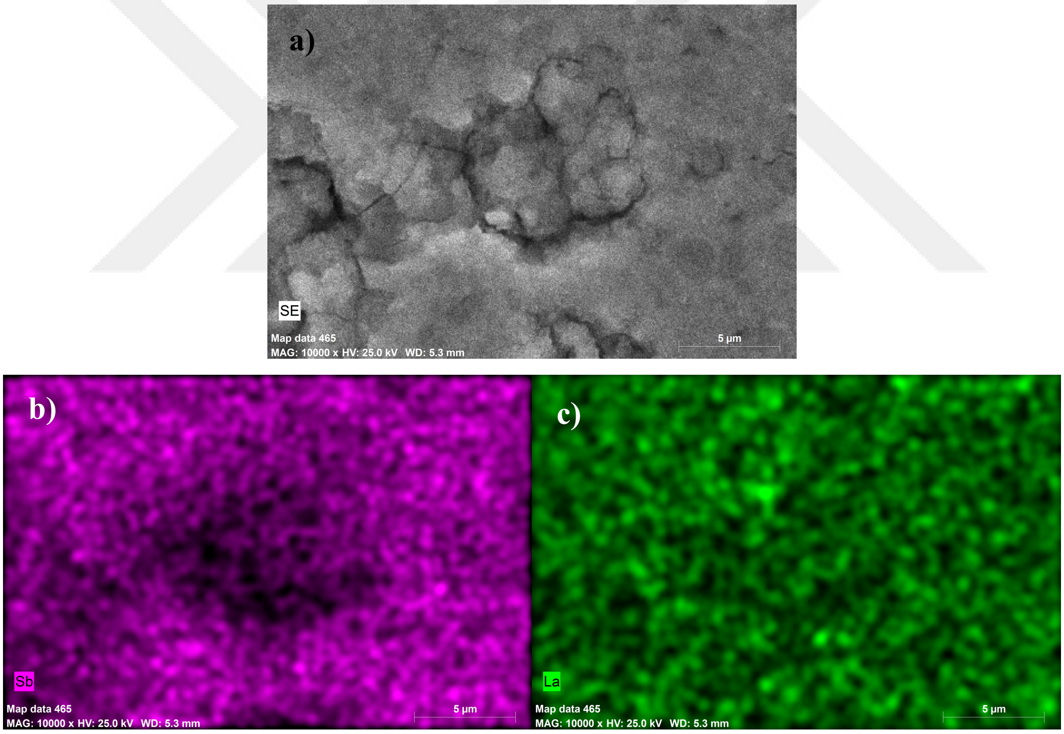

Figure 5. 20 The SEM images and EDX elemental mapping of BG24 sample.

The SEM image represented in Figure 5. 21 a was employed for EDX elemental mapping. Upon examination, La was uniformly distributed throughout the sample, while Sb was predominantly concentrated in partly brighter regions. Considering that La had a higher electronic density compared to Sb, it was inferred that the brighter regions primarily consisted of La rather than Sb. This observation may have been attributed to the potential loss of Mg in the sample, leading to an imbalance in the ratios of La and Sb.

Also, the density calculations made by the Archimedes method gave a value of 3.81 g/cm^3 for BG 24 sample, which is 98% in reference to the theoretical density. As represented from the SEM image in Figure 5.21 a and b, introducing La to the structure increased the pore volume effecting a decrease in the density of the sample.

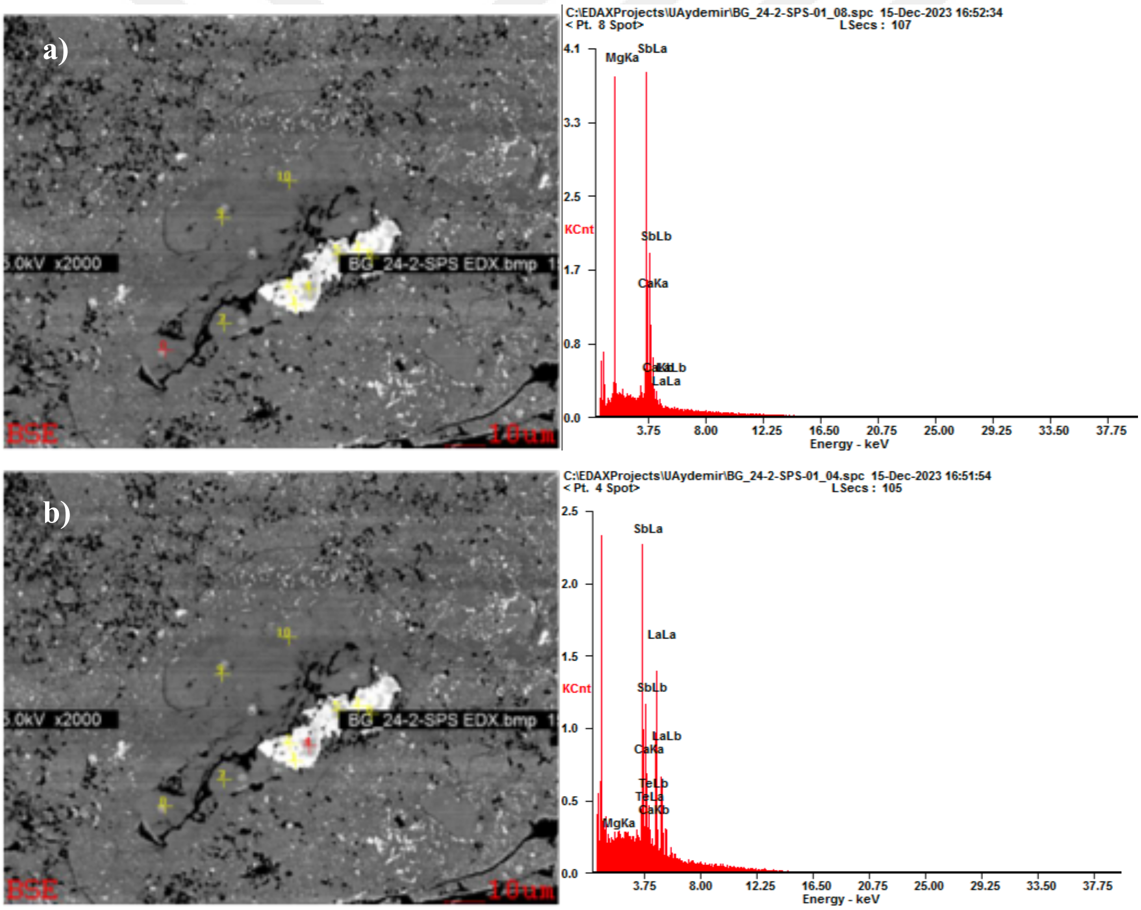

Figure 5. 21 SEM images and EDX mapping of BG 24 samples **a)** bright inclusion and **b)** bright phase.

The SEM images of the BG25 sample ($Ca_{0.9}La_{0.1}Mg_{2.1}Sb_{1.95}Te_{0.05}$) were presented in Figures 5. 22 a and b, revealing the microstructural features. Figures 5. 22 c and d provided EDX elemental mapping of the sample. The higher electronic density of La was evident in the brighter regions, while Sb was not very homogenously distributed throughout the sample. The minimal Te doping was challenging to detect via EDX measurement due to its low concentration. Therefore, WDX analysis was employed to accurately determine the Te content. Table 6 below presented the calculated composition of BG25 obtained from WDX analysis.

Furthermore, to determine the results of the synthesis, we conducted Archimedes density measurements and compare the theoretical density with the calculated results. The calculated density of BG 25 sample is 3.74 g/cm^3 which is 97 % in reference to its theoretical density. Therefore, the decrease can be attributed to the increase in the pore concentration of our sample.

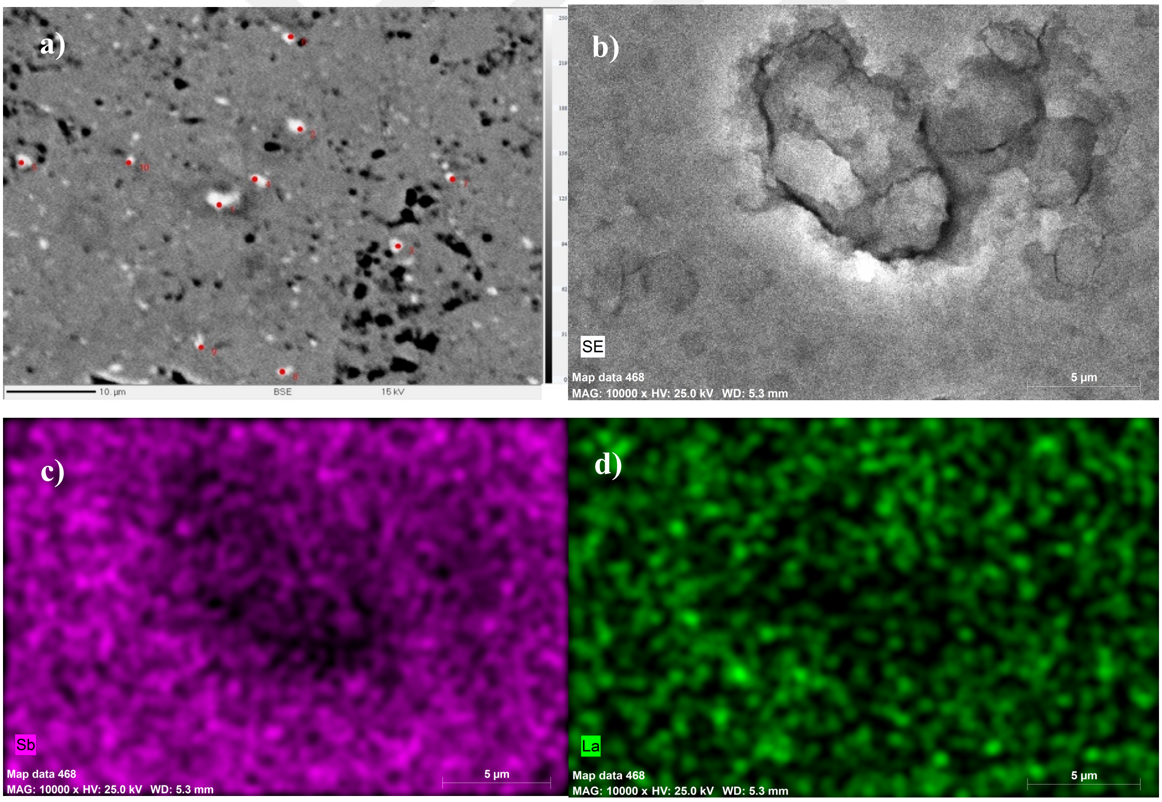

Figure 5. 22 BG25 samples **a)** bright inclusion SEM image **b)** main phase SEM image and **c, d)** EDX elemental mapping taken from the SEM image in (b).

Table 6 Compositional calculation of BG25 samples bright dots, main phase 1 and main phase 2.

	Atomic %		
	Bright Dots	**Main Phase 1**	**Main Phase 2**
Mg	40.76	41.22	41.22
Ca	15.86	17.34	17.34
Sb	38.71	38.6	38.6
Te	1.09	1.09	1.09
La	3.57	1.74	1.74
Total	99.99	100	100
Actual Composition	Ca0.8La0.18Mg2.05Sb1.95Te0.05	Ca0.08La0.09Mg2.08Sb1.95Te0.06	Ca0.08La0.09Mg2.08Sb1.95Te0.06

5.2.5.2 La and Te Doped Bi Based Samples

WDX analysis was employed to determine the composition of synthesized $CaMg_2Bi_2$-based samples. SEM images of the BG32 samples ($CaMg_2Bi_2$) were presented in Figure 5. 23a and b. Notably, two darker dots marked by red arrows in the images initially appeared as wide pores but were later identified as Fe impurities through EDX analysis.

In the EDX elemental mapping, Fe impurities were depicted in the accompanying Figure 5. 24. It was observed that these impurities may have originated during the sample preparation, possibly introduced while scraping the stainless steel to obtain the powder sample. In Figure 5. 24 a, the red dot represented a random surface section, and EDX measurements did not reveal any Fe impurities in the composition. However, in Figure 5. 24 b, the second red dot demonstrated a notable presence of Fe impurities. This indicated that these darker regions were impurity phases, while the overall sample maintained its actual composition.

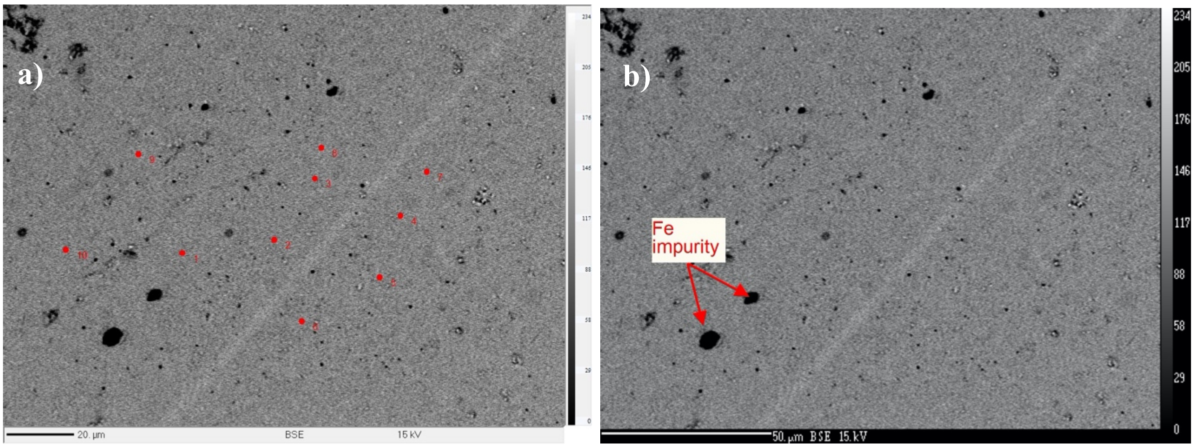

Figure 5. 23 BSE images of BG32 samples **a)** main phase, **b)** impurity phase.

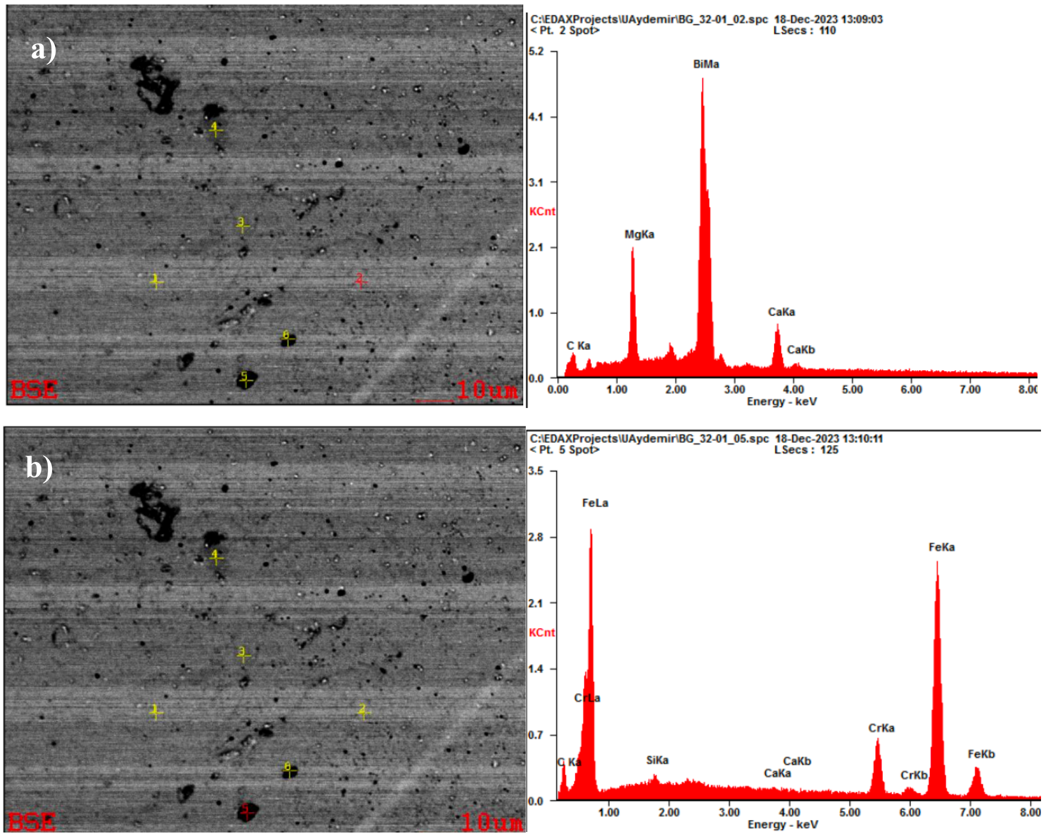

Figure 5. 24 SEM image and EDX mapping of BG32 samples **a)** main phase and **b)** impurity phase.

Following the WDX analysis, the determined composition of the synthesized sample was found to be $Ca_{0.9}Mg_{2.1}Bi_2$. Despite potential influences from sample inhomogeneity and contamination during the preparation steps, the calculation results indicated that the sample was well-achieved and closely matched the expected composition of $CaMg_2Bi_2$. Using the Archimedes density calculation method, it was determined that the density of our $CaMg_2Bi_2$ sample is 5.37 g/cm^3, which is 97% of its theoretical density value. Although the presence of Fe impurities in the sample would typically increase the overall density, the SEM image in Figure 5.23 reveals a porous structure. This porosity counteracts the effect of the Fe impurity, ultimately leading to a reduced density in the sample.

The presence of inhomogeneities in the synthesized sample, coupled with potential contamination introduced during the preparation process, may have led to variations in elemental concentrations. However, despite these challenges, the sample remained unaffected and yielded positive results.

Due to the heterogeneous nature of the BG26 and BG27 samples, we conducted a linescan analysis alongside WDX and EDX mapping. In Figure 5. 25, the BSE image of the BG26 sample subjected to linescan analysis reveals two distinct lines exhibiting varying intensities of La. In Figure 5. 25 b, the first line's intensities suggest deficiencies in Mg and Ca, with an excess of La detected at the same points. However, no definitive conclusions can be drawn regarding the Te and Bi content. Conversely, the results from the second line, depicted in Figure 5. 25 c, indicate a slight deficiency in Ca within a 63µm range, alongside an excess of Mg content at corresponding points. Notably, the levels of Te, La, and Bi remain constant throughout the analysis.

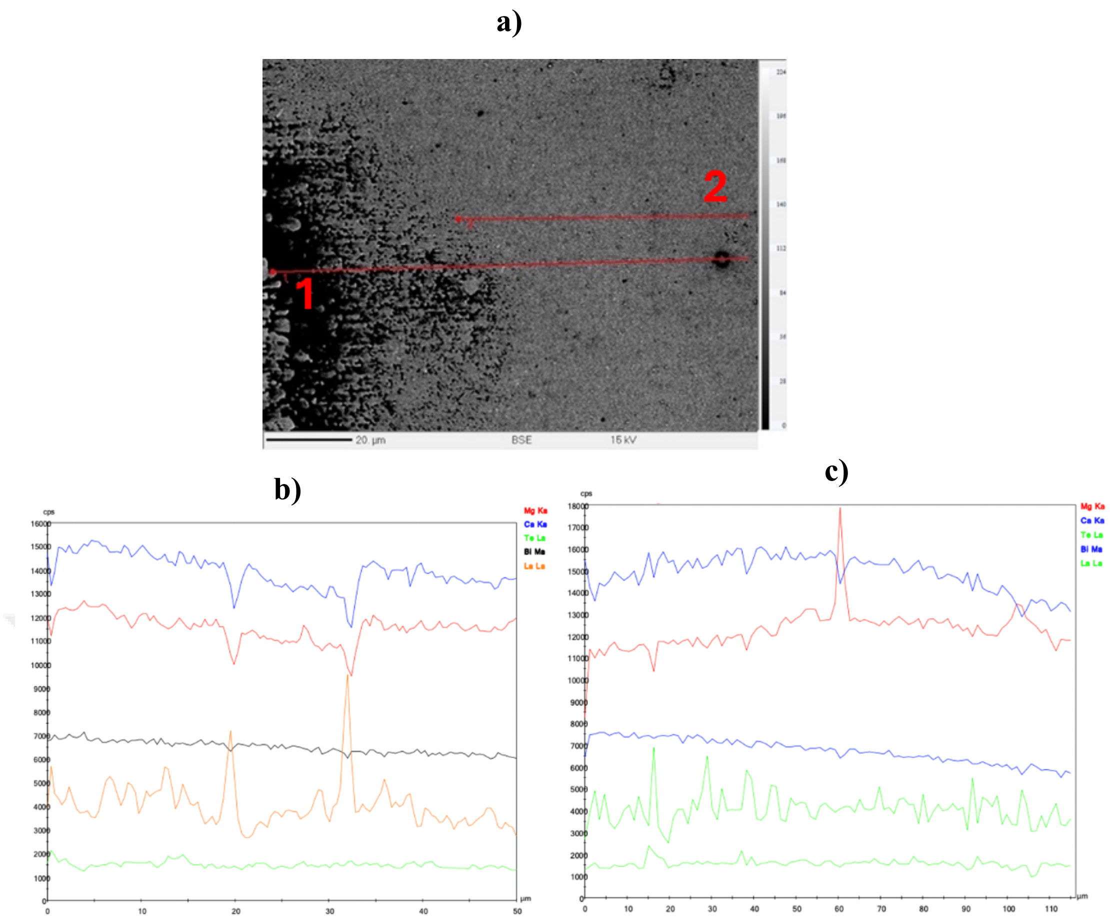

Figure 5. 25 linescan analysis on BG26 sample **a)** BSE image **b)** first line intensities **c)** second line intensities.

After, EDX mapping was performed to assess the composition in both the main phase and the darker region. The analysis utilized by the SEM image depicted in Figure 5. 26 a. It was evident from the image that Te and La are not uniformly dispersed in the material, confirming the predictions made by the linescan analysis regarding the darker regions being La-rich.

Although, the non-uniform distribution of the composition, the stoichiometric calculations from the WDX analysis indicated that the BG26 sample had a composition of $Ca_{0.97}La_{0,1}Mg_{2.47}Bi_{1.95}Te_{0,05}$. Also, the results achieved from the Archimedes density calculation method shows 98% similarity with the actual composition ($d_{Calculated}$:5.41 gr/cm^3).

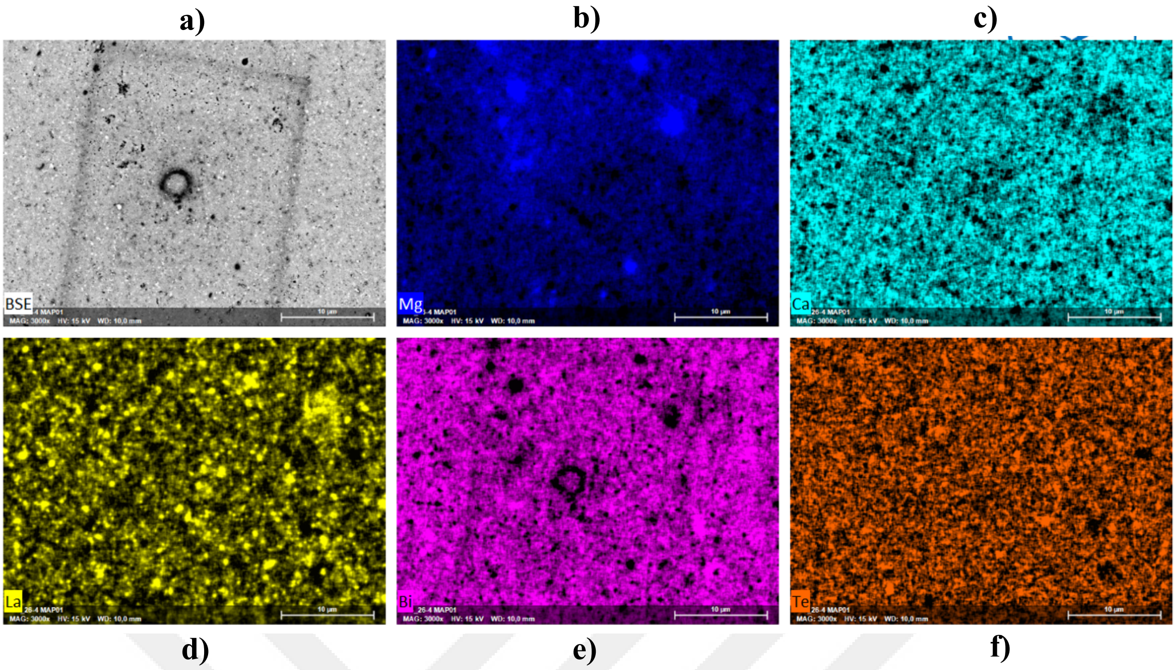

Figure 5. 26 EDX mapping of BG26 sample **a)** SEM image, **b)** Mg distribution, **c)** Ca distribution, **d)** La distribution, **e)** Bi distribution, f**)** Te distribution.

The linescan analysis and EDX mapping were done on the SEM image given below in Figure 5. 27 a for the BG27 sample. In the linescan analysis, the intensity of elemental La was determined to be very high, and the main phase composition calculated by the WDX analysis resulted as $Ca_{0.9}La_{0.14}Mg_{2.27}Bi_2$.

In Figure 5. 27, the elemental mapping of the BG27 sample is given. As seen from Figure 5. 27 e, elemental La precipitated in some regions while Ca, Mg, and Bi were homogeneously distributed. This uneven distribution resulted in minor inhomogeneity. However, the results achieved from the Archimedes density calculation method show 99.27% true results to its theoretical density.

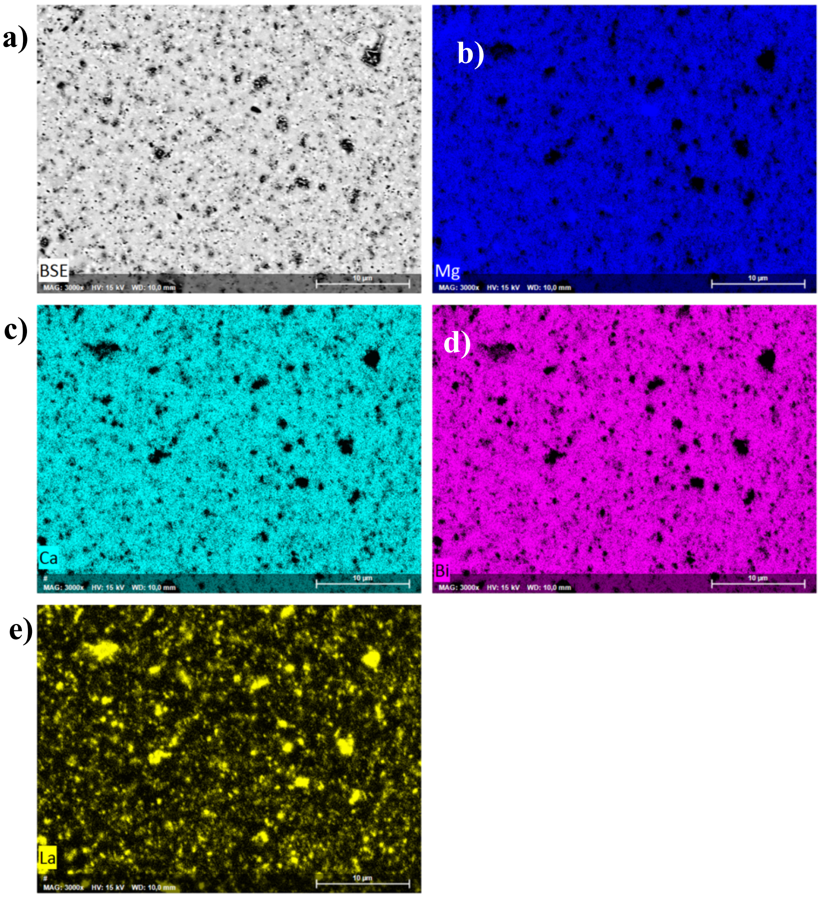

Figure 5. 27 EDX mapping of BG27 sample **a)** SEM image, **b)** Mg distribution, **c)** Ca distribution, **d)** Bi distribution, **e)** La distribution.

5.2.5.3 Mechanical Property Measurements

The Vickers hardness test was conducted on polished samples using a digital metallic Vickers hardness tester, as detailed in Chapter 4. During the test, a constant force was applied to the sample for 10 seconds, and measurements were taken until a stable reading was achieved.

Microhardness measurements were obtained from 20 to 25 different points across all Sb and Bi-based samples. The Vickers hardness indenter marks of six samples were illustrated in Figure 5. 28 and Figure 5. 29, and the corresponding average hardness values were presented in Table 7.

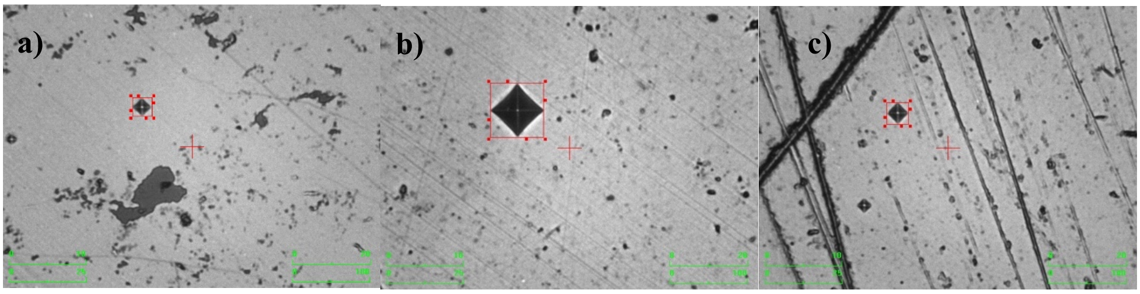

Figure 5. 28 Vickers hardness indenter marks of $CaMg_2Sb_2$ based samples **a)** BG28, **b)** BG24 and **c)** BG25.

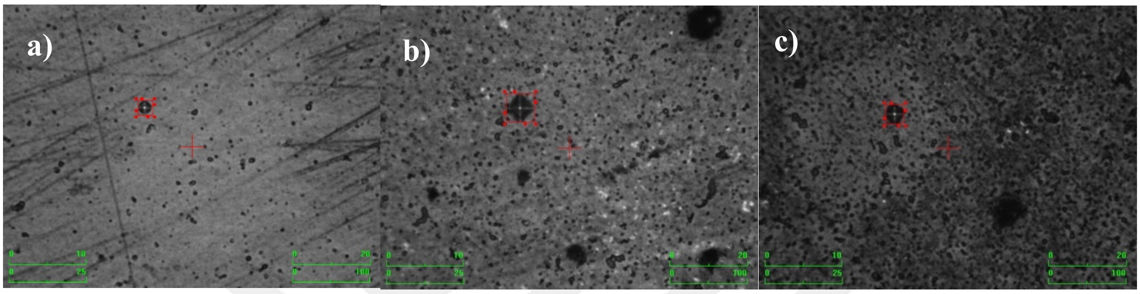

Figure 5. 29 Vickers hardness indenter marks of $CaMg_2Bi_2$ based samples **a)** BG32, **b)** BG26 and **c)** BG27.

Table 7 Average hardness values of $CaMg_2Sb_2$ based and $CaMg_2Bi_2$ based samples.

	$CaMg_2Sb_2$ Based Samples			**$CaMg_2Bi_2$ Based Samples**		
	BG28	BG24	BG25	BG32	BG26	BG27
	(Before doping)	*(Doped with La)*	*(Doped with La and Te)*	*(Before doping)*	*(Doped with La)*	*(Doped with La and Te)*
Hardness (HV)	260,3	370,6	360,3	160,32	215,3	264,3

As highlighted in the table, the $CaMg_2Sb_2$-based samples with an undoped composition demonstrated the lowest hardness values compared to the doped counterparts. Intriguingly, the introduction of Te to the structure resulted in a slight reduction in hardness of the $CaMg_2Sb_2$ sample. In contrast, the $CaMg_2Bi_2$-based samples exhibited a consistent increasing trend with each introduced doping element. When Vickers hardness of the $CaMg_2Sb_2$ and Mg_3Bi_2 is considered, the hardness values of samples BG28 and BG32 resulted in lower values (105, 106)

Chapter 6:

SUMMARY

The thesis investigates the thermoelectric properties of binary and ternary phase phosphides, with the aim of designing comprehensive phosphide thermoelectric generators. Additionally, finding new n-type Mg_3Sb_2-based materials is explored for the development of Zintl phase thermoelectric generators. First, synthesis methods of binary and ternary phosphides, namely GaP, NaSnP, and SrSnP, were screened (38). After that, the electronic and thermal conduction properties of the promising new 1-2-2 n-type Zintl compounds, $CaMg_2Sb_2$, and $CaMg_2B_{i2}$ have been studied through doping with Te and La (60, 82, 83).

The application of the solid-state synthesis method yielded fewer promising results in the synthesis of ternary phase phosphides. The NaSnP structure, synthesized with excess Sn, demonstrated air sensitivity and flammability when exposed to air. High-energy ball milling, as an alternative method, showed promising results in the phosphide synthesis process. Despite air sensitivity, the ternary phases were successfully obtained after a 4-hour synthesis process, as confirmed by XRD patterns. However, the binary compound GaP, though well-received with high-energy ball milling, exhibited exceptionally high resistivity. Computational methods were employed to explore Zn doping strategies, resulting in well-obtained Zn-doped GaP structures. Nevertheless, the resistivity remained prohibitively high for thermoelectric measurements, leading to non-promising outcomes.

In the second phase of experimental section, the focus was on exploring n-type 1-2-2-based Zintl compounds. Doping strategies employing La and Te elements were implemented on $CaMg_2Sb_2$ and $CaMg_2Bi_2$ to induce n-type conduction. Analysis of undoped powder samples revealed the presence of elemental Sb, suggesting potential loss of Ca and Mg during synthesis. Also, doping with La led to the formation of binary compounds, resulting in a decrease in doping yield below 100%. Thermoelectric measurements were performed on both undoped and doped samples, revealing the anticipated trends. The introduction of La and Te significantly lowered resistivity, indicating a marked improvement in electrical conduction. Shifting Seebeck coefficient values from positive to negative signaled a transition from proton to electron charge carriers. After doping, thermal conductivity values exhibited a decrease, with the lowest observed in samples subjected to both La and Te doping.

In conclusion, with proper doping strategies and synthesis methods to reduce air sensitivity and resistivity, thermoelectric phosphides have the potential to become high-performance materials for thermoelectric applications. Additionally, the application of La and Te doping to achieve n-type 1-2-2 structured $CaMg_2Sb_2$ and $CaMg_2Bi_2$ Zintl compounds is feasible. However, achieving proper zT values near or higher than 1 requires further optimization and related doping and microstructure engineering strategies. With continued efforts, $CaMg_2Sb_2$ and $CaMg_2Bi_2$ 1-2-2 Zintl compounds may emerge as promising candidates for designing full Zintl-type thermoelectric modules.

References

1. Firth A, Zhang B, Yang A. Quantification of global waste heat and its environmental effects. Applied energy. 2019;235:1314-34.
2. Brückner S, Liu S, Miró L, Radspieler M, Cabeza LF, Lävemann E. Industrial waste heat recovery technologies: An economic analysis of heat transformation technologies. Applied Energy. 2015;151:157-67.
3. Papapetrou M, Kosmadakis G, Cipollina A, La Commare U, Micale G. Industrial waste heat: Estimation of the technically available resource in the EU per industrial sector, temperature level and country. Applied Thermal Engineering. 2018;138:207-16.
4. Jouhara H, Khordehgah N, Almahmoud S, Delpech B, Chauhan A, Tassou SA. Waste heat recovery technologies and applications. Thermal Science and Engineering Progress. 2018;6:268-89.
5. Snyder GJ, Toberer ES. Complex thermoelectric materials. Nature materials. 2008;7(2):105-14.
6. Elsheikh MH, Shnawah DA, Sabri MFM, Said SBM, Hassan MH, Bashir MBA, et al. A review on thermoelectric renewable energy: Principle parameters that affect their performance. Renewable and sustainable energy reviews. 2014;30:337-55.
7. Tan G, Zhao L-D, Kanatzidis MG. Rationally designing high-performance bulk thermoelectric materials. Chemical reviews. 2016;116(19):12123-49.
8. Nolas GS, Sharp J, Goldsmid J. Thermoelectrics: basic principles and new materials developments: Springer Science & Business Media; 2001.
9. Rowe D. Thermoelectrics Handbook: Macro to Nano (Boca Raton: CRC/Taylor and Francis). 2006.
10. Chen L, Liu R, Shi X. Thermoelectric materials and devices: Elsevier; 2020.
11. Terasaki I. Introduction to thermoelectricity. Materials for Energy Conversion Devices. 2005:339-57.
12. Tritt TM. Thermoelectric phenomena, materials, and applications. Annual review of materials research. 2011;41:433-48.
13. Drebushchak V. The peltier effect. Journal of Thermal Analysis and Calorimetry. 2008;91:311-5.
14. May AF, Snyder GJ. Introduction to modeling thermoelectric transport at high temperatures. Materials, preparation, and characterization in thermoelectrics. 2012:1-18.

15. Snyder GJ, Ursell TS. Thermoelectric efficiency and compatibility. Physical review letters. 2003;91(14):148301.

16. Mahan G. Good Thermoelectrics, Solid State Physics, Vol. 51, Academic Press, New York 1997 (p. 81).

17. Pei Y, Wang H, Snyder GJ. Band engineering of thermoelectric materials. Advanced materials. 2012;24(46):6125-35.

18. Zhang X, Bu Z, Shi X, Chen Z, Lin S, Shan B, et al. Electronic quality factor for thermoelectrics. Science advances. 2020;6(46):eabc0726.

19. Kauzlarich SM, Brown SR, Snyder GJ. Zintl phases for thermoelectric devices. Dalton Transactions. 2007(21):2099-107.

20. Yu K, Zhou Y, Liu Y, Liu F, Hu L, Ao W, et al. Near-room-temperature thermoelectric materials and their application prospects in geothermal power generation. Geomechanics and Geophysics for Geo-Energy and Geo-Resources. 2020;6:1-25.

21. Schwartz M. Encyclopedia of materials, parts and finishes: CRC press; 2002.

22. Neeli G, Behara DK, Kumar MK. State of the art review on thermoelectric materials. International Journal of Science and Research. 2016;5:1833-44.

23. Jonson M, Mahan G. Mott's formula for the thermopower and the Wiedemann-Franz law. Physical Review B. 1980;21(10):4223.

24. Chen Z-G, Han G, Yang L, Cheng L, Zou J. Nanostructured thermoelectric materials: Current research and future challenge. Progress in Natural Science: Materials International. 2012;22(6):535-49.

25. Taherian R, Kausar A. Electrical Conductivity in Polymer-Based Composites: Experiments, Modelling, and Applications: William Andrew; 2018.

26. Kuo JJ, Kang SD, Imasato K, Tamaki H, Ohno S, Kanno T, et al. Grain boundary dominated charge transport in Mg 3 Sb 2-based compounds. Energy & Environmental Science. 2018;11(2):429-34.

27. Grimvall G. Thermophysical properties of materials: Elsevier; 1999.

28. Mohamed Bashir Ali Bashir SMS, Mohd Faizul Mohd Sabri, Dhafer Abdulameer Shnawah, Mohamed Hamid Elsheikh. Recent advances on Mg2Si1−xSnx materials for thermoelectric generation. Renewable and Sustainable Energy Reviews. 2014;37:569-84.

29. Zhang Y. First-principles Debye–Callaway approach to lattice thermal conductivity. Journal of Materiomics. 2016;2(3):237-47.

30. Wan C, Wang Y, Wang N, Norimatsu W, Kusunoki M, Koumoto K. Development of novel thermoelectric materials by reduction of lattice thermal conductivity. Science and Technology of Advanced Materials. 2010.

31. Zaferani SH, Ghomashchi R, Vashaee D. Strategies for engineering phonon transport in Heusler thermoelectric compounds. Renewable and Sustainable Energy Reviews. 2019;112:158-69.

32. Chen J-H, Whitmire KH. A structural survey of the binary transition metal phosphides and arsenides of the d-block elements. Coordination Chemistry Reviews. 2018;355:271-327.

33. Corbridge DE. Phosphorus: chemistry, biochemistry and technology: CRC press; 2013.

34. Schlesinger ME. The thermodynamic properties of phosphorus and solid binary phosphides. Chemical reviews. 2002;102(11):4267-302.

35. Quinn R, Bos J-W. Recent progress in phosphide materials for thermoelectric energy conversion. Journal of Materials Chemistry A. 2023.

36. Pöhls J-H, Faghaninia A, Petretto G, Aydemir U, Ricci F, Li G, et al. Metal phosphides as potential thermoelectric materials. Journal of Materials Chemistry C. 2017;5(47):12441-56.

37. Zhang J, Liu H, Cheng L, Wei J, Liang J, Fan D, et al. High thermoelectric performance can be achieved in black phosphorus. Journal of Materials Chemistry C. 2016;4(5):991-8.

38. Nuss Jr, Wedig U, Xie W, Yordanov P, Bruin J, Hübner R, et al. Phosphide–tetrahedrite Ag6Ge10P12: thermoelectric performance of a long-forgotten silver-cluster compound. Chemistry of Materials. 2017;29(16):6956-65.

39. Yi T, Zhang G, Tsujii N, Fleurial J-P, Zevalkink A, Snyder GJ, et al. Phase characterization, thermal stability, high-temperature transport properties, and electronic structure of rare-earth Zintl phosphides Eu3M2P4 (M= Ga, In). Inorganic chemistry. 2013;52(7):3787-94.

40. Reshak A, Auluck S. Thermoelectric properties of Nowotny–Juza NaZnX (X= P, As and Sb) compounds. Computational Materials Science. 2015;96:90-5.

41. Yuan X, Zhao Y, Ni J, Meng S, Dai Z. Thermoelectric transport properties of metal phosphide XLiP (X= Sr, Ba). Journal of Physics: Condensed Matter. 2023;35(15):155501.

42. Lin L, Woods G, Callcott T. Soft-X-ray fluorescence spectra of III− V phosphides BP, GaP, and InP. Physical Review B. 2001;63(23):235107.

43. Miao J, Chai C, Zhang W, Song Y, Yang Y. First-Principles Study on Structural, Mechanical, Anisotropic, Electronic and Thermal Properties of III-Phosphides: XP (X= Al, Ga, or In) in the P 6422 Phase. Materials. 2020;13(3):686.

44. Haq BU, AlFaify S, Ahmed R, Al-Qaisi S, Alsardia M, Khadka I, et al. Thermoelectric properties of different polymorphs of gallium phosphide; A first-principles study. Ceramics International. 2022;48(1):642-7.

45. Arbouche O, Belgoumène B, Soudini B, Azzaz Y, Bendaoud H, Amara K. First-principles study on structural properties and phase stability of III-phosphide (BP, GaP, AlP and InP). Computational materials science. 2010;47(3):685-92.

46. Gajaria TK, Dabhi SD, Jha PK. Ab initio energetics and thermoelectric profiles of gallium pnictide polytypes. Scientific Reports. 2019;9(1):5884.

47. Janka O, Kauzlarich SM. Zintl compounds. Encyclopedia of Inorganic and Bioinorganic Chemistry. 2011:1-19.

48. Sevov SC. Zintl phases. Intermetallic Compounds-Principles and Practice: Progress. 2002;3:113-32.

49. Steurer W. Crystal structures of metallic elements and compounds. Physical Metallurgy: Elsevier; 2014. p. 1-101.

50. Funahashi R. Thermoelectric energy conversion: theories and mechanisms, materials, devices, and applications: Woodhead Publishing; 2021.

51. Miller G. Structure and bonding at the Zintl border. Chemistry, structure and bonding of Zintl phases and ions. 1996:1.

52. Muller U. Inorganic structural chemistry: John Wiley & Sons; 2007.

53. Shuai J, Mao J, Song S, Zhang Q, Chen G, Ren Z. Recent progress and future challenges on thermoelectric Zintl materials. Materials Today Physics. 2017;1:74-95.

54. Liu K-F, Xia S-Q. Recent progresses on thermoelectric Zintl phases: Structures, materials and optimization. Journal of Solid State Chemistry. 2019;270:252-64.

55. Toberer ES, Cox CA, Brown SR, Ikeda T, May AF, Kauzlarich SM, et al. Traversing the metal-insulator transition in a Zintl phase: rational enhancement of thermoelectric efficiency in Yb14Mn1− xAlxSb11. Advanced Functional Materials. 2008;18(18):2795-800.

56. Ortiz BR, Gorai P, Krishna L, Mow R, Lopez A, McKinney R, et al. Potential for high thermoelectric performance in n-type Zintl compounds: a case study of Ba doped KAlSb 4. Journal of Materials Chemistry A. 2017;5(8):4036-46.

57. Madsen GK. Automated search for new thermoelectric materials: the case of LiZnSb. Journal of the American Chemical Society. 2006;128(37):12140-6.

58. Toberer ES, May AF, Scanlon CJ, Snyder GJ. Thermoelectric properties of p-type LiZnSb: Assessment of ab initio calculations. Journal of Applied Physics. 2009;105(6).

59. Zhang J, Song L, Pedersen SH, Yin H, Hung LT, Iversen BB. Discovery of high-performance low-cost n-type Mg3Sb2-based thermoelectric materials with multi-valley conduction bands. Nature communications. 2017;8(1):13901.

60. Ohno S, Imasato K, Anand S, Tamaki H, Kang SD, Gorai P, et al. Phase boundary mapping to obtain n-type Mg3Sb2-based thermoelectrics. Joule. 2018;2(1):141-54.

61. Shi X, Wang X, Li W, Pei Y. Advances in thermoelectric Mg3Sb2 and its derivatives. Small Methods. 2018;2(10):1800022.

62. Condron CL, Kauzlarich SM, Gascoin F, Snyder GJ. Thermoelectric properties and microstructure of Mg3Sb2. Journal of Solid State Chemistry. 2006;179(8):2252-7.

63. Brod MK, Anand S, Snyder GJ. The Importance of Mg–Sb Interactions in Achieving High Conduction Band Degeneracy in Mg3Sb2 for High n-Type Thermoelectric Performance. Materials Today Physics. 2023;31:100959.

64. Ozen M, Yahyaoglu M, Candolfi C, Veremchuk I, Kaiser F, Burkhardt U, et al. Enhanced thermoelectric performance in Mg 3+ x Sb 1.5 Bi 0.49 Te 0.01 via engineering microstructure through melt-centrifugation. Journal of Materials Chemistry A. 2021;9(3):1733-42.

65. Tang X, Zhang B, Zhang X, Wang S, Lu X, Han G, et al. Enhancing the thermoelectric performance of p-type Mg3Sb2 via codoping of Li and Cd. ACS applied materials & interfaces. 2020;12(7):8359-65.

66. Xu B, Li R, Yu G, Ma S, Wang Y, Wang Y, et al. The relation between the electronic structure and thermoelectric properties for Zintl compounds Mg3Sb2. Journal of the Physical Society of Japan. 2017;86(2):024601.

67. Zhang J, Song L, Mamakhel A, Jørgensen MRV, Iversen BB. High-performance low-cost n-type Se-doped Mg3Sb2-based Zintl compounds for thermoelectric application. Chemistry of Materials. 2017;29(12):5371-83.

68. Bhardwaj A, Rajput A, Shukla A, Pulikkotil J, Srivastava A, Dhar A, et al. Mg 3 Sb 2-based Zintl compound: a non-toxic, inexpensive and abundant thermoelectric material for power generation. RSC advances. 2013;3(22):8504-16.

69. Zhang J, Song L, Madsen GK, Fischer KF, Zhang W, Shi X, et al. Designing high-performance layered thermoelectric materials through orbital engineering. Nature communications. 2016;7(1):10892.

70. Imasato K, Wood M, Anand S, Kuo JJ, Snyder GJ. Understanding the high thermoelectric performance of Mg3Sb2-Mg3Bi2 alloys. Advanced Energy and Sustainability Research. 2022;3(6):2100208.

71. Imasato K, Kang SD, Ohno S, Snyder GJ. Band engineering in Mg 3 Sb 2 by alloying with Mg 3 Bi 2 for enhanced thermoelectric performance. Materials Horizons. 2018;5(1):59-64.

72. Bhardwaj A, Chauhan N, Misra D. Significantly enhanced thermoelectric figure of merit of p-type Mg 3 Sb 2-based Zintl phase compounds via nanostructuring and employing high energy mechanical milling coupled with spark plasma sintering. Journal of Materials Chemistry A. 2015;3(20):10777-86.

73. Chen X, Wu H, Cui J, Xiao Y, Zhang Y, He J, et al. Extraordinary thermoelectric performance in n-type manganese doped Mg3Sb2 Zintl: high band degeneracy, tuned carrier scattering mechanism and hierarchical microstructure. Nano Energy. 2018;52:246-55.

74. Mao J, Shuai J, Song S, Wu Y, Dally R, Zhou J, et al. Manipulation of ionized impurity scattering for achieving high thermoelectric performance in n-type Mg3Sb2-based materials. Proceedings of the National Academy of Sciences. 2017;114(40):10548-53.

75. Gorai P, Toberer ES, Stevanović V. Effective n-type doping of Mg3Sb2 with group-3 elements. Journal of Applied Physics. 2019;125(2).

76. Shuai J, Wang Y, Kim HS, Liu Z, Sun J, Chen S, et al. Thermoelectric properties of Na-doped Zintl compound: Mg3− xNaxSb2. Acta Materialia. 2015;93:187-93.

77. Bhardwaj A, Misra D. Enhancing thermoelectric properties of a p-type Mg3Sb2-based Zintl phase compound by Pb substitution in the anionic framework. RSC Adv. 4, 34552–34560 (2014).

78. Chen C, Li X, Li S, Wang X, Zhang Z, Sui J, et al. Enhanced thermoelectric performance of p-type Mg3Sb2 by lithium doping and its tunability in an anionic framework. Journal of Materials Science. 2018;53(23):16001-9.

79. Zhang J, Song L, Iversen BB. Insights into the design of thermoelectric Mg3Sb2 and its analogs by combining theory and experiment. Npj Computational Materials. 2019;5(1):76.

80. Zhang Y-b, Liang J-S, Liu C, Zhou Q, Xu Z, Chen H-b, et al. Enhancing thermoelectric performance in P-Type Mg3Sb2-based zintls through optimization of band gap structure and nanostructuring. Journal of Materials Science & Technology. 2024;170:25-32.

81. Imasato K, Kang SD, Snyder GJ. Exceptional thermoelectric performance in Mg 3 Sb 0.6 Bi 1.4 for low-grade waste heat recovery. Energy & Environmental Science. 2019;12(3):965-71.

82. Gorai P, Stevanović V, Toberer ES. Computationally guided discovery of thermoelectric materials. Nature Reviews Materials. 2017;2(9):1-16.

83. Sun J, Singh DJ. Thermoelectric properties of AMg 2 X 2, AZn 2 Sb 2 (A= Ca, Sr, Ba; X= Sb, Bi), and Ba 2 ZnX 2 (X= Sb, Bi) Zintl compounds. Journal of Materials Chemistry A. 2017;5(18):8499-509.

84. Tokita M. Chapter 11.2. 3-Spark Plasma Sintering (SPS) Method, Systems, and Applications. Handbook of Advanced Ceramics. 2013:1149-77.

85. Anselmi-Tamburini U. Spark plasma sintering. 2021.

86. Suárez M, Fernández A, Menéndez J, Torrecillas R, Kessel H, Hennicke J, et al. Challenges and opportunities for spark plasma sintering: a key technology for a new generation of materials. Sintering applications. 2013;13:319-42.

87. Epp J. X-ray diffraction (XRD) techniques for materials characterization. Materials characterization using nondestructive evaluation (NDE) methods: Elsevier; 2016. p. 81-124.

88. Lamas DG, de Oliveira Neto M, Kellermann G, Craievich AF. X-ray Diffraction and Scattering by Nanomaterials. Nanocharacterization techniques: Elsevier; 2017. p. 111-82.

89. Salame PH, Pawade VB, Bhanvase BA. Characterization tools and techniques for nanomaterials. Nanomaterials for green energy: Elsevier; 2018. p. 83-111.

90. Inagaki M, Kang F. Materials science and engineering of carbon: characterization: Butterworth-Heinemann; 2016.

91. Vernon-Parry KD. Scanning electron microscopy: an introduction. III-Vs review. 2000;13(4):40-4.

92. de Oliveira Jr O, Ferreira L, Marystela G, de Lima Leite F, Da Róz AL. Nanocharacterization Techniques: William Andrew; 2017.

93. Kim B, Hochella Jr MF. Analytical transmission electron microscopy and scanning transmission electron microscopy techniques for the characterization of nanomaterial composition, phase and crystallinity. Frontiers of Nanoscience. 8: Elsevier; 2015. p. 123-52.

94. Tang C, Yang Z. Transmission electron microscopy (TEM). Membrane characterization: Elsevier; 2017. p. 145-59.

95. Zhu Q, Kim HS, Ren Z. A rapid method to extract Seebeck coefficient under a large temperature difference. Review of Scientific Instruments. 2017;88(9).

96. Miyauchi T, Sonomura H, Yamamoto N. Electrical Properties of Gallium Phosphide. Japanese Journal of Applied Physics. 1967;6(12):1409.

97. Shannon RD. Revised effective ionic radii and systematic studies of interatomic distances in halides and chalcogenides. Acta crystallographica section A: crystal physics, diffraction, theoretical and general crystallography. 1976;32(5):751-67.

98. Jain A, Ong SP, Hautier G, Chen W, Richards WD, Dacek S, et al. Commentary: The Materials Project: A materials genome approach to accelerating materials innovation. APL materials. 2013;1(1).

99. Wang Y, Zhang X, Wang Y, Liu H, Zhang J. Enhanced Thermoelectric Properties of n-type Mg3Sb2 by Excess Magnesium and Tellurium Doping. physica status solidi (a). 2019;216(6):1800811.

100. Tani J-i, Ishikawa H. Thermoelectric properties of Te-doped Mg3Sb2 synthesized by spark plasma sintering. Physica B: Condensed Matter. 2020;588:412173.

101. Sun C, Shi X, Zheng L, Chen B, Li W. Transport properties of p-type CaMg2Bi2 thermoelectrics. Journal of Materiomics. 2019;5(4):567-73.

102. Peng X, Guo J, Su X, Wu J, Zhang Q, Tang X. Ultrafast Combustion Synthesis and High Thermoelectric Performance of Mg3Sb2-x Bi x-Based Compounds. ACS Applied Energy Materials. 2024;7(6):2552-60.

103. Song L, Zhang J, Iversen BB. Simultaneous improvement of power factor and thermal conductivity via Ag doping in p-type Mg 3 Sb 2 thermoelectric materials. Journal of Materials Chemistry A. 2017;5(10):4932-9.

104. May AF, McGuire MA, Singh DJ, Custelcean R, Jellison Jr GE. Structure and properties of single crystalline CaMg2Bi2, EuMg2Bi2, and YbMg2Bi2. Inorganic chemistry. 2011;50(21):11127-33.

105. Li G, Aydemir U, Wood M, An Q, Goddard III WA, Zhai P, et al. Deformation mechanisms in high-efficiency thermoelectric layered Zintl compounds. Journal of Materials Chemistry A. 2017;5(19):9050-9.

106. Chen Y, Zuo E, Dou X, Chen L, Jiang G, Mao A. First-principles investigation of mechanical properties, elastic anisotropy, and ultralow lattice thermal conductivities of ductile Mg–Bi alloys. Vacuum. 2022;206:111535.